

The Steklov spectrum of the Helmholtz operator

by

Kshitij Anand Patil

M.Sc. (Engineering Mathematics), Institute of Chemical Technology, Mumbai, 2019

B.Tech (Telecommunications), Mumbai University, 2018

B.Sc. (Mathematics), Mumbai University, 2017

Thesis Submitted in Partial Fulfillment of the
Requirements for the Degree of
Master of Science

in the
Department of Mathematics
Faculty of Science

© Kshitij Anand Patil 2023
SIMON FRASER UNIVERSITY
Fall 2023

Copyright in this work is held by the author. Please ensure that any reproduction or re-use
is done in accordance with the relevant national copyright legislation.

Declaration of Committee

Name: **Kshitij Anand Patil**

Degree: **Master of Science**

Thesis title: **The Steklov spectrum of the Helmholtz operator**

Committee:

Chair:	Tamon Stephen Professor, Mathematics
Nilima Nigam Co-Supervisor Professor, Mathematics	
Weiran Sun Co-Supervisor Associate Professor, Mathematics	
Ben Adcock Committee Member Professor, Mathematics	
Steve Ruuth Committee Member Professor, Mathematics	
John Stockie Examiner Professor, Mathematics	

Abstract

The Steklov eigenvalue problem is a boundary value problem where the spectral parameter relates the Dirichlet and Neumann traces. It has been extensively studied for the Laplacian [GP17]. In this thesis, we study the Steklov problem for the Helmholtz operator $-\Delta - \mu^2$ with real wave number μ for bounded planar domains. After reformulating this problem as a boundary integral equation we implement a numerical method with the help of layer potentials approximated using quadratures as in [CK13]. We obtain a generalized eigenvalue problem for the Steklov-Helmholtz eigenvalues and eigendensities, where the eigenfunctions are reconstructed using the single layer potential. We describe a numerical approach for the reformulated problem. We observe exponential convergence of the numerically computed Steklov-Helmholtz eigenvalues. A Weyl-type law is observed for the asymptotics of the spectrum. We report on additional experiments including a shape optimization problem. The numerical scheme is tested on a variety of domains of genus 0 and 1. Our approach can be adapted to other problems as well.

Keywords: Helmholtz equation; eigenvalue problems; Dirichlet to Neumann maps; boundary integral equations; quadrature rules

Dedication

To my parents (Mrs. Vaishali Patil and Dr. Anand Patil) and myself.

Acknowledgements

We are probably some type of average of the people that surround us. If that is true, then I am at the very least awesome. I have had the good fortune of being in the company of the kindest people and my parents have always given me the freedom to do what I like.

I would not have had the opportunity to come study at SFU if it was not for Prof. Nilima Nigam and the financial support that she, Prof. Steve Ruuth and the department of Mathematics at SFU provided to me which made it possible for me to pursue my love for maths. Every meeting and discussion I have had with Dr. Nilima, no matter how short has made me a better Mathematician and thinker. Her kindness (never mind how much she denies being nice) and patience are contagious in the best way possible. I often use the terms guide, advisor and supervisor interchangeably and all of them hold true for Dr. Nilima. She guides me along the way, advises me on possible turns I could make and supervises over my mistakes and shortcomings. For example, this thesis solely exists because at one meeting she told me about the Steklov boundary condition, which I had never seen before. Prof. Ben Adcock and Prof. Weiran Sun have also been a great supporters of mine and have gladly accepted all my requests (*so far ;)*). The courses that I took in the first year of my masters program have tremendously improved my mathematical ability and I would like to thank all my instructors, Dr. Ben, Dr. Nilima, Dr. Steve, Prof. David Muraki, Prof. Razvan Fetecau and Dr. Weiran. It would be incomplete to not mention how great the department staff have been and I would specially like to thank Stacey Openshaw, Christie Carlson, Rachel Tong, Dale Yamaura, Casey Bell and Rita Li for being ever so helpful and lively. I would also like to thank the students that I interacted with while TAing for helping me become a better teacher and more patient. My friends are great stress relievers and reminders that it is okay to smell the roses. For improvements to this thesis I thank Juan, Javier, Matt, Kthim, Daniel (especially for RBFs), Ryan, Sebastian, Sharon, Piyush, Vatsal, Kanwal, Kulwant, Aman, Madhur, Govind and Aishu. Should any of my other friends read this, you know who you are and don't let my ignorance undercut your importance.

The unconditional love from my grandmums (Mrs. Pushpa Ruparel and Mrs. Savitribai Patil), my parents, my dog Floyd and the rest of my family has given me the strength and courage to be away from home for long periods of time. Special shoutout to my uncle Mr. Prasad Ruparel for being who he is. I was also lucky enough to be friends with dogs here, Alpha and Sally who make me so happy by just being there. Finally I would like to thank my teachers, Mr. Nilesh Shah, Dr. Amiya Bhowmick, Dr. Akshay Rane, Dr. Nitin Gulhane, Mr. Algonda Desai, Dr. Ramrup Sarkar and Mr. Subhash Krishnan who have been teaching me how to be a good Mathematician since way back when.

There is a sequence of words which will make it all ok, please assume that I wrote it here. To the very best of times, gone and to come.

Contents

Declaration of Committee	ii
Abstract	iii
Dedication	iv
Acknowledgements	v
Table of Contents	vi
List of Algorithms	viii
List of Tables	viii
List of Figures	x
1 Introduction	1
1.1 Notation and thesis structure	1
1.2 Thesis contributions	4
1.3 History of the Steklov-Laplace problem	4
1.4 History of the Steklov-Helmholtz problem	7
1.4.1 The one dimensional Steklov-Helmholtz eigenvalue problem	8
1.4.2 Comparing Steklov-Laplace and Steklov-Helmholtz eigenfunctions of the unit disk	9
1.5 The Helmholtz equation in \mathbb{R}^2	11
1.6 Integral operators and potentials	13
1.7 Dirichlet to Neumann maps	19
1.7.1 Maps	21
1.7.2 Assumptions for unique solutions	21
1.7.3 Connection to the Steklov-Helmholtz problem	22
1.7.4 Connection to the Transmission problem	23

2 Reformulating and discretizing the Steklov-Helmholtz eigenvalue problem	25
2.1 2d Integral reformulation	25
2.1.1 Boundary parametrization	26
2.2 Splitting to treat singularities	27
2.3 Specialized quadratures	31
2.4 Generalized eigenvalue problem	33
3 Numerical experiments for the Steklov-Helmholtz problem for smooth and bounded domains in \mathbb{R}^2	36
3.1 Tests on a disk of radius $R > 0$	36
3.1.1 Interior Dirichlet and Neumann problems	37
3.1.2 Dirichlet / Neumann / Robin eigenvalues of the Laplacian	39
3.1.3 Steklov-Helmholtz problem on the disk	44
3.2 Approaching Dirichlet-Laplace eigenvalues	56
3.3 The Steklov-Helmholtz problem on domains of genus 1	59
3.4 Convergence tests on genus 0 and genus 1 domains	65
3.4.1 Experiments on genus 0 domains	65
3.4.2 Experiments on genus 1 domains	66
3.5 Negative eigenvalues and spectral asymptotics for domains of genus 0	68
3.5.1 Number of negative Steklov-Helmholtz eigenvalues	69
3.5.2 Standard homothety of Steklov-Helmholtz eigenvalue problem and connection to the Robin-Laplacian	72
3.5.3 Asymptotic behaviour of Steklov-Helmholtz eigenvalues	76
3.6 Boundary weights	82
3.7 Shape optimization of Steklov-Helmholtz eigenvalues	86
4 Transmission eigenvalue problem	94
4.1 Searching for transmission eigenvalues	95
4.2 Tests	95
5 Conclusion and discussion	99
5.1 Summary	99
5.2 Future work	100
References	102
Appendix A Curve library	106
Appendix B README for the code	107
B.1 Curves	107

B.2	Trigonometric polynomials	109
B.3	Layer potentials	109
B.4	Steklov eigenvalues	111
B.5	Construction of solutions inside Ω	112
B.6	RBFs	113

List of Algorithms

1	Search for Laplace eigenvalues λ^D, λ^N and λ^R	39
2	RBF interpolation of function evaluations for f , see Appendix B.6	41
3	Approximating the tangential gradient $\nabla_\Gamma u$ using RBFs, see Appendix B.6	88
4	Search for transmission eigenvalues μ_T	95

List of Tables

Table 1.1	Standard Laplace eigenvalue problems.	2
Table 1.2	Comparison of Steklov-Laplace and Steklov-Helmholtz eigenpairs for the unit disk.	9
Table 3.1	First 5 entries of the true and approximate densities, $\mu = 7$, $N = 729$, $R = 2\pi$. The columns correspond to the Interior Dirichlet Problem (IDP). The numbers in pink bold text are the digits for which the true densities ψ^{comp} computed using inbuilt MATLAB functions are constant. The numbers in blue bold text are the digits for which the densities ψ^N computed by our approach are constant.	38
Table 3.2	First 5 entries of the true and approximate densities, $\mu = 7$, $N = 729$, $R = 2\pi$. The columns correspond to the Interior Neumann Problem (INP). The numbers in pink bold text are the digits for which the true densities ψ^{comp} computed using inbuilt MATLAB functions are constant. The numbers in blue bold text are the digits for which the densities ψ^N computed by our approach are constant.	38

Table 3.3	Differences between the first 5 entries of the true ψ^{comp} and approximate ψ^N densities, $\mu = 7$, $N = 729$, $R = 2\pi$. The first 2 columns correspond to the Interior Dirichlet Problem (IDP). The last 2 columns correspond to the Interior Neumann Problem (INP).	38
Table 3.4	Coefficients $A_{\mu, M }$ of k for disks	77
Table 3.5	Coefficients $B_{\mu, M }$ of \sqrt{k} for disks	77
Table 3.6	Coefficients $C_{\mu, M }$ of $1/\sqrt{k}$ for disks	77
Table 3.7	Coefficients $D_{\mu, M }$ of k^0 for disks	77
Table 3.8	Slopes and intercepts of lines of best fit to the Steklov-Helmholtz eigenvalues for $k = 300, \dots, 500$, for various domains of perimeter 1. The table on the left has $\mu = 1, 5, 7$ and the table on the right has $\mu = 10, 15, 20$. All slopes are $\approx \pi$.	82
Table 3.9	The subspace angles between true $(\nabla_\Gamma^{\text{circle}} u)$ and RBF approximated $(\nabla_\Gamma^{\text{approx}} u)$ tangential gradients for various circles, $N = 300$. The first column contains the wave number μ , the second column contains the radius R , the third column contains the eigenvalue number k . The fourth column contains the subspace angles between $\nabla_\Gamma^{\text{circle}} u$ and the real part of $\nabla_\Gamma^{\text{approx}} u$. The fifth column contains the subspace angles between $\nabla_\Gamma^{\text{circle}} u$ and the imaginary part of $\nabla_\Gamma^{\text{approx}} u$.	89

List of Figures

Figure 1.1	Typical domain under consideration.	1
Figure 1.2	Comparing the real part of Steklov eigenfunctions for the Laplace and Helmholtz operators, $\mu = 14$ inside the unit disk. Starting from the top left, going row-wise we show for fixed k the Steklov-Laplace (green, left) and Steklov-Helmholtz (red, right) eigenfunctions.	9
Figure 1.3	Comparing the real part of Steklov eigenfunctions for the Laplace and Helmholtz equations, $\mu = 7$ on the unit disk. Starting from the top left, going row-wise we show for fixed k the Steklov-Laplace (blue, left) and Steklov-Helmholtz (red, right) eigenfunctions.	10
Figure 1.4	Comparing the first 100 Steklov-Laplace (blue) and Steklov-Helmholtz (red) eigenvalues across various wave numbers μ for the unit disk.	11
Figure 3.1	Minimum singular values of B_μ (Dirichlet-Laplace, s_{min}^D , top, blue), $A_\mu + Id$ (Neumann-Laplace, s_{min}^N , middle, red) and C_μ (Robin-Laplace $\sigma = -1$, s_{min}^R , bottom, purple) for the unit disk with $\mu \in [0.1, 12]$. Computed eigenvalues correspond to local minimas of s_{min}^i , $i = D, N, R$. The vertical lines correspond to the true eigenvalues.	40
Figure 3.2	Minimum singular values of B_μ (Dirichlet-Laplace, s_{min}^D , top, blue), $A_\mu + Id$ (Neumann-Laplace, s_{min}^N , middle, red) and C_μ (Robin-Laplace $\sigma = 2$, s_{min}^R , bottom, purple) for the disk of radius 3 with $\mu \in [0.1, 2]$. Computed eigenvalues correspond to local minimas of s_{min}^i , $i = D, N, R$. The vertical lines correspond to the true eigenvalues.	40
Figure 3.3	Roots of sign-flipped and RBF interpolated s_{min}^i , $i = D, N, R$, for the disk of radius 3 with $\mu \in [0.1, 2]$.	43
Figure 3.4	In each subfigure we show the first N sorted eigenvalues σ_k^{true} (red) and σ_k (light blue) $k = 1, \dots, N$ and the eigenvalue of multiplicity 1 (top row). We show the absolute errors AE_k (bottom row, left) and absolute relative errors RE_k (bottom row, right) for disks with various configurations of radius R , wave number μ and N .	47

Figure 3.5	Norms of relative errors $\ RE\ _2$ of σ_k against $2N$ across various disks and wave numbers μ with respect to σ_k^{true} . In each subplot, we fix R and vary μ .	48
Figure 3.6	Norms of relative errors $\ RE\ _2$ of σ_k against $2N$ of across various disks and wave numbers μ where we set $\sigma_k^{true} := \sigma_k^{1024}(R \neq 7)$ and $\sigma_k^{true} := \sigma_k^{2048}(R = 7)$. In each subplot, we fix R and vary μ .	49
Figure 3.7	N , which is the smallest power of 2 for which $\ RE\ _2$ is of machine precision for the Steklov-Helmholtz spectrum of disks of various radii R and various wave numbers μ .	50
Figure 3.8	Comparing the computed and true, 1st and 20th Steklov-Helmholtz eigenfunctions of the unit disk, $\mu = 1$. We set $N = 500$ and $m = 150$. The subspace angles are reported in the figure titles.	53
Figure 3.9	1st and 75th Steklov-Helmholtz eigenfunctions of the disk of radius 7 with wave number 10. We set $N = 500$ and $m = 150$. The subspace angles are reported in the figure titles.	55
Figure 3.10	Steklov-Helmholtz eigenpairs of the disk of radius 7 as $\mu^2 \rightarrow \lambda^D$. In subfigures (a)-(c) show Steklov-Helmholtz eigenfunctions and in (d) shows the Dirichlet-Laplace eigenfunction. In subfigure (e) shows σ_1 against μ .	57
Figure 3.11	Steklov-Helmholtz eigenpairs of the disk of the kite as $\mu^2 \rightarrow \lambda^D$. In subfigures (a)-(c) show Steklov-Helmholtz eigenfunctions and in (d) shows the Dirichlet-Laplace eigenfunction. In subfigure (e) shows σ_1 against μ .	58
Figure 3.12	Errors of the Steklov-Helmholtz eigenvalues for annulus of radii $R_1 = 2$ and $R_2 = 4$.	62
Figure 3.13	The true solution seems to turn at different points, till a certain value of N .	63
Figure 3.14	Computed and expected eigenfunctions ($k = 20$) on M and inside an annular ring with outer radius 7 and inner radius 5, $\mu = 3$ and $N = 300$. Subfigure (a) compares the eigenfunctions inside Ω . Subfigures (b), (c) compare the eigenfunctions on M_1, M_2 respectively. The titles contain the subspace angles in degrees.	64
Figure 3.15	Convergence of Steklov-Helmholtz eigenvalues for some curves.	65
Figure 3.16	We observe that the first eigenvalue of the annular domain (circle, circle) goes to σ_1 of the disk of radius 1. Subfigure (a) shows the absolute values of the eigenfunctions.. Subfigure (b) shows σ_1 . First row corresponds to $\mu = 2$, second row corresponds to $\mu = 20$. Horizontal blue line (top right) is σ_1 of the disk of radius 1. Horizontal red line (bottom right) is σ_1 of the disk of radius 1.	67

Figure 3.17	We observe that the first eigenvalue of the annular domain (circle, butterfly) goes to σ_1 of the disk of radius 1. Subfigure (a) shows the absolute values of the eigenfunctions. Subfigure (b) shows σ_1 . First row corresponds to $\mu = 2$, second row corresponds to $\mu = 20$. Horizontal blue line (top right) is σ_1 of the disk of radius 1. Horizontal red line (bottom right) is σ_1 of the disk of radius 1.	68
Figure 3.18	Comparison of absolute eigenvalues $ \sigma_k $ of disks of varying radii. In each subfigure μ is fixed and R varies. The eigenvalues across various radii exhibit similar behaviour later on in the spectrum.	69
Figure 3.19	Comparison of absolute eigenvalues $ \sigma_k $ of disks with varying μ . In each subfigure R is fixed and μ varies. The eigenvalues across various wave numbers exhibit similar behaviour later on in the spectrum.	70
Figure 3.20	$N(0)$ for Steklov-Helmholtz eigenvalues. The figure shows heat maps of $N(0), \mu R$ for given μ, R . The two heatmaps are very similar, i.e. $N(0) \approx \mu R$.	70
Figure 3.21	Number of negative Steklov-Helmholtz eigenvalues across various curves. The first 5 subfigures are heat maps of $N(0)$ across some curves. The 6th heat map (bottom right) is of the value $ M \mu/(2\pi)$. Here $ M , \mu \in [1, 20]$.	71
Figure 3.22	Number of negative Steklov-Helmholtz eigenvalues across various curves. The first 5 subfigures are heat maps of $N(0)$ across some curves for given $\mu, M $. The 6th heat map (bottom right) is of the value $ M \mu/(2\pi)$ for given $\mu, M $. Here $ M \in [1, 50], \mu \in [1, 20]$.	72
Figure 3.23	Ratios of Steklov-Helmholtz eigenvalues of original domain over Steklov-Helmholtz eigenvalues of scaled domains. In each subfigure every row corresponds to the same wave number μ and shows the first 1000 eigenvalue ratios on the left panel and eigenvalue ratios (500-1700) on the right panel. The horizontal lines in the plots above are the scaling parameters $a > 0$.	73
Figure 3.24	Homothetic property (3.11) for the Steklov-Helmholtz eigenvalues, where Ω is the butterfly and $\mu = 10$.	75
Figure 3.25	Comparison of scaling $\sigma_k(\Omega)$ with $ M $ for disks. The Steklov-Helmholtz eigenvalues for $\mu = 1, 5, 10$ and lengths $ M = 1, 2, 3$ are shown on the left. On the right, The Steklov-Helmholtz eigenvalues scaled by $ M = 1, 2, 3$ are shown for $\mu = 1, 2, 3$.	76
Figure 3.26	Fits of the type $\sigma_k(\Omega) \approx A_{\mu, M }k + B_{\mu, M }\sqrt{k} + \frac{C_{\mu, M }}{\sqrt{k}} + D_{\mu, M }$ for disks of perimeter $ M = 1, 2, 3$ and $\mu = 1, 5, 10$.	77
Figure 3.27	Fits of the type $\sigma_k(\Omega) \approx A_{\mu, M }k + B_{\mu, M }\sqrt{k} + \frac{C_{\mu, M }}{\sqrt{k}} + D_{\mu, M }$ for the ellipse (left) and cavity (right). Perimeters $ M = 1, 2, 3$ and $\mu = 1, 5, 10$.	78

Figure 3.28	First 50 Steklov-Helmholtz eigenvalues $\{\sigma_k\}$ of some curves of length 1. In each figure the wave number μ is fixed and we consider the disk, ellipse, kite, acorn and star.	79
Figure 3.29	Plots in figure 3.28 superimposed on each other.	79
Figure 3.30	First 100 Steklov-Helmholtz eigenvalues of the disk, ellipse, kite, acorn and star with $\mu = 15$. On the right, $ M = 1$	80
Figure 3.31	First 10 perimeter scaled absolute eigenvalues for the disk, ellipse, kite, acorn and star. On the left, the perimeter $ \Gamma := M = 1$ is not 1. On the right we set $ \Gamma = 1$. In each subplot the wave number μ is fixed. For different μ a different curve has the smallest eigenvalue.	81
Figure 3.32	In the top left are the Steklov-Helmholtz eigenvalues σ_k (blue) and real part of the $\sigma_{k,\rho}$ (red). Note that $\sigma_{k,\rho} \in \mathbb{C}$ which means that our method does not work since $\rho(0) \neq \rho(2\pi)$. In the top right are the ratios of the $\sigma_k / \text{real}(\sigma_{k,\rho})$. The bottom row shows the density $\rho(t) = 10t^3$	83
Figure 3.33	Comparison of the Steklov-Helmholtz problem and boundary-weighted Steklov-Helmholtz problem. $\mu = 5$, constant density $\rho \equiv 2$ for butterfly. In subfigure (a) are the spectrum of the 2 problems and the density. The 5th eigenfunctions are compared in subfigures (b), (c). The subspace angles between the eigenfunctions are near 0.	85
Figure 3.34	Comparison of the Steklov-Helmholtz problem and boundary-weighted Steklov-Helmholtz problem. $\mu = 5$, constant density $\rho(t) = 5 \exp(-\sin t) + \cos^3(t)$ for butterfly. In subfigure (a) are the spectrum of the 2 problems and the density. The 7th eigenfunctions are compared in subfigures (b), (c). The subspace angles between the eigenfunctions are reported in the plots.	86
Figure 3.35	Scaled eigenvalues for circles with stepsize for $R = 0.001$ and $R \in [1, 3]$. The first 3 eigenvalues are shown. In subfigure (a) $k = 1, 2$. In subfigure (b) $k = 2, 3$. In each subfigure, on the left is $ M \sigma_k$ and on the right $\sqrt{ \Omega }\sigma_k$	91
Figure 3.36	10 Experiments for the first 3 Steklov-eigenvalues of disks with radii in $[1, 3]$. Subfigure(a) shows experiments for $k = 1$, subfigure(b) shows experiments for $k = 2$ and subfigure(c) shows experiments for $k = 3$. Each subfigure show iterations of the radii R (left), the eigenvalue σ_k (middle) and the shape derivative σ'_k (right) for each of the 10 experiments. For $k = 1, 3$ the optimization converges to a Dirichlet-Laplace eigenvalue.	92
Figure 3.37	10 Experiments for the first Steklov-eigenvalues of the deformed ellipse for $\kappa \in [0, 1]$. Subfigure(a) shows the actual scaled eigenvalues for $k = 1$, subfigure(b) shows experiments for $k = 1$. Subfigure(b) show iterations of the radii R (left), the eigenvalue σ_k (middle) and the shape derivative σ'_k (right) for each of the 10 experiments.	92

Figure 3.38	10 Experiments for the first Steklov-eigenvalues of the deformed ellipse for $\kappa \in [1, 6]$. Subfigure(a) shows the actual scaled eigenvalues for $k = 1$, subfigure(b) shows experiments for $k = 1$. Subfigure(b) show iterations of the radii R (left), the eigenvalue σ_k (middle) and the shape derivative σ'_k (right) for each of the 10 experiments. Here $ M = 1$ is fixed.	93
Figure 4.1	Locating zeros using algorithm 4 for egg with curvature 0.2, $n_{RI} = 4$ and $N = 120$	95
Figure 4.2	Possible transmission eigenvalues in $[6, 12]$ of egg with curvature 0.2, $n_{RI} = 4$ using Algorithm 4. Subfigure (a) shows the curve of minimum singular values s_{min} . Subfigure (b) shows the located zeros of RBF after sign flipping s_{min}	96
Figure 4.3	Refined search of μ_T in $[6, 7]$ for the egg with curvature 0.2.	97
Figure 4.4	Refined search of μ_T in $[10, 11]$ for the egg with curvature 0.2.	98
Figure 4.5	A couple of transmission eigenfunctions for the egg with curvature 0.2. Both subfigures show real part of eigenfunctions for $n_{RI} = 1$ (green, left) and $n_{RI} = 4$ (red, right). The bottom row shows the eigendensity ϕ	98

Chapter 1

Introduction

This thesis is concerned with the discretization and computation of an elliptic eigenvalue problem for bounded domains in \mathbb{R}^2 . Our main focus is on the Steklov-Helmholtz eigenvalue problem, where we require that the normal derivative of the solution is a multiple of the solution on the boundary. This is the *Steklov* boundary condition. We search for the eigenfunctions and eigenvalues using an ansatz based on the fundamental solution of the Helmholtz equation in the plane. This *boundary-eigenvalue* problem has been extensively studied both computationally and analytically for the Laplacian [GP17] and we hope to provide useful information for similar studies on the Helmholtz operator.

In this thesis we implement a numerical scheme to approximate the Steklov-Helmholtz-eigenpairs. Our method involves reformulating the Steklov-Helmholtz eigenvalue problem into a boundary integral equation via the use of layer potentials. We adapt our approach to solve the Dirichlet/Neumann/Robin-Laplace eigenvalue problems and the transmission eigenvalue problem [CK17]. However, we cannot apply our method to the Steklov-Laplace eigenvalue problem since the fundamental solution of the Helmholtz equation does not converge to the fundamental solution of the Laplace equation in the plane.

1.1 Notation and thesis structure

We use the following notation throughout this thesis unless specified otherwise. We consider a bounded domain called $\Omega \subset \mathbb{R}^2$ that has a sufficiently smooth boundary M (at least Lipschitz, see [Definition 1.6.16](#)) and outer unit normal ν (see [Figure 1.1](#)).

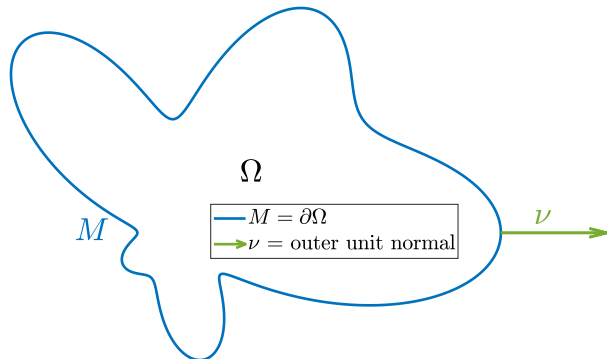


Figure 1.1: Typical domain under consideration.

This thesis is primarily about the Helmholtz operator, $-\Delta - \mu^2$ with the real *wave number* $\mu \in \mathbb{R}$. The Helmholtz equation $-(\Delta + \mu^2)u = 0$ has the fundamental solution $G_\mu(x, y) = \frac{i}{4}H_0^1(\mu|x - y|)$, $x \in \mathbb{R}^2 \setminus \{y\}$, where H_0^1 is the Hankel function of the first kind and of order 0 (see [Equation 1.15](#)).

The operators concerned with the eigenvalue problems in this thesis are maps on *Sobolev spaces* (see [Section 1.6](#)). We will use the standard notation for Sobolev spaces having *weak derivatives* in $L^2(D)$, $H^s(D) := W^{s,2}(D)$, $|s| \leq 2$ where D is either the domain Ω or its boundary M . The closure of the space of infinitely differentiable functions $C_c^\infty(\Omega)$ in $H^s(\Omega)$ is denoted by $H_0^s(\Omega)$.

Remark 1.1.1 (Notation of Hankel function and a Sobolev space). *The Hankel function $H_0^1(x)$, $x > 0$ is not to be confused with the space $H_0^1(\Omega)$, $\Omega \subset \mathbb{R}^2$.*

The various eigenvalue problems that we consider are listed below.

- Let $\alpha, \beta, \sigma \in \mathbb{R}$ be fixed and consider the *Laplace eigenvalue problem*: find $\lambda \in \mathbb{R}$, $u \in C^2(\Omega) \cap C(M)$ such that,

$$\begin{cases} -\Delta u = \lambda u & \text{in } \Omega, \\ \alpha \frac{\partial u}{\partial \nu} = \beta \sigma u & \text{on } M. \end{cases} \quad (1.1)$$

[Table 1.1](#) summarizes the conditions which give the 3 standard Laplace eigenvalue problems.

Parameter values		Name		Eigenvalue notation
$\frac{\alpha}{\beta\sigma} = 0$		Dirichlet-Laplace		$\lambda^D := \lambda$
$\frac{\beta\sigma}{\alpha} = 0$		Neumann-Laplace		$\lambda^N := \lambda$
$0 \neq \alpha = \beta$ and $0 \neq \sigma$		Robin-Laplace		$\lambda^R := \lambda$

Table 1.1: Standard Laplace eigenvalue problems.

- For a given wave number μ , the *Steklov-Helmholtz eigenvalue problem* is to find: *eigenvalues* $\sigma \in \mathbb{R}$ and $u \in H^1(\Omega) \cap H^{1/2}(M)$ such that,

$$\begin{cases} -\Delta u - \mu^2 u = 0 & \text{in } \Omega, \\ \frac{\partial u}{\partial \nu} = \sigma \rho u & \text{on } M, \end{cases} \quad (1.2)$$

where μ is a fixed wave number and ρ is a positive bounded function. We immediately observe that the Robin-Laplace eigenvalue problem (1.1) and Steklov-Helmholtz eigenvalue problem (1.2) have similar structure in their form. The main difference is that the Robin-Laplace problem is a *volume type* eigenvalue problem (the spectral parameter is in Ω) for the Laplacian, whereas the Steklov-Helmholtz problem is a *surface type* eigenvalue problem (the spectral parameter is on M) for the Helmholtz operator.

- For a given refractive index $n_{RI} > 0$, the *transmission eigenvalue problem* is to find: $\mu_T \in \mathbb{C}$, $v, w \in L^2(\Omega)$ and $v - w \in H^2(\Omega)$ such that,

$$\begin{cases} \Delta v + \mu_T^2 v = 0 \text{ in } \Omega, \\ \Delta w + n_{RI} \mu_T^2 w = 0 \text{ in } \Omega, \\ v = w \text{ on } M, \\ \partial_\nu v = \partial_\nu w \text{ on } M. \end{cases} \quad (1.3)$$

Next, we describe notation and terminology associated with the eigenvalues.

- We abuse the term *spectrum* to mean the *point spectrum*, i.e the set of eigenvalues.
- As summarized in [Table 1.1](#) above, the Dirichlet, Neumann and Robin eigenvalues of $-\Delta$ are denoted by λ^D , λ^N and λ^R respectively.
- The sorted k th Steklov-Helmholtz eigenvalue is denoted by σ_k in general. Depending on the context we make modifications to this notation. If the domain needs to be emphasized we write $\sigma_k(\Omega)$ and if the wave number is also required we write $\sigma_k(\Omega, \mu)$. We write $\sigma_{\rho, k}$ where $\rho \not\equiv 1$ is a boundary weight. we emphasize half the number of discretization points N , by writing σ_k^N . In case of the disk where we know the actual eigenvalues while comparing with the approximate eigenvalues σ_k , we write σ_k^{true} .
- The k th sorted transmission eigenvalue is denoted by $\mu_{T_{k, n_{RI}}}$. If the refractive index is made clear, then we simply write μ_{T_k} .

We now describe the structure of this thesis.

1. In [Chapter 1](#), we review some of the current state of the art of the Steklov problem (for the Laplace and Helmholtz operators). We also go over some of the required theory for the work in this thesis.
2. In [Chapter 2](#), we go over our proposed strategy to solve the Steklov-Helmholtz problem for bounded $\Omega \subset \mathbb{R}^2$ with smooth M .
3. In [Chapter 3](#) we test our method on the disk where the solution is known for the standard Laplace eigenvalue problems and the Steklov-Helmholtz eigenvalue problem. We then perform experiments on various domains to check for convergence and test for properties of the Steklov-Helmholtz spectrum. We observe a Weyl-type law for the asymptotics of the spectrum and close the chapter with some experiments on shape optimization for the k th Steklov-eigenvalue.
4. In [Chapter 4](#) we use the discretized operators built in [Chapter 2](#) to solve the transmission eigenvalue problem. We suggest a search algorithm for the transmission eigenvalues.

5. In [Chapter 5](#) we summarize and discuss our work and describe future work to be done.
6. In [Appendix A](#) we list the parametrizations for the curves we have tried our work on. In [Appendix B](#) we provide the MATLAB code written for this thesis.

1.2 Thesis contributions

The work in this thesis is focused on a numerical study of the Steklov-Helmholtz eigenvalue problem. After reformulating the Steklov-Helmholtz eigenvalue problem using boundary layer potentials, we approximate the solutions of certain boundary value problems related to the Helmholtz operator.

To begin, we briefly summarize work already done on the Steklov-Laplace and Steklov-Helmholtz eigenvalue problems, and discuss key differences between the eigenfunctions of the two problems for disks.

For the Steklov-Helmholtz eigenvalue problem on Ω , we approximate the eigenpairs using layer potentials. In this setting, we provide code for approximations of the single layer and the adjoint of the double that are required to solve this problem. We observe exponential convergence of the Steklov-Helmholtz eigenvalues for various curves of genus 0 and 1 with dependence on the wave number μ and the number of discretization points. Incidentally, we can use these potential layers for other boundary value problems such as the Dirichlet/Neumann/Robin-Laplace eigenvalue problems and the transmission eigenvalue problem. We expect the applicable use of these layer potentials in other boundary value problems that they arise in. Further, modifications to the code can be made to build other layer potentials as well. Through our experiments, we establish a homothety result for the Steklov-Helmholtz eigenvalue problem, and make conjectures about the number of negative eigenvalues, and the asymptotic behaviour of the spectrum. Further, we investigate a shape optimization problem for the k th eigenvalue.

1.3 History of the Steklov-Laplace problem

The Steklov problem was introduced by Vladimir Andreevich Steklov in a talk at the Kharkov Mathematical Society in December 1895. The impact of his works is well documented in [\[Kuz+14\]](#). His focus was the Steklov-Laplace problem: *to find a solution u and eigenvalues σ such that*

$$\begin{cases} -\Delta u = 0 & \text{in } \Omega, \\ \frac{\partial u}{\partial \nu} = \sigma \rho u & \text{on } M, \end{cases} \quad (1.4)$$

where ρ is a non-negative bounded weight function. Most of the literature that we review concerns bounded domains with Lipschitz boundaries where the Steklov spectrum is discrete, $0 = \sigma_0 < \sigma_1 \leq \sigma_2 \leq \dots$ (see Section 7.1.1 in [\[LMP22\]](#) and Section 2 in [\[AM12\]](#)). Physically, this condition models the vibration of a free membrane with mass concentrated along the boundary. The incorrect spelling

of the surname “Stekloff”, has propagated through time including when R. Weinstock brought attention to this problem in 1954 through his work in [Wei54] for simply connected domains. Weinstock discovered a bound on the first non-zero Steklov-Laplace eigenvalue,

$$\sigma_1 \leq \frac{2\pi}{\int_M \rho \, ds}. \quad (1.5)$$

Further, for boundary weight $\rho \equiv 1$, $\sigma_1 \leq \frac{2\pi}{|M|}$. Weinstock showed that equality is attained if and only if Ω is a disk. From this he concluded that for curves of fixed length $|M|$, the circle has the largest σ_1 . An extension of the bound discovered by Weinstock was proposed J. Hersch, L. Payne and M. Schiffer in [HPS74] and was shown to be sharp by A. Girouard and I. Polterovich in [GP10]. In the same work, Girouard et al also studied multiply connected domains and some mixed Steklov type problems. In the context of Weinstock’s work they showed that $\sigma_k \leq \frac{2\pi k}{|M|}$. Having established bounds on Steklov-Laplace eigenvalues, a natural question is on their asymptotic behaviour. For simplicity, we let the boundary weight $\rho \equiv 1$. The asymptotic behaviour is based on counting functions, i.e. the number of eigenvalues less than a given number. Precisely for $x \in \mathbb{R}^+$, let $N(x) = \#\{k, \sigma_k \leq x\}$ be the number of Steklov-Laplace eigenvalues less than x and note that $N(x) = 0, \forall x < 0$, which in contrast is not true for the Steklov-Helmholtz eigenvalues as we shall see. Theorem 7.2.1 [LMP22] states a Weyl type law on Steklov-Laplace eigenvalues. In 2 dimensions, the asymptotic behaviour of the counting function goes as (see equations 2,3 in [Gir+21]),

$$N(x) = \frac{x}{\pi} |M| + \mathcal{O}(1), \quad x \rightarrow \infty, \quad (1.6)$$

or equivalently,

$$\sigma_k = \frac{\pi k}{|M|} + \mathcal{O}(1), \quad k \rightarrow \infty. \quad (1.7)$$

The asymptotic relations (1.6) and (1.7) exemplify the natural connection between the spectrum and the volumetric properties of the domain. We note that the Steklov-Laplace spectrum of domains with the same volume exhibit similar asymptotic behaviour. The asymptotic behaviour of the Steklov-Laplace eigenvalues of curvilinear polygons is discussed in Section 7.3.1 of [LMP22]. The authors show in Theorem 7.3.2, that the Steklov-Laplace eigenvalues asymptotically are approximately the square roots of the eigenvalues of the quantum graph Laplacian as in equation 7.3.1 in [LMP22]. Moving on to further applications, consider the mixed Steklov-Laplace problem (also called the *Sloshing problem*),

$$\begin{cases} -\Delta u = 0 & \text{in } \Omega, \\ \frac{\partial u}{\partial \nu} = \sigma u & \text{on } \Gamma, \\ \frac{\partial u}{\partial \nu} = 0 & \text{on } M \setminus \Gamma. \end{cases} \quad (1.8)$$

Modifications to the Poincaré inequality (a special case of which Steklov had proved in 1897) give rise to a boundary-domain inequality for Ω , a bounded Lipschitz domain in \mathbb{R}^d , $d \geq 2$ with $\Gamma \subseteq M$,

$$\left\| u - \frac{\int_{\Gamma} u \, ds}{|\Gamma|} \right\|_{L^2(\Gamma)} \leq C \|\nabla u\|_{L^2(\Omega)}.$$

The sharp constant in this inequality is $C = 1/\sqrt{\sigma_1^S}$ where σ_1^S is the smallest positive eigenvalue of problem (1.8). For special domain configurations in $\mathbb{R}^2, \mathbb{R}^3$ the eigenvalues of this problem are the *sloshing frequencies*. These are frequencies of free oscillations of a liquid in containers and can be interpreted as resonant frequencies. In 2012, R. Krechetnikov and H. Mayer won the Fluid Dynamics Ig Nobel prize for their work on sloshing frequencies [MK12].

Isoperimetric inequalities have been an area of great interest for the Steklov problem. The goal is to find bounds on eigenvalues with some dependence on the shape (such as Weinstocks's inequality, Equation 1.5). Work on maximizing the first eigenvalue of the Laplace-Beltrami operator by Hersch in 1970 brought interest to work on extremal metrics and was extended to Steklov eigenvalues on surfaces with boundary in the classical works by A. Fraser and R. Schoen in [FS09], [FS12]. Their work was on extremal metrics for the first Steklov eigenvalue on genus zero surfaces with multiple boundary components, and they proved existence of maximizers. Another direction is to consider shape optimization problems with the help of shape calculus. In [CDM22], the authors derive shape (semi)derivatives for various eigenvalue problems including the Steklov-Laplace problem. Initial studies for the Steklov-Laplace focus on maximizing or minimizing the first eigenvalue among shapes of fixed length/area/volume. Generally, the choice of constraint depends on the type of boundary condition. In the Steklov-Laplace problem the perimeter is fixed since all the mass is concentrated there. A vast amount of numerical work has been done on maximizing Steklov eigenvalues with techniques using shape calculus and conformal mapping, see [AKO17], [AK19], [Ant21], [OKO21].

In [Wan+18] the authors perform extrinsic shape analysis using the Steklov-Laplace eigenvalue problem and use layer potentials and finite element methods to capture spatial embedding of a shape up to rigid motion (translation+rotation) in \mathbb{R}^3 . Extrinsic shape analysis examines the surface as the outer boundary of a volume as compared to intrinsic shape analysis which relies on quantities like geodesic distances that can be measured without leaving the outer surface. As the authors describe, intrinsic geometry is an ineffective description of shape for many applications since the spatial embedding information is lost and because the intrinsic perspective is a counterintuitive way to describe the shapes of many real-world objects. In terms of operators, the *extrinsic* Dirichlet-to-Neumann map replaces the *intrinsic* Laplace-Beltrami map.

In [IN22], the authors use the Dirichlet-to-Neumann map with the theory of layer potentials to provide a spectral approximation theorem showing an exponential numerical evaluation depending on the number of Steklov eigenfunctions used and the number of discretization points. We use a similar approach in this thesis.

1.4 History of the Steklov-Helmholtz problem

While Steklov posed his boundary condition for the Laplacian, we can define it for other elliptic operators (see Chapter 4 in [McL00]). In this thesis we numerically approximate the Steklov spectrum of the Helmholtz operator $-\Delta - \mu^2$ with real wave number μ for bounded and smooth domains in \mathbb{R}^2 . The Helmholtz operator is elliptic (see Chapter 9 in [McL00]) and self-adjoint for real wave number μ (see Section 1.5). We recall the problem (1.2) which is to find Steklov-Helmholtz eigenpairs (σ, u) such that,

$$\begin{cases} -\Delta u - \mu^2 u = 0 & \text{in } \Omega, \\ \frac{\partial u}{\partial \nu} = \sigma \rho u & \text{on } M, \end{cases}$$

where $\mu \in \mathbb{R}$ is the fixed wave number and ρ is a positive and bounded function. This problem is isospectral with the Dirichlet-to-Neumann map and since M is Lipschitz, has a discrete spectrum of non-zero real eigenvalues (see Section 7.4.1 in [LMP22]). We briefly go over work already done on this problem. In [TGH98], the authors consider the modified Helmholtz equation with $\mu = i$, i.e. $-\Delta u + u = 0$ and the Steklov boundary condition. It is one of the first works (to our best knowledge) for a Steklov problem that reformulates the problem to a boundary integral equation using layer potentials together with the fundamental solution. Using a non-uniform grid their method has an error of $\mathcal{O}(h^2)$, where h is the largest spacing between any two grid points. An extension of this work in [HL04] considers the Steklov problem for wave number $\mu \in \mathbb{R}$, $-\Delta u + \mu^2 u = 0$ (along with the Laplace equation, i.e. $\mu = 0$). Relying on the trapezoidal rule and Richardson extrapolation, the authors demonstrate $\mathcal{O}(h^3)$ convergence. Numerical approaches for the modified Helmholtz equation with the Steklov boundary condition have recently been studied in [CG23]. They use the finite element method for their study which addresses three questions, including the asymptotic behaviour of the k th eigenvalue as $\mu \rightarrow \infty$ for planar domains. In [MM20] the authors compare three different Discontinuous Galerkin discretization schemes for the non-self adjoint Steklov-Helmholtz problem, i.e. when $\mu \in \mathbb{C}$ in general. As this problem has mass concentrated at the boundaries, meshing the entire domain involves extra work and computational costs. For the modified Helmholtz sloshing problem (homogeneous Dirichlet and Steklov boundary conditions on parts of M), in [Tur21] the author uses the dual reciprocity boundary element method (DRBEM) which also relies on meshing the domain. This approach has a quadratic order of convergence and numerically Weyl's law is observed. One of the benchmark works for this problem is [Cak+16], where the authors test sensitivity of Steklov eigenvalues to changes in refractive index of the inhomogeneous medium that the domain encompasses. Numerically, they also use the finite element method, but elucidate many important properties of the spectrum analytically (see Sections 2-4). A couple of recent works use layer potentials and the fundamental solution of the Helmholtz equation, similar to our strategy. In the first work [MS22], the authors consider the non-self adjoint Steklov-Helmholtz (i.e. $\mu \in \mathbb{C}$) problem. They use boundary layers with the fundamental solution and spectral indicator methods to

close in on complex Steklov-Helmholtz eigenvalues, by refining regions that probably contain them. This method works well to find the eigenvalues on domains in \mathbb{R}^2 (not necessarily smooth) but eigenfunctions are not computed. In the second work, [DT23] the authors use boundary layers for the solution of Navier scattering problems with Dirichlet boundary condition. They provide stability estimates for their method and demonstrate at least super-algebraic convergence. In [SXY23], the authors propose a Dirichlet-Neumann algorithm using neural network extension operators to solve elliptic interface problems. They observe that their algorithm performs better compared to other alternatives. A couple of great references are [Auc05] and [LMP22], the latter of which we follow closely to describe the Dirichlet to Neumann map in [Section 1.7](#).

1.4.1 The one dimensional Steklov-Helmholtz eigenvalue problem

In one dimension with $\Omega = (a, b) \subset \mathbb{R}$, the Steklov-Helmholtz problem is an eigenvalue problem for the one dimensional differential operator $-\frac{d^2}{dx^2} - \mu^2$. This can be seen as a special type of Sturm-Liouville problem,

$$\begin{cases} -u'' - \mu^2 u = 0, \\ u'(a) = -\sigma u(a); \quad u'(b) = \sigma u(b). \end{cases} \quad (1.9)$$

Note that the boundary condition in [Equation 1.9](#) has two components, one for each end of the interval (a, b) . Let $x \in \mathbb{R}$ and we assume the outward normal pointing toward $+\infty$, which gives a negative sign to the boundary equation at $x = a$. The roots of the auxiliary equation $-m^2 - \mu^2 = 0$ are $m = \pm i\mu$ and hence

$$\begin{aligned} u(x) &= c_1 e^{-i\mu x} + c_2 e^{i\mu x} = c_3 \cos(\mu x) + c_4 \sin(\mu x), \\ u'(x) &= i\mu(-c_1 e^{-i\mu x} + c_2 e^{i\mu x}) = \mu(-c_3 \sin(\mu x) + c_4 \cos(\mu x)). \end{aligned}$$

There are many ways of computing the eigenvalues σ and since we have only two equations, we directly compute them. As we will see later, this is the same as looking for zero determinant solutions of the corresponding matrix system (3.8). Applying the boundary conditions we see,

$$\sigma_k = i\mu \frac{c_1 e^{-i\mu a} - c_2 e^{i\mu a}}{c_1 e^{-i\mu a} + c_2 e^{i\mu a}} = i\mu \frac{-c_1 e^{-i\mu b} + c_2 e^{i\mu b}}{c_1 e^{-i\mu b} + c_2 e^{i\mu b}}, \quad k = 1, 2. \quad (1.10)$$

Equating the two forms of the eigenvalues and solving for c_2 in terms of c_1 we get,

$$\begin{aligned} (c_1 e^{-i\mu a} - c_2 e^{i\mu a})(c_1 e^{-i\mu b} + c_2 e^{i\mu b}) &= (-c_1 e^{-i\mu b} + c_2 e^{i\mu b})(c_1 e^{-i\mu a} + c_2 e^{i\mu a}) \\ c_2 &= \pm c_1 e^{-i\mu(a+b)}. \end{aligned}$$

Putting this back in [Equation 1.10](#) we get only two distinct Steklov-Helmholtz eigenvalues with opposite signs,

$$\sigma_k = i\mu \frac{e^{-i\mu a} \mp e^{-i\mu b}}{e^{-i\mu a} \pm e^{-i\mu b}} = i\mu \frac{-e^{-i\mu b} \pm e^{-i\mu a}}{e^{-i\mu b} \pm e^{-i\mu a}}, \quad k = 1, 2. \quad (1.11)$$

1.4.2 Comparing Steklov-Laplace and Steklov-Helmholtz eigenfunctions of the unit disk

The Steklov-Laplace eigenvalue problem and the Steklov-Helmholtz eigenvalue problem with wave number μ can be solved on the disk using polar coordinates and separation of variables. Using the solutions on the boundary M where $r = 1$, with the Steklov boundary condition, noting that the normal direction is simply the radial direction (i.e. $\partial_\nu \equiv \partial_r$), we get the corresponding Steklov eigenvalues. In [Table 1.2](#) we summarize the Steklov eigenpairs, where $0 \leq r \leq 1$, $\theta \in [0, 2\pi)$ and $J_k(x)$ is the Bessel function of order k evaluated at $x \geq 0$ (see [Equation 1.13](#)).

Operator	Steklov eigenfunctions, $k \in \mathbb{N}_0$	Steklov eigenvalues, $k \in \mathbb{N}_0$
$-\Delta (\mu = 0)$	$u_k^L(r, \theta) := r^k \exp(ik\theta)$	$\sigma_k^L := k$
$-\Delta - \mu^2$	$u_k(r, \theta) := u_k^H(r, \theta) = J_k(\mu r) \exp(ik\theta)$	$\sigma_k := \sigma_k^H = \frac{\mu J'_k(\mu)}{J_k(\mu)}$

Table 1.2: Comparison of Steklov-Laplace and Steklov-Helmholtz eigenpairs for the unit disk.

For both problems, σ_0^L and σ_0 have multiplicity one. For $k > 0$ the eigenvalues have multiplicity two. Inside the disk the eigenfunctions have similar angular behaviour, but different radial behaviour. We show this in [Figure 1.2](#) for the unit disk with wave number $\mu = 14$. Since $\sigma_{2k-1} = \sigma_{2k}$, $k \geq 1$, we consider $k = 0$ and odd eigen numbers $k = 1, 3, \dots, 29$. We observe that the Steklov-Helmholtz eigenfunctions approach the Steklov-Laplace eigenfunctions as k increases.

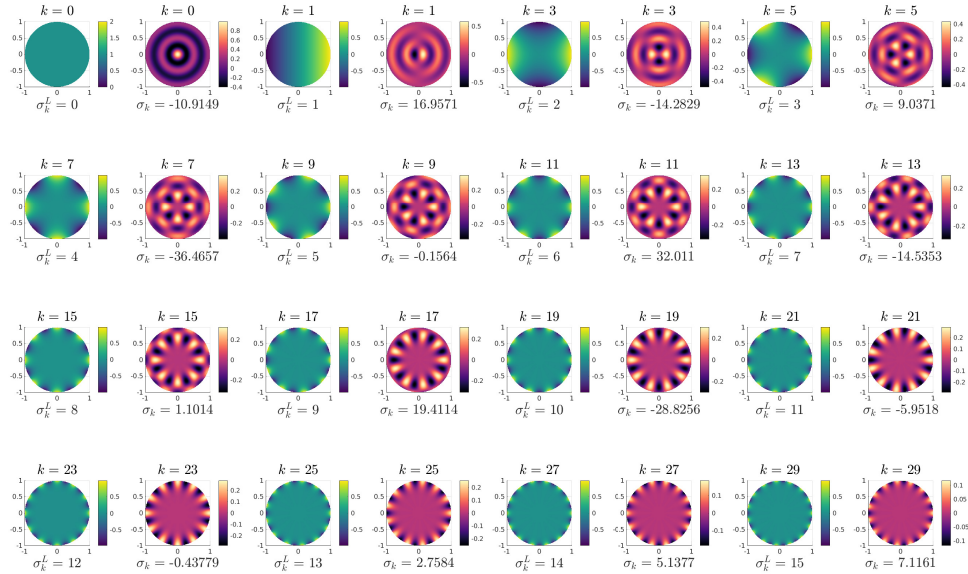
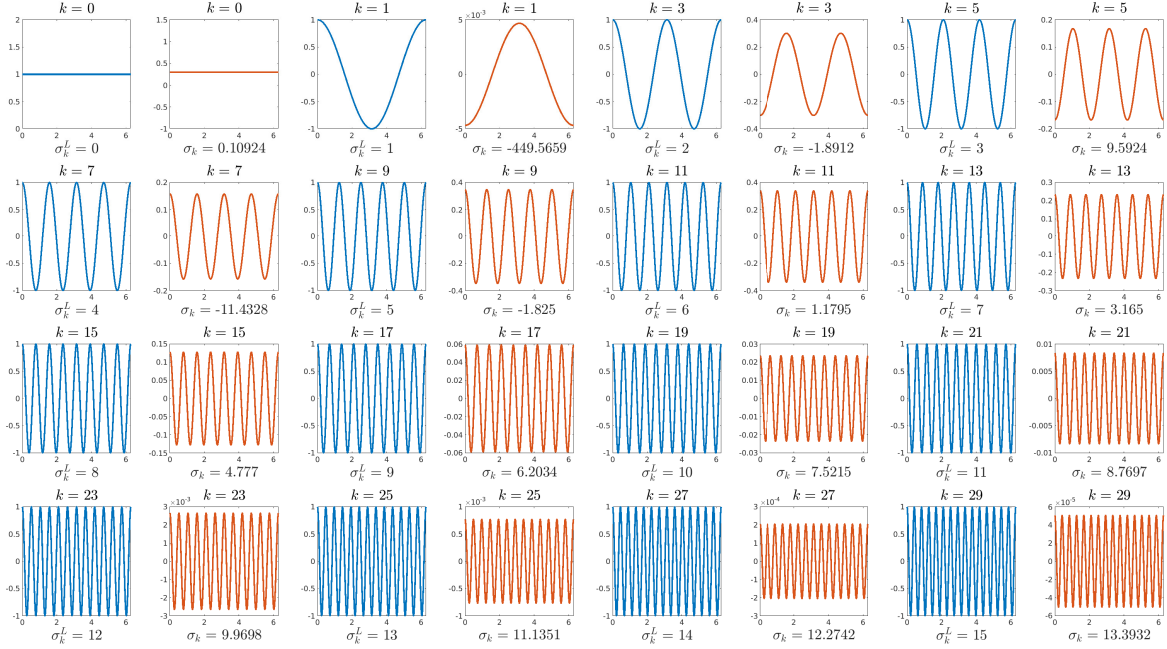


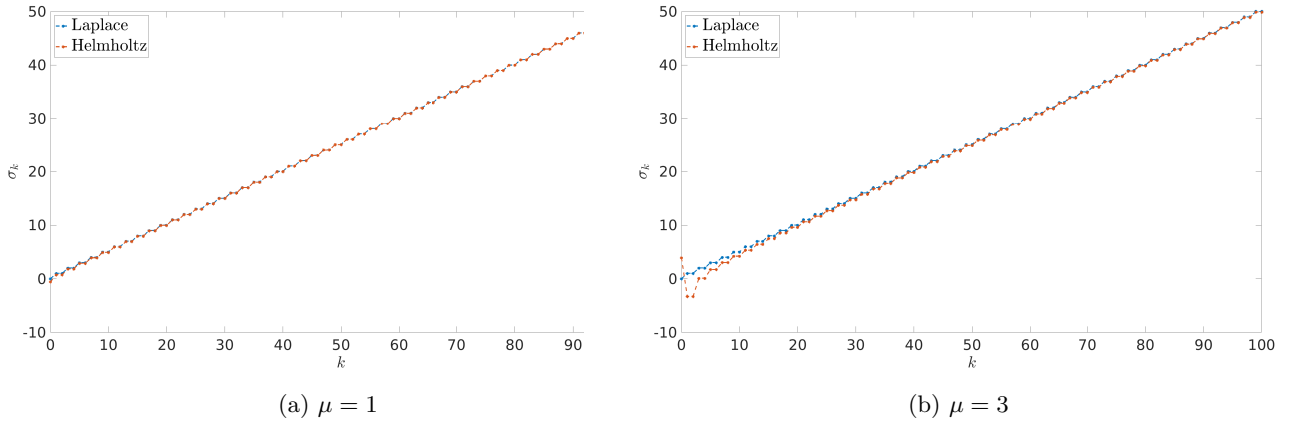
Figure 1.2: Comparing the real part of Steklov eigenfunctions for the Laplace and Helmholtz operators, $\mu = 14$ inside the unit disk. Starting from the top left, going row-wise we show for fixed k the Steklov-Laplace (green, left) and Steklov-Helmholtz (red, right) eigenfunctions.

However, on M we have $u_k^L(1, \theta) = \exp(ik\theta)$ and $u_k(1, \theta) = J_k(\mu) \exp(ik\theta) = J_k(\mu)u_k^L(1, \theta)$. So on the boundary of the disk, the Steklov-Laplace and Steklov-Helmholtz eigenfunctions are multiples of each other and in some sense the same (since scaled eigenfunctions are still eigenfunctions). In [Figure 1.3](#) we show this behaviour for $\mu = 7$, by looking at the boundary traces. As expected, we note that on the boundary M ($r = 1$) for the unit disk, the Steklov-Laplace and Steklov-Helmholtz eigenfunctions are multiples of each other.



[Figure 1.3](#): Comparing the real part of Steklov eigenfunctions for the Laplace and Helmholtz equations, $\mu = 7$ on the unit disk. Starting from the top left, going row-wise we show for fixed k the Steklov-Laplace (blue, left) and Steklov-Helmholtz (red, right) eigenfunctions.

In [Figure 1.4](#) we compare the first hundred Steklov eigenvalues of the Laplace and Helmholtz operators on the disk for various wave numbers μ .



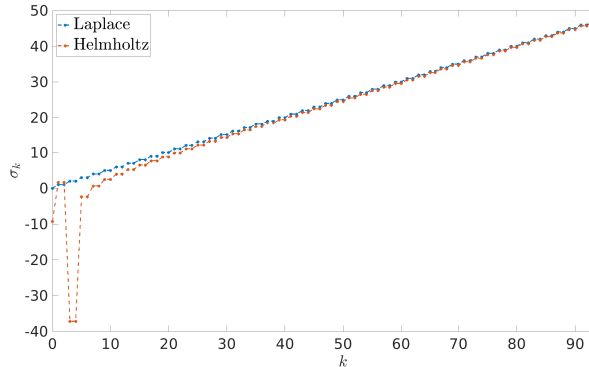
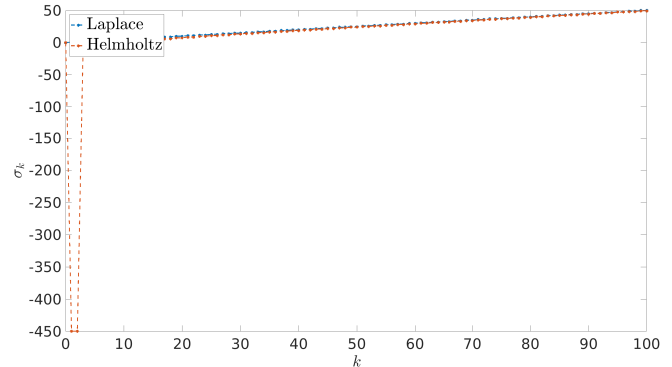
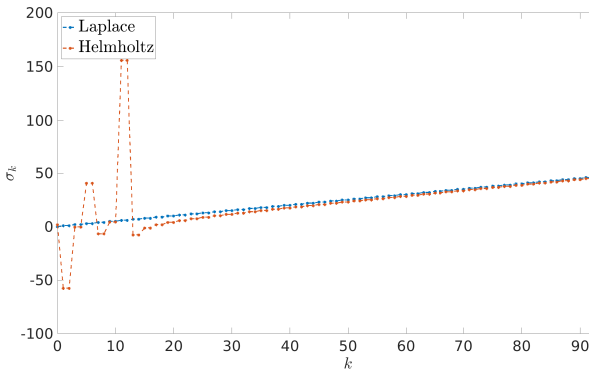
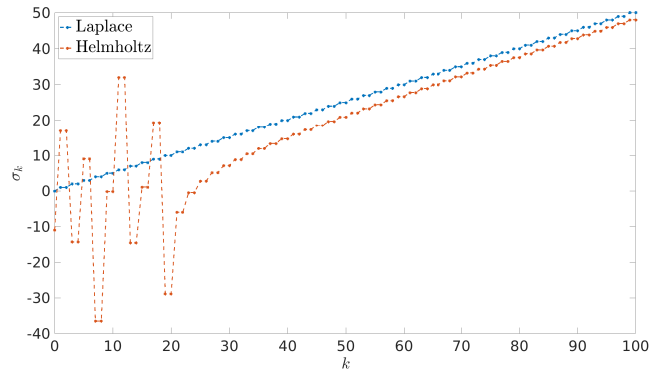
(c) $\mu = 5$ (d) $\mu = 7$ (e) $\mu = 10$ (f) $\mu = 14$

Figure 1.4: Comparing the first 100 Steklov-Laplace (blue) and Steklov-Helmholtz (red) eigenvalues across various wave numbers μ for the unit disk.

We observe that as $k \rightarrow \infty$, the Steklov-Helmholtz eigenvalues approach the Steklov-Laplace eigenvalues. This is expected on considering the variational principles as given in Theorems 7.1.9 and 7.4.2 in [LMP22] (which we discuss in [Section 1.7.3](#)).

Summarizing, if we compare the Steklov eigenpairs for the Laplace and Helmholtz equations on the unit disk, we observe that as the eigenvalue number k increases, the Steklov-Helmholtz eigenpairs approach the Steklov-Laplace eigenpairs. Further, the value of k for which the eigenpairs get *closer* increases as μ increases. Another interesting point is that some Steklov-Helmholtz eigenvalues are negative, which can be inferred from their variational principle (see [Section 1.7.3](#)).

1.5 The Helmholtz equation in \mathbb{R}^2

Our approach to study the eigensolutions of the Steklov-Helmholtz eigenvalue problem uses a potential layer ansatz for the Steklov-Helmholtz eigenfunctions based on the fundamental solution of the Helmholtz equation in \mathbb{R}^2 (see [Equation 2.3](#)). In this section, we briefly describe the fundamental solution of the Helmholtz equation and this discussion is based on Section 3.4 in [CK13]. Recall

that the Helmholtz equation for real wave number μ is

$$-\Delta u - \mu^2 u = 0, \quad \Omega \subset \mathbb{R}^2, \quad (1.12)$$

where we require Ω to be bounded with an at least Lipschitz boundary $M := \partial\Omega$. Consider two functions $U_1(x_1, x_2) = e^{i\mu(x_1+x_2)/\sqrt{2}}$ and $U_2(x, y) = x_2 e^{i\mu x_1}$. Direct calculation shows that they solve [Equation 1.12](#) and hence there are infinitely many solutions of [Equation 1.12](#). To ensure a unique solution we impose the Sommerfeld radiation condition at infinity, $\lim_{r \rightarrow \infty} \sqrt{r} (\partial_r - i\mu) u = 0$, where $r = \sqrt{x_1^2 + x_2^2}$ (see Chapter 2 and equation 3.85 in [\[CK13\]](#)). This condition physically characterizes outgoing waves. In this setting, the solution to the Helmholtz equation is known and stems from Bessel's equation of order 0. Bessel's equation of order n is given by $t^2 f''(t) + t f'(t) + (t^2 - n^2) f(t) = 0$ and has two linearly independent solutions J_n and Y_n , called the Bessel and Neumann functions of order $n \in \mathbb{N}_0$ respectively. We recall their series expansions

$$J_n(t) = \sum_{p=0}^{\infty} \frac{(-1)^p}{p!(n+p)!} \left(\frac{t}{2}\right)^{n+2p}, \quad \text{for } t \in \mathbb{R} \quad (1.13)$$

and

$$\begin{aligned} Y_n(t) &= \left(\frac{2}{\pi}\right) \left\{ \ln \frac{t}{2} + C \right\} J_n(t) - \frac{1}{\pi} \sum_{p=0}^{n-1} \frac{(n-1-p)!}{p!} \left(\frac{2}{t}\right)^{n-2p} \\ &\quad - \frac{1}{\pi} \sum_{p=0}^{\infty} \frac{(-1)^p}{p!(n+p)!} \left(\frac{t}{2}\right)^{n+2p} \{ \xi(p+n) + \xi(p) \}, \quad \text{for } t \in (0, \infty), \end{aligned} \quad (1.14)$$

where

$$\xi(p) = \sum_{m=1}^p \frac{1}{m} \quad \text{for } p \in \mathbb{N}$$

and

$$C := \lim_{p \rightarrow \infty} (\xi(p) - \ln p) \quad \text{is Euler's constant (see equation 3.75 in [\[CK13\]](#))}.$$

The second term in [Equation 1.14](#) is 0 when $n = 0$. It is known that these solutions are real analytic for $t \in \mathbb{R}$ for the Bessel function and for $t \in \mathbb{R}^+$ for the Neumann function. The fact that they solve Bessel's equation can be verified by direct substitution, while analyticity in t is obtained by the ratio test. The Hankel functions of order n of the first kind is defined by $H_n^1(t) := J_n(t) + iY_n(t)$, $t > 0$. The fundamental solution of the Helmholtz [Equation 1.12](#) is given by

$$G_\mu(x, y) := \frac{i}{4} H_0^1(\mu |x - y|) \quad \text{for } x \neq y. \quad (1.15)$$

Referring to equations 4.1, 4.2, 4.6, 4.7 and Chapter 9 in [\[McL00\]](#) we briefly show that the Helmholtz operator is self-adjoint for real wave number μ . In context of the associated sesquilinear

form Φ associated with the Helmholtz operator $-\Delta - \mu^2$ we have,

$$\Phi(u, v)_\Omega = \int_\Omega \overline{\nabla u} \cdot \nabla v - \mu^2 \bar{u}v = \int_\Omega \overline{\nabla u \cdot \nabla v} - \overline{\mu^2 u \bar{v}} = \overline{\int_\Omega \nabla u \cdot \nabla v - \mu^2 u \bar{v}}.$$

Now we note that if $\mu \in \mathbb{C}$, then $\bar{\mu} \neq \mu$. In our setting we have that $\mu \in \mathbb{R}$, allowing us to write:

$$\Phi(u, v)_\Omega = \overline{\int_\Omega \nabla u \cdot \nabla v - \mu^2 u \bar{v}} = \overline{\Phi(v, u)_\Omega}, \quad (1.16)$$

and hence we have that the Helmholtz operator is self-adjoint for real wave number μ .

1.6 Integral operators and potentials

Our numerical study of the Steklov-Helmholtz eigenvalue problem relies on reformulating it as an eigenvalue problem in terms of boundary integral operators and the fundamental solution G_μ . We seek solutions in terms of a boundary integral called the *Single layer potential*. This integral plays a central role in our method and we summarize the required theory in brief from Chapter 3 in [McL00].

Consider the usual space of “test” functions,

$$C_c^\infty(\Omega) = \{\phi, \phi \in C_K^\infty(\Omega), \text{ for some } K \subset\subset \Omega\},$$

i.e. the function space of infinitely differentiable functions with compact support in $\Omega \subset \mathbb{R}^d$ ($C_{\text{comp}}^\infty, C_0^\infty$ are a couple of the other notations for this space in the literature). For a multi-index $\alpha = (\alpha_1, \alpha_2, \dots, \alpha_d) \in \mathbb{N}_0^d$, we write for $\phi \in C_c^\infty(\Omega)$, $D^\alpha \phi = \partial_{x_1}^{\alpha_1} \partial_{x_2}^{\alpha_2} \cdots \partial_{x_d}^{\alpha_d} \phi$. We also consider the usual space $L^p(\Omega)$, which is the space of functions with a finite norm $\|\cdot\|_{L^p(\Omega)}$, where

$$\|u\|_{L^p(\Omega)} = \begin{cases} (\int_\Omega |u|^p dx)^{1/p}, & 1 \leq p < \infty \\ \text{ess sup}_{x \in \Omega} |u(x)|, & p = \infty. \end{cases}$$

We have that $C_c^\infty(\Omega)$ is dense in $L^p(\Omega)$, $p < \infty$ (see Corollary 3.5 in [McL00]). We denote the pairing of u, v denoted by $(u, v)_\Omega := \int_\Omega \bar{u}v \, dx$ whenever the integrand is in $L^1(\Omega)$.

Definition 1.6.1 (Locally summable/integrable function, page 64 [McL00]). *Suppose $\Omega \subset \mathbb{R}^d$ is open and let $f : \Omega \rightarrow \mathbb{C}$ be Lebesgue measurable. If the Lebesgue integral is finite for all compact subsets $\Omega_c \subset \Omega$, i.e. $\int_{\Omega_c} |f| \, dx < \infty$, $\forall \Omega_c \subset\subset \Omega$, then we say that f is locally summable on Ω and write $f \in L^1_{loc}(\Omega)$.*

Definition 1.6.2 (Convergence in $C_c^\infty(\Omega)$, page 65 [McL00]). *Let $(\phi_j)_{j \in \mathbb{N}}$ be a sequence in $C_c^\infty(\Omega)$. We say that $\phi_j \rightarrow 0$ in $C_c^\infty(\Omega)$ if and only if for all multi-indices α there exists some $K \subset\subset \Omega$, with $\text{supp } \phi_j \subset K \ \forall j$, $\partial^\alpha \phi_j \rightarrow 0$ uniformly in K .*

With this notion of convergence, we call $C_c^\infty(\Omega)$ the space of test functions and write $\mathcal{D}(\Omega)$ instead. Convergence to an element $\phi \in \mathcal{D}(\Omega)$ can be thought of as convergence of $\phi_j - \phi \rightarrow 0$.

Definition 1.6.3 (Sequential continuity, page 65 [McL00]). *Consider some linear functional $f : \mathcal{D} \rightarrow \mathbb{C}$. f is sequentially continuous if and only if for every sequence $\phi_j \in \mathcal{D}(\Omega)$, $\phi_j \rightarrow 0$ in $\mathcal{D}(\Omega)$ implies $f(\phi_j) \rightarrow 0$.*

Definition 1.6.4 (Schwartz distribution, page 65 [McL00]). *A Schwartz distribution on Ω is a linear functional $f : \mathcal{D} \rightarrow \mathbb{C}$ which is sequentially continuous.*

Note that the set of all distributions is larger and contains the set of Schwartz distributions. We denote by $\mathcal{D}^*(\Omega)$ the set of all distributions on Ω , the space of all linear and continuous functionals on \mathcal{D} .

Definition 1.6.5 (Dual space, page 20 [McL00]). *The dual space $X^* = \mathcal{L}(X, \mathbb{C})$ of a normed space X the space of all bounded linear functionals $f : X \rightarrow \mathbb{C}$. We write the pairing of $f \in X^*$ with an element of $u \in X$ as $\langle f, u \rangle = f(u)$ and mean it to be the value of f at u . By the Cauchy-Schwarz inequality we are led to the definition of the norm of the dual space, $\|f\|_{X^*} = \sup_{0 \neq u \in X} \frac{|\langle f, u \rangle|}{\|u\|_X}$.*

We note that the dual space X^* is always complete (Banach).

Example 1.6.1 (Pairing Schwartz distributions, page 66 [McL00]). *Let $u \in L^1_{loc}(\Omega)$ and $\phi \in \mathcal{D}(\Omega)$. Consider the linear functional $\tilde{f}u : \mathcal{D}(\Omega) \rightarrow \mathbb{C}$ defined as $(\tilde{f}u)(\phi) = (u, \phi)_\Omega$. If we consider sequences $\phi_j \rightarrow 0$, then clearly $(u, \phi_j)_\Omega \rightarrow 0$. Hence $\tilde{f}u$ is a Schwartz distribution. Further, we note that \tilde{f} itself can be thought of as a map from $L^1_{loc}(\Omega) \rightarrow \mathcal{D}^*(\Omega)$ and from Theorem 3.7 in [McL00], we have that it is one-one.*

All this is to say that $L^1_{loc}(\Omega)$ is a subspace of $\mathcal{D}^*(\Omega)$ and set of elements in $\mathcal{D}^*(\Omega)$ outside locally summable functions are called generalized functions / distributions (see page 65 in [McL00]).

Definition 1.6.6 (Weak derivative, page 67 [McL00]). *Let $u, g \in L^p(\Omega)$ and let α be a multi-index. Then, g is called the α th weak derivative of u ; $D^\alpha u = g$ in the sense of distributions, i.e.*

$$\int_\Omega u D^\alpha \phi \, dx = (-1)^{|\alpha|} \int_\Omega g \phi \, dx, \quad \forall \phi \in \mathcal{D}(\Omega).$$

Note that we require u, g above to be locally summable. Relating to the example above, we have $D^\alpha u = \tilde{f}g$.

Definition 1.6.7 (Sobolev spaces, page 73 [McL00]). *Let $k \in \mathbb{N}_0$ and $p \geq 1$. The space of functions in $L^p(\Omega)$ having weak order derivatives $D^\alpha f$ in $L^p(\Omega)$ for each multi-index α with $|\alpha| \leq k$ is called the Sobolev space denoted by $W^{k,p}(\Omega)$, i.e.*

$$W^{k,p}(\Omega) = \{f \in L^p(\Omega) : D^\alpha f \in L^p(\Omega) \text{ in the weak sense, } \forall |\alpha| \leq k\}.$$

Equipped with the norm

$$\|f\|_{W^{k,p}(\Omega)}^p = \begin{cases} \sum_{|\alpha| \leq k} \int_{\Omega} |D^\alpha f|^p \, dx & p < \infty \\ \left(\sum_{|\alpha| \leq k} \text{ess sup}_{\Omega} |D^\alpha f| \right)^p & p = \infty, \end{cases}$$

$W^{k,p}(\Omega)$ is a Banach space. Further for $p = 2$, $H^k := W^{k,2}$ is a Hilbert space, with the natural inner product.

Here $D^\alpha f$ is in the weak sense as in [Definition 1.6.6](#). For $k \in \mathbb{N}_0$ we can recursively define $W^{k,p}(\Omega)$ as given by Definition 2.1.3 in [\[LMP22\]](#).

In this thesis, the spaces $H^s(\Omega)$ and $H^s(M)$, where $s \in \mathbb{R}$ are of particular importance since the eigenfunctions of the Steklov-Helmholtz and Transmission eigenvalue problems live in them for specific values of s . So we need to extend the definition of H^k in two ways, to allow $k = s \in \mathbb{R}$ and to define these spaces on the boundary M . We continue our collection of the required definitions and ideas from Chapter 3 of [\[McL00\]](#). First, we try to understand how we can let $k \in \mathbb{R}$. For this we need two main tools, the Fourier transform and the Sobolev space on all of \mathbb{R}^d .

Definition 1.6.8 (Restricting distributions, page 66 [\[McL00\]](#)). *Let $\Omega_1 \subset \Omega$ be an open subset, and $\tilde{\phi} \in \mathcal{D}(\Omega)$ be the zero extension of $\phi \in \mathcal{D}(\Omega_1)$. The restriction of $u \in \mathcal{D}^*(\Omega)$ to $\mathcal{D}^*(\Omega_1)$ denoted by $u|_{\Omega_1}$ is defined as*

$$(u|_{\Omega_1}, \phi)_{\Omega_1} = (u, \tilde{\phi})_{\Omega}, \quad \text{for } \phi \in \mathcal{D}(\Omega_1).$$

Definition 1.6.9 (Fourier transform, page 70 [\[McL00\]](#)). *Let $u \in L^1(\mathbb{R}^d)$ and $\hat{u} := \mathcal{F}u$ denote the Fourier transform of u defined as*

$$\hat{u}(\xi) = \int_{\mathbb{R}^d} \exp(-2\pi i x \cdot \xi) u(x) \, dx, \quad \xi \in \mathbb{R}^d.$$

The adjoint of \mathcal{F} denoted by $u := \mathcal{F}^*\hat{u}$ is defined by,

$$u(x) = \int_{\mathbb{R}^d} \exp(2\pi i x \cdot \xi) \hat{u}(\xi) \, d\xi, \quad x \in \mathbb{R}^d.$$

Corollary 3.11 in [\[McL00\]](#) tells us that if $u, \hat{u} \in L_1(\mathbb{R}^d) \cap C(\mathbb{R}^d)$, then $\mathcal{F}^*\mathcal{F}u = u = \mathcal{F}\mathcal{F}^*u$.

Definition 1.6.10 (Schwartz space of rapidly decreasing functions, page 72 [\[McL00\]](#)). *Consider the space of $C^\infty(\mathbb{R}^d)$ functions, $\mathfrak{S}(\mathbb{R}^d) = \{\phi \in C^\infty(\mathbb{R}^d), \sup_{x \in \mathbb{R}^d} |x^\beta \partial^\alpha \phi(x)| < \infty, \forall \text{ multi-indices } \alpha, \beta\}$. Sequential convergence $\phi_j \rightarrow 0$ here means, $x^\beta \partial^\alpha \phi(x) \rightarrow 0$ uniformly for x and for all multi-indices α, β .*

Importantly, the Fourier transform defines a sequentially continuous linear operator $\mathcal{F} : \mathfrak{S}(\mathbb{R}^d) \rightarrow \mathfrak{S}(\mathbb{R}^d)$ and by Corollary 3.11 in [\[McL00\]](#) the inverse operator $\mathcal{F}^* : \mathfrak{S}(\mathbb{R}^d) \rightarrow \mathfrak{S}(\mathbb{R}^d)$ is continuous as well. Further, the dual of this space denoted by \mathfrak{S}^* is called the space of Temperate distributions.

Let $u, \phi \in \mathfrak{S}(\mathbb{R}^d)$. Then

$$(\mathcal{F}u, \phi) = \int_{\mathbb{R}^d} \int_{\mathbb{R}^d} \overline{u(x)} e^{-2\pi i x \cdot \xi} dx \phi(\xi) d\xi \stackrel{\text{Fubini}}{=} \int_{\mathbb{R}^d} \overline{u(x)} \int_{\mathbb{R}^d} \phi(\xi) e^{2\pi i x \cdot \xi} d\xi dx = (u, \mathcal{F}^*\phi),$$

and similarly, $(\mathcal{F}^*u, \phi) = (u, \mathcal{F}\phi)$. These lead to the extensions, $\mathcal{F} : \mathfrak{S}^*(\mathbb{R}^d) \rightarrow \mathfrak{S}^*(\mathbb{R}^d)$ and $\mathcal{F}^* : \mathfrak{S}^*(\mathbb{R}^d) \rightarrow \mathfrak{S}^*(\mathbb{R}^d)$.

We can extend the Fourier transform to $L^2(\mathbb{R}^d)$ (see Corollary 3.5 and Theorem 3.12 in [McL00]). So if we are able to find some operator using the Fourier transform that behaves like a differentiation operator, we can define weak derivatives of any fractional order. We also know that multiplication in the Fourier space corresponds to differentiation in the original space. So we consider the Bessel potential.

Definition 1.6.11 (Bessel potential of order $s \in \mathbb{R}$, page 75 [McL00]). *The continuous linear operator $\mathcal{J}^s : \mathfrak{S}(\mathbb{R}^d) \rightarrow \mathfrak{S}(\mathbb{R}^d)$ defined by*

$$\mathcal{J}^s(u(x)) = \int_{\mathbb{R}^d} (1 + |\xi|^2)^{s/2} \hat{u}(\xi) e^{2\pi i x \cdot \xi} d\xi = \mathcal{F}^*[(1 + |\xi|^2)^{s/2} \hat{u}(\xi)], \quad x \in \mathbb{R}^d$$

is called the Bessel potential of order s .

Definition 1.6.12 (Sobolev spaces $H^s(\mathbb{R}^d)$, page 76 [McL00]). *Let $s \in \mathbb{R}$ and define,*

$$H^s(\mathbb{R}^d) = \{u \in \mathfrak{S}^*(\mathbb{R}^d), \mathcal{J}^s(u) \in L^2(\mathbb{R}^d)\},$$

with the inner product and induced norm

$$(u, v)_{H^s(\mathbb{R}^d)} = (\mathcal{J}^s(u), \mathcal{J}^s(v)), \quad \|u\|_{H^s(\mathbb{R}^d)}^2 = \|\mathcal{J}^s(u)\|_{L^2(\mathbb{R}^d)}^2 = \int_{\mathbb{R}^d} (1 + |\xi|^2)^s |\hat{u}(\xi)|^2 d\xi.$$

We also have that $H^{-s}(\mathbb{R}^d) = [H^s(\mathbb{R}^d)]^*$ (see p. 76 [McL00]).

Definition 1.6.13 (Sobolev spaces $H^s(F)$, page 76 [McL00]). *Let $F \subset \mathbb{R}^d$ be closed and define*

$$H_F^s = \{u \in H^s(\mathbb{R}^d), \text{ supp } u \subseteq F\}.$$

Since F is closed, it is a Hilbert space with the restriction of the inner product on $H^s(\mathbb{R}^d)$.

Definition 1.6.14 (Sobolev spaces $H^s(\Omega)$, page 77 [McL00]). *Let $\Omega \subset \mathbb{R}^d$ be open and define,*

$$H^s(\Omega) = \{u \in \mathcal{D}^*(\Omega), \text{ } u = U|_{\Omega} \text{ for some } U \in H^s(\mathbb{R}^d)\}.$$

We define the inner product here using a specific orthogonal projection $P : H^s(\mathbb{R}^d) \rightarrow H_{\mathbb{R}^d \setminus \Omega}^s$ with $PU|_{\Omega} = 0$ and $(I - P)U|_{\Omega} = U|_{\Omega}$, $\forall U \in H^s(\mathbb{R}^d)$. For $U, V \in H^s(\mathbb{R}^d)$, if $u = U|_{\Omega}$ and $v = V|_{\Omega}$ we

have an inner product and induced norm,

$$(u, v)_{H^s(\Omega)} = ((I - P)U, (I - P)V)_{H^s(\mathbb{R}^d)}, \|u\|_{H^s(\Omega)} = \min_{U|_\Omega = u, U \in H^s(\mathbb{R}^d)} \|U\|_{H^s(\mathbb{R}^d)}.$$

Remark 1.6.1 (Another definition of Sobolev spaces). *For an equivalent definition using the Slobodeckii semi-norm see the first definition of Sobolev spaces in Chapter 3 of [McL00].*

Now we need to define Sobolev spaces on the boundary. We motivate this by noting that we can view boundaries of domains in \mathbb{R}^d as living in \mathbb{R}^{d-1} . This is the basis of defining Sobolev spaces on boundaries. Recall that M is the boundary of the open set Ω and that we can view $M = \partial\Omega = \overline{\Omega} \cap (\mathbb{R}^d \setminus \Omega)$. We have loosely used the term Lipschitz domain up till now. What we mean is that M can be written as the graph of some Lipschitz function locally. While it is possible that there are multiple such functions for different parts of M , the best case scenario would be if there was just one function $\zeta : \mathbb{R}^{d-1} \rightarrow \mathbb{R}$. We can write $\Omega = \Omega_\zeta = \{x = (x_1, \dots, x_d) \in \mathbb{R}^d, x_d < \zeta(x') \forall x' \in \mathbb{R}^{d-1}\}$ and $M = \{x = (x_1, \dots, x_{d-1}) \in \mathbb{R}^{d-1}, x_d = \zeta(x') \forall x' \in \mathbb{R}^{d-1}\}$. In a more general case the domain would be defined by a union of m many sets $\Omega = \cup_{i=1}^m \Omega_{\zeta_i}$. In the following definitions we assume that $\Omega = \Omega_\zeta$.

Definition 1.6.15 (Hölder space $C^{k,\beta}(D)$, page 90 [McL00]). *Let $k \in \mathbb{N}_0$ and $0 < \beta \leq 1$ and $D \subseteq \mathbb{R}^d$. The Hölder Spaces $C^{k,\beta}(D)$ consists of functions $\zeta \in C^k(D)$ such that the k th order partial derivatives are Hölder continuous with exponent β , i.e.*

$$|\partial^\alpha \zeta(x) - \partial^\alpha \zeta(y)| \leq M|x - y|^\beta \text{ for all } x, y \in D, |\alpha| = k, \text{ and some } M > 0.$$

Note that functions in $C^{0,1}(D)$ are Lipschitz functions. In our setting $D = \mathbb{R}^{d-1}$.

Definition 1.6.16 (Lipschitz domain, Definition 3.28 [McL00]). *Ω is a Lipschitz domain if M is compact and there are finite families $\{W_j\}$ and $\{\Omega_j\}$ such that*

- (i) *Each W_j is open and $M \subseteq \cup_j W_j$, i.e. $\{W_j\}$ is a finite open cover of M .*
- (ii) *Each Ω_j can be transformed into a Lipschitz hypograph by rotation plus translation (rigid motion).*
- (iii) *$W_j \cap \Omega = W_j \cap \Omega_j$ for each j .*

We recall from the discussion above that $\Omega = \Omega_\zeta$.

Definition 1.6.17 (Lipschitz hypograph, page 90 [McL00]). *If ζ is a Lipschitz function, then Ω is a Lipschitz hypograph.*

While the Lipschitz condition is the minimum requirement of regularity we require, it may be necessary to impose smoother conditions. Ω is a C^k hypograph if ζ is $C^k(D)$ with bounded partial

derivatives $\partial^\alpha \zeta$ for all $|\alpha| \leq k$. Further if the k th order partial derivatives of ζ are Hölder continuous with exponent β , then Ω is $C^{k,\beta}$ domain. Now we define some other Sobolev spaces and show relations to dual spaces.

Definition 1.6.18 (Some more Sobolev spaces). *Let $s \in \mathbb{R}$ and consider the Sobolev spaces,*

(i) $\tilde{H}^s(\Omega) = \text{closure of } \mathcal{D}(\Omega) \text{ in } H^s(\mathbb{R}^d)$,

(ii) $H_0^s(\Omega) = \text{closure of } \mathcal{D}(\Omega) \text{ in } H^s(\Omega)$.

These are Hilbert spaces on restricting the inner products of $H^s(\mathbb{R}^d)$ and $H^s(\Omega)$. Further, they are equal for $s \neq \frac{2n-1}{2}$, $n \in \mathbb{N}$ (Theorem 3.33 [McL00]). We also have for all $s \in \mathbb{R}$ (Theorem 3.30 [McL00]),

(i) $H^s(\Omega)^* = \tilde{H}^s(\Omega)$,

(ii) $\tilde{H}^s(\Omega)^* = H^{-s}(\Omega)$.

Definition 1.6.19 (Sobolev spaces on the boundary, page 98 [McL00]). *If Ω is a $C^{r+1,1}$ with $r \geq 0$, then for $u \in L_2(M)$ define $u_\zeta(x') = u(x', \zeta(x'))$ for $x \in \mathbb{R}$. We have*

$$H^s(M) = \{u \in L_2(M), u_\zeta \in H^s(\mathbb{R})\} \text{ for } |s| \leq r + 1,$$

with the inner product $(u, v)_{H^s(M)} = (u_\zeta, v_\zeta)_{H^s(\mathbb{R})}$. We can also define $H^{-s}(M)$ as the dual of $H^s(M)$ with

$$\|u\|_{H^{-s}(M)} = \sup_{0 \neq v \in H^s(M)} \frac{|(u, v)_M|}{\|v\|_{H^s(M)}}.$$

For both the Steklov-Helmholtz and Transmission eigenvalue problems, the idea is to reformulate them into boundary integral equations and construct solutions in terms of the *Single layer potential*. We view the potential as a right inverse of the trace operator (see Section 1.7.1). Finally, for the next two definitions we refer to Theorems 6.12, 6.13, 7.1, 7.2 in [McL00] and recall the fundamental solution $G_\mu(x, y)$ of the Helmholtz equation given in Equation 1.15.

Definition 1.6.20 (Single-layer potential). *Let Ω be $C^{r+1,1}$, $r \geq 0$. The map $\mathcal{S}_\mu : H^{s-1/2}(M) \rightarrow H^{s+1}(\Omega)$,*

$$[\mathcal{S}_\mu \phi](x) = 2 \int_M G_\mu(x, y) \phi(y) \, ds_y, \quad x \in \mathbb{R}^d \setminus M, \quad (1.17)$$

where $r \in \mathbb{N}_0$ and $|s| \leq r + 1$ is called the single-layer potential.

The single layer potential maps boundary data to the solution in the domain and is continuous.

We now consider the continuous restrictions of the single layer and its normal derivative with respect to x to the boundary M .

Definition 1.6.21 (Extensions of Single-layer potential to the boundary). *Under assumptions of the single layer, the maps $S_\mu : H^{s-1/2}(M) \rightarrow H^{s+1/2}(M)$ and $K'_\mu : H^{s-1/2}(M) \rightarrow H^{s-1/2}(M)$ are continuous for $y \neq x \in M$ with,*

$$([\mathcal{S}_\mu \phi](x))_{|_M} = 2 \int_M G_\mu(x, y) \phi(y) \, ds_y, \quad (1.18)$$

and

$$(\partial_{\nu_x} [\mathcal{S}_\mu \phi](x))_{|_M} = 2 \int_M \partial_{\nu_x} G_\mu(x, y) \phi(y) \, ds_y + \phi(x). \quad (1.19)$$

We denote these by $[S_\mu \phi](x) := ([\mathcal{S}_\mu \phi](x))_{|_M}$ and $[K'_\mu \phi](x) := 2 \int_M \partial_{\nu_x} G_\mu(x, y) \phi(y) \, ds_y$. Note that when extending the normal derivative of the single layer to the boundary, we pick up a jump (see Theorem 2.13 in [CK83]).

1.7 Dirichlet to Neumann maps

The following discussion is based on Section 7.4 of [LMP22]. Let $s \in \mathbb{R}$ and $\mu \neq 0$. To find the eigenvalues σ of the Steklov-Helmholtz eigenvalue problem (1.2) with $\rho \equiv 1$,

$$\begin{cases} -\Delta U = \mu^2 U & \text{in } \Omega, \\ \partial_\nu U = \sigma U & \text{on } M, \end{cases} \quad (1.20)$$

we first consider the Dirichlet problem,

$$\begin{cases} -\Delta U = \mu^2 U & \text{in } \Omega, \\ U = u & \text{on } M, \end{cases} \quad (1.21)$$

for some $u \in H^{s+1/2}(M)$ and the associated homogeneous problem, i.e. when the boundary data $u \equiv 0$,

$$\begin{cases} -\Delta U = \mu^2 U & \text{in } \Omega, \\ U = 0 & \text{on } M. \end{cases} \quad (1.22)$$

By Theorem 4.10 (i) in [McL00], if (1.22) has only the trivial solution, then (1.21) has a unique solution $U \in H^{s+1}(\Omega)$. From Theorem 6.2.5 in [Eva10] we know that (1.22) has a nontrivial solution if and only if $\mu^2 \in \text{Spec}(1.22)$ and so as long as $\mu^2 \notin \text{Spec}(1.22)$, (1.21) has a unique solution in $H^{s+1}(\Omega)$. Similarly for a unique solution to the Neumann version of (1.21), we need μ^2 to not be a Neumann eigenvalue of the Laplacian. These ideas lead to probably the most restrictive assumption in this thesis that μ^2 is not a Dirichlet or Neumann eigenvalue of the Laplacian. In a crude sense, we see that if σ in (1.20) were to be 0 and we sought μ^2 , then it would reduce to the Neumann-

Laplace problem. Similarly in a crude sense, to reduce to the Dirichlet-Laplace problem, we would need $1/\sigma \rightarrow 0$.

Under our assumptions, [Equation 1.21](#) has a unique solution, which we define to be $U := \mathcal{E}_\mu u \in H^{s+1}(\Omega)$. This solution is called the μ -Helmholtz extension of u , where

$$\begin{aligned}\mathcal{H}_\mu(\Omega) &= \{U \in H^{s+1}(\Omega), -\Delta U = \mu^2 U\} =: S_1 \\ &= \{\mathcal{E}_\mu u, u \in H^{s+1/2}(M)\} =: S_2.\end{aligned}$$

We set $s = 0$ for now. The first form of this set gives us the solution directly as a function in $H^1(\Omega)$ whose trace is u , and the second characterises the solution as an extension of the boundary data in $H^{1/2}(M)$. By the trace Theorems 3.37 and 3.38 in [\[McL00\]](#), if Ω is a Lipschitz domain, the trace is bounded and its right continuous inverse is continuous. So we have a bounded trace $T : H^1(\Omega) \rightarrow H^{1/2}(M)$ with a continuous right inverse, $\mathcal{E}_\mu : H^{1/2}(M) \rightarrow H^1(\Omega)$. We now show equivalence of the two sets S_1 and S_2 .

- S_1 contains elements in $H^1(\Omega)$ such that they solve [Equation 1.21](#). We will see that such solutions are extensions of boundary data in $H^{1/2}(M)$. Let $U_1, U_2 \in S_1$ and $\alpha \in \mathbb{C}$, and consider

$$-\Delta(U_1 + \alpha U_2) = -\Delta U_1 - \alpha \Delta U_2 = \mu^2 U_1 + \alpha \mu^2 U_2 = \mu^2(U_1 + \alpha U_2)$$

So S_1 is a subspace of $H^1(\Omega)$. Now suppose that $U \in S_1$. Then ΔU is well defined. If the boundary M is Lipschitz then by the trace Theorem there exists a bounded linear operator $T : H^1(\Omega) \rightarrow H^{1/2}(M)$ such that $TU = U|_M$. So if $\mu^2 \notin \text{Spec}(1.22)$, there exists an extension of $f := U|_M$, $\mathcal{E}_\mu f = U$, since the solution depends continuously on the boundary data.

- Now suppose we take a $W := \mathcal{E}_\mu u \in H^1(\Omega)$ such that it solves the Helmholtz equation. Again by the trace Theorem, $TW \in H^{1/2}(M)$ and so [Equation 1.21](#) is solvable with boundary data $u = TW$.

Definition 1.7.1 (Dirichlet to Neumann map for the Helmholtz equation, Def. 7.4.1 [\[LMP22\]](#)).
Let $\mu^2 \notin \text{Spec}(1.22)$. The linear operator

$$\mathcal{D}_\mu : H^{s+1/2}(M) \rightarrow H^{s-1/2}(M), \quad \mathcal{D}_\mu : u \rightarrow T\partial_\nu(\mathcal{E}_\mu u) \tag{1.23}$$

which maps Dirichlet datum u to the Neumann datum trace of the normal derivative of its μ^2 -Helmholtz extension is called the Dirichlet to Neumann (DtN) map for the Helmholtz equation.

To clarify the meaning of $\partial_\nu \mathcal{E}_\mu u$ in the definition above let $U := \mathcal{E}_\mu u, V \in H^1(\Omega)$ and note that U solves the Helmholtz equation. By Green's formula,

$$\begin{aligned}\int_{\Omega} \nabla \cdot (V \nabla U) &= \int_{\Omega} \nabla V \cdot \nabla U + V \Delta U = \int_{\Omega} \nabla V \cdot \nabla U - \mu^2 V U \\ &= \int_M v \partial_\nu U, \quad \forall V \in H^1(\Omega), \quad v := TV \in H^{1/2}(M).\end{aligned}$$

With respect to problems (1.20) and (1.21), we see that the DtN map takes the boundary data of (1.21) to the trace of the normal derivative of (1.20). We summarize the important maps that we work with.

1.7.1 Maps

Let Ω be $C^{r+1,1}$, $r \geq 0$. Then by Theorems 3.37 and 4.21 in [McL00],

- The extension operator takes $\mathcal{E}_\mu : H^{s+1/2}(M) \rightarrow H^{s+1}(\Omega)$, $0 \leq s \leq r+1$.
- The Dirichlet to Neumann map takes $\mathcal{D}_\mu : H^{s+1/2}(M) \rightarrow H^{s-1/2}(M)$, $|s| \leq r+1$.
- The trace operator takes $T : H^{s+1}(\Omega) \rightarrow H^{s+1/2}(M)$, $-1/2 < s \leq r+1$.

In view of Definitions 1.6.20 and 1.6.21, we have $\mathcal{S}_\mu = \mathcal{E}_\mu S_\mu$ and $S_\mu = T \mathcal{S}_\mu$.

1.7.2 Assumptions for unique solutions

Let $s = 0$ and consider $\mu^2 \in \text{Spec}(1.22)$. In this case there is no guarantee of the existence of a solution to (1.21), let alone uniqueness. Consider the space of Neumann boundary traces of eigenfunctions of (1.22),

$$\mathcal{K}_\mu := \{T \partial_\nu U, \quad U \in \mathcal{H}_\mu(\Omega) \cap H_0^1(\Omega)\} = \{T \partial_\nu U, \quad -\Delta U = \mu^2 U, \quad TU = u = 0\}.$$

Note that by linearity of normal derivative and the trace map, \mathcal{K}_μ is a vector space. By Theorem 6.5.1 [Eva10] the multiplicity of each eigenvalue μ^2 is finite. So \mathcal{K}_μ is finite dimensional. Now we examine required conditions for existence of solutions of (1.21). Suppose U^D is a Dirichlet eigenfunction of (1.22) with respect to eigenvalue μ^2 and U solves (1.21). Then,

$$\mu^2(U, U^D)_{L^2(\Omega)} = (-\Delta U, U^D)_{L^2(\Omega)} = (U, -\Delta U^D)_{L^2(\Omega)} + (T(\partial_\nu U), TU^D)_{L^2(M)} + (TU, T(\partial_\nu U^D))_{L^2(M)}.$$

From the homogeneous Dirichlet-Helmholtz problem (1.22) we have $-\Delta U^D = \mu^2 U$ on Ω and $U^D|_M = 0$. So,

$$\begin{aligned}\mu^2(U, U^D)_{L^2(\Omega)} &= \mu^2(U, U^D)_{L^2(\Omega)} + (TU, T(\partial_\nu U^D))_{L^2(M)} \iff (U, \partial_\nu U^D)_{L^2(M)} = 0 \\ &\iff TU \perp T(\partial_\nu U^D).\end{aligned}$$

So (1.21) is solvable if and only if $TU = u$ is orthogonal to \mathcal{K}_μ in $L^2(M)$. We now look at uniqueness. Suppose U solves (1.21) and U^D is an eigenfunction of (1.22). Then consider on Ω for $\alpha \in \mathbb{R}$, $-\Delta(U + \alpha U^D) = -\Delta U - \alpha \Delta U^D = \mu^2(U + \alpha U^D)$ and in M , $TU + \alpha TU^D = TU = u$. Hence solutions of (1.21) are unique modulo addition of Dirichlet eigenfunctions. For a more thorough examination and extension of [Definition 1.7.1](#) we refer to Section 7.4.1 in [LMP22]. So as long as $\mu^2 \notin \text{Spec}(1.22)$, the domain of \mathcal{D}_μ is $\text{Dom}(\mathcal{D}_\mu) = H^{s+1/2}(M)$.

1.7.3 Connection to the Steklov-Helmholtz problem

Now we set $s = 0$ and explore the connection between the Dirichlet to Neumann map and the Steklov-Helmholtz problem. Let $U, V \in H^1(\Omega)$ be sufficiently smooth and solve the Helmholtz equation. By the divergence product rule and the Helmholtz equation,

$$\nabla \cdot (V \nabla U) = \nabla V \cdot \nabla U + V \Delta U = \nabla V \cdot \nabla U - \mu^2 VU.$$

Consider again problem (1.2) with boundary weight ρ . Now we integrate, use the Divergence Theorem and the Steklov-Helmholtz boundary condition,

$$\sigma_\rho(TV, \rho TU)_{L^2(M)} = (\nabla V, \nabla U)_{L^2(\Omega)} - \mu^2(V, U)_{L^2(\Omega)} \quad (1.24)$$

where we denote by σ_ρ the eigenvalue of the boundary weighted problem (1.2). On setting $V = U$ we get the Steklov-Helmholtz eigenvalues in terms of their eigenfunctions,

$$\sigma_\rho = \frac{\|\nabla U\|_{L^2(\Omega)}^2 - \mu^2 \|U\|_{L^2(\Omega)}^2}{\|\sqrt{\rho} TU\|_{L^2(M)}^2}. \quad (1.25)$$

Going back to the LHS of [Equation 1.24](#) with $V = U$ and $\rho \equiv 1$, we have that

$$\sigma \|TU\|_{L^2(M)}^2 = (TU, T(\partial_\nu U))_{L^2(M)} = (TU, \mathcal{D}_\mu u)_{L^2(M)},$$

and thus see that the Steklov-Helmholtz problem and the Dirichlet to Neumann map \mathcal{D}_μ are isospectral. Further, (1.24) is also the quadratic form of the self-adjoint DtN operator \mathcal{D}_μ . Also, the basis of eigenfunctions are orthogonal in $L^2(M)$ (see Section 3.1.1 and p. 270 in [LMP22]). Now we state the variational principle for the Steklov-Helmholtz problem.

Theorem 1.7.1 (Variational principle for the Dirichlet to Neumann map, Thm. 7.4.2 [LMP22]). *Let Ω be a bounded open set in \mathbb{R}^d , with a Lipschitz boundary $M = \partial\Omega$, let $\mu \in \mathbb{R}$ be fixed, and let*

σ_k be the eigenvalues of the Dirichlet to Neumann map for the Helmholtz equation in Ω . Then,

$$\begin{aligned}\sigma_k &= \min_{\tilde{\mathcal{L}}_\mu \subset \text{Dom}(\mathcal{D}_\mu), u \in \tilde{\mathcal{L}}_\mu \setminus \{0\}, \dim \tilde{\mathcal{L}}_\mu = k} \frac{\|\nabla \mathcal{E}_\mu u\|_{L^2(\Omega)}^2 - \mu^2 \|\mathcal{E}_\mu u\|_{L^2(\Omega)}^2}{\|u\|_{L^2(M)}^2} \\ &= \min_{\mathcal{L}_\mu \subset \mathcal{H}_\mu(\Omega), u \in \mathcal{L}_\mu \setminus \{0\}, \dim \mathcal{L}_\mu = k} \frac{\|\nabla U\|_{L^2(\Omega)}^2 - \mu^2 \|U\|_{L^2(\Omega)}^2}{\|U|_M\|_{L^2(M)}^2}.\end{aligned}\tag{1.26}$$

With the trace Theorem and from Remark 3.1.4 in [LMP22], for eigenfunctions $\mathcal{E}_\mu u_1, \dots, \mathcal{E}_\mu u_{k-1}$ we can choose $\mathcal{L}_{k-1} = \text{span}\{\mathcal{E}_\mu u_1, \dots, \mathcal{E}_\mu u_{k-1}\}$ to reformulate

$$\sigma_k = \min_{u \in \text{Dom}(\mathcal{D}_\mu) \setminus \{0\}, u \perp \mathcal{L}_{k-1}} \frac{\|\nabla \mathcal{E}_\mu u\|_{L^2(\Omega)}^2 - \mu^2 \|\mathcal{E}_\mu u\|_{L^2(\Omega)}^2}{\|\mathcal{E}_\mu u\|_{L^2(M)}^2}.$$

To summarize, for the Steklov-Helmholtz eigenvalue problem we set $s = 0$ and have the mapping property for,

- the Dirichlet to Neumann map, $\mathcal{D}_\mu : H^{1/2}(M) \rightarrow H^{-1/2}(M)$.
- the layer potentials, $\mathcal{S}_\mu : H^{-1/2}(M) \rightarrow H^1(\Omega)$, $S_\mu : H^{-1/2}(M) \rightarrow H^{1/2}(M)$ and $K'_\mu : H^{-1/2}(M) \rightarrow H^{-1/2}(M)$ are continuous.

1.7.4 Connection to the Transmission problem

We examine the transmission eigenvalue problem (1.3) with the assumption that both μ^2 and $n_{RI}\mu^2$ are not Dirichlet-Laplace eigenvalues. We set $s = \pm 1$ and summarize the main ideas of Section 2 in [CK17]. We look for solutions $V, W \in H^0(\Omega) = L^2(\Omega)$ such that $V - W \in H^2(\Omega)$. From lemma 2.1 in [CK17] and Theorem 7.17 in [McL00], we have that S_k is Fredholm with zero index (Theorem 2.27 in [McL00]). This leads to the existence and boundedness of the inverse map $S_\mu^{-1} : H^{-1/2}(M) \rightarrow H^{-3/2}(M)$. For refractive index n_{RI} we get, a formulation of $\mathcal{D}_{\mu, n_{RI}} : H^{-1/2}(M) \rightarrow H^{-3/2}(M)$ as $\mathcal{D}_{\mu, n_{RI}} = (I + K'_{\mu, n_{RI}})S_\mu^{-1}$. Recall the single layer potential and its traces from [Definition 1.6.20](#) and [Definition 1.6.21](#) for $\Omega \in C^{r+1,1}$,

$$\mathcal{S}_\mu : H^{s-1/2}(M) \rightarrow H^{s+1}(\Omega), [\mathcal{S}_\mu \phi](x) = 2 \int_M G_\mu(x, y) \phi(y) \, ds_y, \quad x \in \mathbb{R}^d \setminus M,$$

and

$$K'_\mu : H^{s-1/2}(M) \rightarrow H^{s-1/2}(M), [K'_\mu \phi](x) = 2 \int_M \partial_{\nu_x} G_\mu(x, y) \phi(y) \, ds_y, \quad y \neq x \in M,$$

where $|s| \leq r+1$. In the context of transmission eigenvalues we hence need to consider the difference operator (see equation 2.10 in [CK17]),

$$N(\mu) = \mathcal{D}_\mu - \mathcal{D}_{\mu, n_{RI}}. \quad (1.27)$$

In Section 2 of [CK17] the authors show that $N(\mu)$ is bounded (lemma 2.4), coercive (Theorem 2.5) and compact (Theorem 2.6). Theorems 2.5 and 2.6 of [CK17] then imply Theorem 2.7 which states that $N(\mu)$ is a Fredholm operator with index 0 and is analytic. We summarize the mapping properties and boundedness of $N(\mu)$ and cite [CK17] for the remaining details. The idea is to use the fact that $N(\mu)$ is the normal derivative on the boundary M of the operator that takes $\phi \rightarrow (\mathcal{S}_\mu S_\mu^{-1} - \mathcal{S}_{\mu, n_{RI}} S_{\mu, n_{RI}}^{-1})\phi$. Then since this operator is bounded, it follows that its normal derivative trace $N(\mu)$ is (lemma 2.1 [CK17]) bounded. Let $u = (\mathcal{S}_\mu S_\mu^{-1} - \mathcal{S}_{\mu, n_{RI}} S_{\mu, n_{RI}}^{-1})\phi$, $\phi \in H^{-1/2}(M)$ on M . Rewriting

$$u = \mathcal{S}_\mu(S_\mu^{-1} - S_{\mu, n_{RI}}^{-1})\phi - (\mathcal{S}_{\mu, n_{RI}} - \mathcal{S}_\mu)S_{\mu, n_{RI}}^{-1}\phi, \quad (1.28)$$

along with Theorem 3.2 in [CH13] and the trace Theorem we have that the operators,

$$\mathcal{S}_{\mu, n_{RI}} - \mathcal{S}_\mu : H^{-3/2}(M) \rightarrow H^2(\Omega), \quad (1.29)$$

$$S_\mu - S_{\mu, n_{RI}} : H^{-3/2}(M) \rightarrow H^{3/2}(M), \quad (1.30)$$

are bounded.

From Corollary 2.3 [CK17] we have that $S_{\mu, n}^{-1} : H^{-1/2}(M) \rightarrow H^{-3/2}(M)$, ($s = -1$) and $S_\mu^{-1} : H^{3/2}(M) \rightarrow H^{1/2}(M)$, ($s = 1$) are bounded. Now we rewrite the difference operator of the inverses as

$$S_{\mu, n_{RI}}^{-1} - S_\mu^{-1} = S_\mu^{-1}(S_\mu - S_{\mu, n_{RI}})S_{\mu, n_{RI}}^{-1}. \quad (1.31)$$

Then using the mapping properties above and equation (1.30) that $S_\mu^{-1} - S_{\mu, n_{RI}}^{-1} : H^{-1/2}(M) \rightarrow H^{1/2}(M)$ is bounded.

Now going back to (1.28) we consider both terms individually. In the first term, we have from (1.31) that $(S_\mu^{-1} - S_{\mu, n_{RI}}^{-1})\phi \in H^{1/2}(M)$ and from (1.17) ($s = 1$) that $\mathcal{S}_\mu(S_\mu^{-1} - S_{\mu, n_{RI}}^{-1})\phi \in H^2(\Omega)$. Next, for the second term we have that $S_{\mu, n_{RI}}^{-1}\phi \in H^{-3/2}(M)$. From (1.29) we have that $(\mathcal{S}_{\mu, n_{RI}} - \mathcal{S}_\mu)S_{\mu, n_{RI}}^{-1}\phi \in H^2(\Omega)$. Hence the operator (1.28) maps from $H^{-1/2}(M) \rightarrow H^2(\Omega)$ and together with the boundedness of the operators above, we have that the operator (1.28) is bounded as well. We began with the observation that $N(\mu)$ is the normal trace of this operator and from (1.17) and (1.19) for $s = 1$ we have that $N(\mu) : H^{-1/2}(M) \rightarrow H^{1/2}(M)$ is bounded.

Chapter 2

Reformulating and discretizing the Steklov-Helmholtz eigenvalue problem

In this Chapter we consider closed and bounded domains Ω in \mathbb{R}^2 whose boundaries M have a smooth 2π -periodic parameterization. We recall the Steklov-Helmholtz eigenvalue problem (1.2) to find eigenpairs u, σ such that

$$\begin{cases} -\Delta u - \mu^2 u = 0 & \text{in } \Omega, \\ \frac{\partial u}{\partial \nu} = \sigma \rho u & \text{on } M. \end{cases} \quad (1.2)$$

We assume that the eigenfunctions of the Steklov-Helmholtz eigenvalue problem (1.2) are given by the single layer potential (1.17). The Chapter is arranged as follows. In Section 2.1 we reformulate the eigenvalue problem (1.2) into an integral equation involving integral operators. We then observe that the kernels of these integral operators have logarithmic singularities. For proper numerical treatment of these kernels, we split the kernels in Section 2.2 using the technique given by Martensen and Kussmaul (see [Mar63], [Kus69]). In Section 2.3 we discuss the use of quadratures and discretization of the layer potentials. Finally, we describe the obtained generalized eigenvalue problem in Section 2.4. We perform numerical experiments in Chapter 3.

2.1 2d Integral reformulation

We recall the Helmholtz equation for positive wave number μ , $-\Delta U - \mu^2 U = 0$ and let $\Omega \in \mathbb{R}^2$ be a bounded region with C^2 boundary $M := \partial\Omega$. We also recall the single layer potential S_μ and the adjoint of the double layer potential K'_μ from Definition 1.6.21. For $x \in M$ we have,

$$[S_\mu \phi](x) := 2 \int_M G_\mu(x, y) \phi(y) \, ds_y \quad (2.1)$$

and

$$[K'_\mu \phi](x) := 2 \int_M \partial_{n_x} G_\mu(x, y) \phi(y) \, ds_y \quad (2.2)$$

We use the single layer and adjoint of the double layer potentials defined in [Equation 2.1](#) and [Equation 2.2](#) to reformulate the Steklov-Helmholtz eigenvalue problem as a boundary integral equation. From Theorems 3.16 and 3.28 of [\[CK83\]](#), we know that the single layer potential with continuous density $\phi \in H^{1/2}(M)$

$$\frac{1}{2}[\mathcal{S}\phi](x) = \int_M G_\mu(x, y)\phi(y) \, ds_y, \quad x \in \mathbb{R}^2 \setminus M, \quad (2.3)$$

solves the interior Neumann and Dirichlet problems with boundary data $g(x)$ and $f(x)$ respectively, if the density satisfies the corresponding integral equation for all $x \in M$,

$$\int_M \partial_{\nu_x} G_\mu(x, y)\phi(y) \, ds_y + \frac{\phi(x)}{2} = g(x) \quad (2.4)$$

and

$$\int_M G_\mu(x, y)\phi(y) \, ds_y = f(x). \quad (2.5)$$

Considering this we use the ansatz for the solution of the Steklov-Helmholtz eigenvalue problem: $u(x) = \int_M G_\mu(x, y)\phi(y) \, ds_y$. Then the Steklov boundary condition gives,

$$\begin{aligned} \int_M \partial_{\nu_x} G_\mu(x, y)\phi(y) \, ds_y + \frac{\phi(x)}{2} &= \sigma\rho \int_M G_\mu(x, y)\phi(y) \, ds_y, \text{ i.e.} \\ K'_\mu \phi + \phi &= \sigma\rho S_\mu \phi. \end{aligned} \quad (2.6)$$

The eigenvalue problem is now to find the surface density ϕ and generalized eigenvalues σ . We need to confirm that this formulation is indeed equivalent to [\(1.2\)](#).

- Suppose that u solves [\(1.2\)](#). Then by the reformulation we just did, the density ϕ and σ must solve [\(2.6\)](#).
- Now suppose that we know that ϕ and σ solve [\(2.6\)](#). Then by Theorems 3.16 and 3.28 of [\[CK83\]](#), we have that [\(2.1\)](#) is a solution of the Helmholtz equation inside Ω . Further, by [\(2.6\)](#) and the double and single layers we get back the Steklov boundary condition.

2.1.1 Boundary parametrization

In what follows, we set $\rho \equiv 1$ and discuss other cases for ρ in [Remark 2.4.2](#). We assume that the boundary M is analytic and has a 2π periodic parametrization given by $z : t \rightarrow \mathbb{R}^2$ where $t \in [0, 2\pi]$, $z(t) = (z_1(t), z_2(t))$. We require $|z'(t)| > 0$. We set $x = z(t)$ and $y = z(\tau)$. Now we write the relevant terms under this parametrization. The density is $\phi(x) = \phi(z(t)) =: \psi(t)$ and the differential is $ds_y = |z'(\tau)| \, d\tau$.

The fundamental solution of the Helmholtz equation becomes $G_\mu(x, y) = \frac{i}{4}H_0^1(\mu r(t, \tau))$, where $r(t, \tau)^2 = (z_1(t) - z_1(\tau))^2 + (z_2(t) - z_2(\tau))^2$. Next, we look at the normal derivative of G_μ with

respect to x . Noting that $(H_0^1)' = -H_1^1$,

$$\begin{aligned}\partial_{\nu_x} \frac{i}{4} H_0^1(\mu |x-y|) &= \frac{i}{4} \nabla_{z(t)} H_0^1(\mu r(t, \tau)) \cdot \nu_{z(t)} = \frac{i}{4} \nabla_{z(t)} H_0^1(\mu r(t, \tau)) \cdot \frac{(z'_2(t), -z'_1(t))}{|z'(t)|}, \\ &= \frac{i\mu}{4|z'(t)|r(t, \tau)} H_1^1(\mu r(t, \tau)) [z'_2(t)(z_1(\tau) - z_1(t)) - z'_1(t)(z_2(\tau) - z_2(t))], \\ \partial_{\nu_x} \frac{i}{4} H_0^1(\mu |x-y|) &= \frac{i\mu}{4|z'(t)|r(t, \tau)} H_1^1(\mu r(t, \tau)) X(t, \tau),\end{aligned}$$

where we denote $X(t, \tau) := [z'_2(t)(z_1(\tau) - z_1(t)) - z'_1(t)(z_2(\tau) - z_2(t))]$.

Note that by assumption we have $|z'(t)| > 0$. For this parametrization with $\tau \neq t \in [0, 2\pi)$ the integral [Equation 2.6](#) becomes

$$\frac{i\mu}{2|z'(t)|} \int_0^{2\pi} \frac{H_1^1(\mu r(t, \tau))}{r(t, \tau)} X(t, \tau) |z'(\tau)| \psi(\tau) d\tau + \psi(t) = \sigma \frac{i}{2} \int_0^{2\pi} H_0^1(\mu r(t, \tau)) |z'(\tau)| \psi(\tau) d\tau. \quad (2.7)$$

Denoting

$$L(t, \tau) := \frac{i\mu}{2|z'(t)|} \frac{H_1^1(\mu r(t, \tau))}{r(t, \tau)} X(t, \tau) |z'(\tau)| \text{ and } M(t, \tau) := \frac{i}{2} H_0^1(\mu r(t, \tau)) |z'(\tau)|,$$

we rewrite [Equation 2.7](#) as

$$\int_0^{2\pi} L(t, \tau) \psi(\tau) d\tau + \psi(t) = \sigma \int_0^{2\pi} M(t, \tau) \psi(\tau) d\tau. \quad (2.8)$$

The goal is to solve eigenvalue problem [\(2.8\)](#) to find the eigendensities $\psi \in H^{1/2}(M)$ and eigenvalues $\sigma \in \mathbb{R}$.

2.2 Splitting to treat singularities

We wish to approximate the integrals in [\(2.8\)](#) with suitable quadratures. We note that $L(t, \tau)$ and $M(t, \tau)$ are kernels of the integrals on the left and right hand sides of [\(2.8\)](#) respectively. We observe that when $t = \tau$, these kernels L and M have logarithmic singularities due to the Neumann function of order 0 (i.e. $Y_0(0)$, see [Equation 1.14](#)). We split both the kernels where we subtract and add a term given in [\[Mar63\]](#) and [\[Kus69\]](#). By doing this, each kernel is split into two kernels such that we preserve 2π -periodicity of each kernel and we are able to use suitable quadratures.

We begin by examining M in more detail using the series expansions of the Bessel function (1.13) of order 0 and that of the Neumann function (1.14) of order 0,

$$M(t, \tau) = \frac{i|z'(\tau)|}{2} \left[J_0(\mu r(t, \tau)) + i \left(\frac{2}{\pi} \left\{ \ln \frac{\mu r(t, \tau)}{2} + C \right\} J_0(\mu r(t, \tau)) - \frac{2}{\pi} \sum_{p=0}^{\infty} \frac{(-1)^p}{(p!)^2} \left(\frac{\mu r(t, \tau)}{2} \right)^{2p} \xi(p) \right) \right].$$

Now we add and subtract the term given by [Mar63] and [Kus69],

$$\begin{aligned} M(t, \tau) &= \frac{i|z'(\tau)|}{2} \left[\left(1 + \frac{2i}{\pi} \left\{ \ln \frac{\mu r(t, \tau)}{2} + C \right\} \right) J_0(\mu r(t, \tau)) - \frac{2i}{\pi} \sum_{p=0}^{\infty} \frac{(-1)^p}{(p!)^2} \left(\frac{\mu r(t, \tau)}{2} \right)^{2p} \xi(p) \right] \\ &\quad \mp \frac{|z'(\tau)| J_0(\mu r(t, \tau))}{2\pi} \ln \left(4 \sin^2 \frac{t-\tau}{2} \right), \\ &= -\frac{|z'(\tau)| J_0(\mu r(t, \tau))}{2\pi} \ln \left(4 \sin^2 \frac{t-\tau}{2} \right) + \frac{|z'(\tau)|}{\pi} \sum_{p=0}^{\infty} \frac{(-1)^p}{(p!)^2} \left(\frac{\mu r(t, \tau)}{2} \right)^{2p} \xi(p) \\ &\quad + \frac{|z'(\tau)|}{2} \left[i - \frac{2C}{\pi} - \frac{1}{\pi} \ln \left(\frac{(\mu r(t, \tau))^2}{16 \sin^2 \frac{t-\tau}{2}} \right) \right] J_0(\mu r(t, \tau)). \end{aligned}$$

We now denote

$$M_1(t, \tau) := -\frac{|z'(\tau)| J_0(\mu r(t, \tau))}{2\pi}$$

and

$$\begin{aligned} M_2(t, \tau) &:= \frac{|z'(\tau)|}{2} \left[i - \frac{2C}{\pi} - \frac{1}{\pi} \ln \left(\frac{(\mu r(t, \tau))^2}{16 \sin^2 \frac{t-\tau}{2}} \right) \right] J_0(\mu r(t, \tau)) + \\ &\quad \frac{|z'(\tau)|}{\pi} \sum_{p=0}^{\infty} \frac{(-1)^p}{(p!)^2} \left(\frac{\mu r(t, \tau)}{2} \right)^{2p} \xi(p), \end{aligned}$$

giving

$$M(t, \tau) := M_1(t, \tau) \ln \left(4 \sin^2 \frac{t-\tau}{2} \right) + M_2(t, \tau). \quad (2.9)$$

We now examine for $M_2(t, \tau)$ the limit $t \rightarrow \tau$, only for the argument of the logarithm since the other terms in $M_2(t, \tau)$ are clearly well behaved in this limit.

$$\begin{aligned} \lim_{\tau \rightarrow t} \frac{r(t, \tau)^2}{\sin^2 \frac{t-\tau}{2}} &= 2 \lim_{\tau \rightarrow t} \frac{z'_1(\tau)[z_1(t) - z_2(\tau)] + z'_2(\tau)[z_2(t) - z_1(\tau)]}{\sin \frac{t-\tau}{2} \cos \frac{t-\tau}{2}} \\ &= 4 \lim_{\tau \rightarrow t} \frac{z'_1(\tau)[z_1(t) - z_2(\tau)] + z'_2(\tau)[z_2(t) - z_1(\tau)]}{\sin(t-\tau)} = 4[z'_1(\tau)^2 + z'_2(\tau)^2], \end{aligned}$$

where we use L'Hôpital's rule twice. Noting that $J_0(0) = 1$, $r(t,t) = 0$ and $\xi(0) = 0$ we get,

$$\lim_{t \rightarrow \tau} M_2(t, \tau) = \frac{|z'(t)|}{2} \left[i - \frac{2C}{\pi} - \frac{1}{\pi} \ln \left(\frac{\mu^2}{4} [z'_1(t)^2 + z'_2(t)^2] \right) \right]. \quad (2.10)$$

We therefore define the value of $M_2(t, t) = \lim_{t \rightarrow \tau} M_2(t, \tau)$ as obtained above in [Equation 2.10](#) to ensure continuity in the limit.

Now let us examine $L(t, \tau)$. For convenience let

$$A(t, \tau) := \frac{\mu}{2\pi} \frac{|z'(\tau)|}{|z'(\tau)|} \frac{X(t, \tau)}{r(t, \tau)} \text{ and}$$

$$B(t, \tau) := \frac{\mu r(t, \tau)}{2} \sum_{p=0}^{\infty} \frac{(-1)^p}{p!(1+p)!} \left(\frac{\mu r(t, \tau)}{2} \right)^{2p} \{\xi(1+p) + \xi(p)\}.$$

With this,

$$L(t, \tau) = i\pi A(t, \tau) \left[J_1(\mu r(t, \tau)) + i \left(\frac{2}{\pi} \left\{ \ln \frac{\mu r(t, \tau)}{2} + C \right\} J_1(\mu r(t, \tau)) - \frac{1}{\pi} \frac{2}{\mu r(t, \tau)} - \frac{1}{\pi} B(t, \tau) \right) \right]$$

$$= \pi A(t, \tau) \left[\left(i - \frac{2}{\pi} \left\{ \ln \frac{\mu r(t, \tau)}{2} + C \right\} \right) J_1(\mu r(t, \tau)) + \frac{1}{\pi} \frac{2}{\mu r(t, \tau)} + \frac{1}{\pi} B(t, \tau) \right].$$

We again subtract and add a similar term as we did for M and simplify,

$$L(t, \tau) = \pi A(t, \tau) \left[\left(i - \frac{2}{\pi} \left\{ \ln \frac{\mu r(t, \tau)}{2} + C \right\} \right) J_1(\mu r(t, \tau)) + \frac{1}{\pi} \left(\frac{2}{\mu r(t, \tau)} + B(t, \tau) \right) \right]$$

$$\mp A(t, \tau) J_1(\mu r(t, \tau)) \ln \left(4 \sin^2 \frac{t-\tau}{2} \right),$$

$$L(t, \tau) = -A(t, \tau) J_1(\mu r(t, \tau)) \ln \left(4 \sin^2 \frac{t-\tau}{2} \right) + A(t, \tau) \left(\pi i - \ln \left(\frac{\mu^2 r(t, \tau)^2}{16 \sin^2 \frac{t-\tau}{2}} \right) + 2C \right) J_1(\mu r(t, \tau))$$

$$+ A(t, \tau) \left(\frac{2}{\mu r(t, \tau)} + B(t, \tau) \right).$$

We now denote

$$L_1(t, \tau) := -A(t, \tau) J_1(\mu r(t, \tau)),$$

and

$$L_2(t, \tau) := A(t, \tau) J_1(\mu r(t, \tau)) \left(\pi i - \ln \left(\frac{\mu^2 r(t, \tau)^2}{16 \sin^2 \frac{t-\tau}{2}} \right) + 2C \right) + A(t, \tau) \left(\frac{2}{\mu r(t, \tau)} + B(t, \tau) \right).$$

We can write,

$$L(t, \tau) := L_1(t, \tau) \ln \left(4 \sin^2 \frac{t-\tau}{2} \right) + L_2(t, \tau). \quad (2.11)$$

In both L_1 and L_2 note the presence of the term $A(t, \tau)J_1(\mu r(t, \tau))$. Further in L_2 , the term $A(t, \tau)$ appears with $1/r(t, \tau)$ and $B(t, \tau)$. We must check that the limits of these terms as $\tau \rightarrow t$ exist. We first compute the limit of $A(t, \tau)J_1(\mu r(t, \tau))$ as $\tau \rightarrow t$,

$$\begin{aligned} A(t, \tau)J_1(\mu r(t, \tau)) &= \frac{\mu}{2\pi} \frac{|z'(\tau)|}{|z'(t)|} \frac{X(t, \tau)}{r(t, \tau)} \sum_{p \geq 0} \frac{(-1)^p}{p!(p+1)!} \left(\frac{\mu r(t, \tau)}{2} \right)^{1+2p} \\ &= \frac{\mu^2}{4\pi} \frac{|z'(\tau)|}{|z'(t)|} X(t, \tau) \sum_{p \geq 0} \frac{(-1)^p}{p!(p+1)!} \left(\frac{\mu r(t, \tau)}{2} \right)^{2p}, \end{aligned}$$

and then

$$\lim_{t \rightarrow \tau} A(t, \tau)J_1(\mu r(t, \tau)) = \lim_{t \rightarrow \tau} -L_1(t, \tau) = 0, \quad (2.12)$$

since $X(t, t) = 0$ and the series is convergent. Therefore we define

$$L_1(t, t) = \lim_{t \rightarrow \tau} L_1(t, \tau) = 0,$$

as obtained in [Equation 2.12](#) to ensure continuity in the limit. We observe that $L_2(t, \tau)$ is structured like $M_2(t, \tau)$ and so in a very similar way as we did for $M_2(t, \tau)$, we can show that both the first term of $L_2(t, \tau)$ and $A(t, \tau)B(t, \tau)$ go to 0 as $t \rightarrow \tau$.

The only term left to check in $L_2(t, \tau)$ is,

$$A(t, \tau) \frac{2}{\mu r(t, \tau)} = \frac{1}{\pi} \frac{|z'(\tau)|}{|z'(t)|} \frac{X(t, \tau)}{r^2(t, \tau)}.$$

Note that we only need to check the limit for the ratio of $X(t, \tau)/r^2(t, \tau)$,

$$\lim_{\tau \rightarrow t} \frac{X(t, \tau)}{r^2(t, \tau)} = \lim_{\tau \rightarrow t} \frac{[z'_2(t)(z_1(\tau) - z_1(t)) - z'_1(t)(z_2(\tau) - z_2(t))]}{(z_1(\tau) - z_1(t))^2 + (z_2(\tau) - z_2(t))^2}.$$

We use L'Hôpital's rule a few times again,

$$\begin{aligned} \lim_{\tau \rightarrow t} \frac{X(t, \tau)}{r^2(t, \tau)} &= \lim_{\tau \rightarrow t} \frac{1}{2} \frac{[z'_2(t)z'_1(\tau) - z'_1(t)z'_2(\tau)]}{(z_1(\tau) - z_1(t))z'_1(\tau) + (z_2(\tau) - z_2(t))z'_2(\tau)} \\ 2 \lim_{\tau \rightarrow t} \frac{X(t, \tau)}{r^2(t, \tau)} &= \lim_{\tau \rightarrow t} \frac{z'_2(t)z''_1(\tau) - z'_1(t)z''_2(\tau)}{z'_1(\tau)^2 + (z_1(\tau) - z_1(t))z''_1(\tau) + z'_2(\tau)^2 + (z_2(\tau) - z_2(t))z''_2(\tau)} \\ 2 \lim_{\tau \rightarrow t} \frac{X(t, \tau)}{r^2(t, \tau)} &= \frac{z'_2(t)z''_1(t) - z'_1(t)z''_2(t)}{|z'_1(t)|^2}. \end{aligned}$$

Recalling that $A(t, \tau) = \frac{\mu}{2\pi} \frac{|z'(\tau)|}{|z'(t)|} \frac{X(t, \tau)}{r(t, \tau)}$ we get,

$$\lim_{\tau \rightarrow t} \frac{2A(t, \tau)}{\mu r(t, \tau)} = \frac{z'_2(t)z''_1(t) - z'_1(t)z''_2(t)}{2\pi |z'(t)|^2}. \quad (2.13)$$

To ensure continuity in the limit, we therefore define $L(t, t) = \lim_{\tau \rightarrow t} \frac{2A(t, \tau)}{\mu r(t, \tau)}$ as obtained in (2.13). The kernels L_1, L_2, M_1 and M_2 turn out to be analytic ([CK13] p. 77). Note also that M, L are 2π periodic. So the integral Equation 2.8 to find $\psi \in H^{1/2}(M)$ and $\sigma \in \mathbb{R}$ becomes: to find ψ, σ so that,

$$\begin{aligned} \int_0^{2\pi} \left[L_1(t, \tau) \ln \left(4 \sin^2 \frac{t - \tau}{2} \right) + L_2(t, \tau) \right] \psi(\tau) \, d\tau + \psi(t) \\ = \sigma \int_0^{2\pi} \left[M_1(t, \tau) \ln \left(4 \sin^2 \frac{t - \tau}{2} \right) + M_2(t, \tau) \right] \psi(\tau) \, d\tau. \end{aligned} \quad (2.14)$$

2.3 Specialized quadratures

After splitting the kernels L, M , in Equation 2.14 we have integrals with logarithmic kernels of the form,

$$\int_0^{2\pi} f(t, \tau) \ln \left(4 \sin^2 \frac{t - \tau}{2} \right) + g(t, \tau) \, d\tau,$$

where f and g are products of M_1 (L_1) and M_2 (L_2) as defined in equations (2.9), (2.11). Now we partition $[0, 2\pi]$ with $2N + 1$ equidistant points as

$$\tau_j = \frac{\pi j}{N}, \quad j : 0 \rightarrow 2N.$$

Since we only consider closed curves, note that $t = 0$ and $t = 2\pi$ correspond to the same point in \mathbb{R}^2 . We use separate quadratures for the two integrands.

The form of the first integrand obtained due to the Kussmaul-Martensen splitting allows us to use their quadrature ([Mar63], [Kus69]) as described in Section 3.5 of [CK13]. This quadrature is also referred to as the Kress quadrature (see equations 11.11, 11.12 and 12.16 in [Kre99]).

$$\begin{aligned} \int_0^{2\pi} f(t, \tau) \ln \left(4 \sin^2 \frac{t - \tau}{2} \right) \, d\tau &\approx \sum_{j=0}^{2N-1} R^N(t, \tau_j) f(t, \tau_j), \text{ where} \\ R^N(t, \tau_j) &:= -\frac{2\pi}{N} \sum_{m=1}^{N-1} \frac{\cos m(t - \tau_j)}{m} - \pi \frac{\cos N(t - \tau_j)}{N^2}, \quad j : 0 \rightarrow 2N - 1. \end{aligned}$$

Note that we only use the first $2N$ points, i.e. all points excluding 2π .

For the second (non-singular) integrand we can use the Trapezoidal rule,

$$\int_0^{2\pi} g(t, \tau) \, d\tau \approx \frac{\pi}{N} \left(\frac{g(t, 0) + g(t, 2\pi)}{2} + \sum_{j=1}^{2N-1} g(t, \tau_j) \right) = \frac{\pi}{N} \sum_{j=0}^{2N-1} g(t, \tau_j).$$

For the trapezoidal rule we know that as long as the function is analytic and periodic, the error decreases at least exponentially. Further, we can exactly recover the integral for trigonometric polynomials of degree $\leq N$ using the trapezoidal rule (see equation 12.1 in [Kre99]). Now we replace $f(t, \tau)$ and $g(t, \tau)$ by their trigonometric interpolation polynomials with associated Lagrange basis of degree N , denoted by $f^{tp}(t, \tau)$. We use the interpolating property that $f^{tp}(t, \tau_j) = f(t, \tau_j)$, $j : 0 \rightarrow 2N - 1$. From equations 11.11 and 11.12 in [Kre99] we know that for an equidistant partition of $[0, 2\pi]$ with an even number of grid points and function evaluations at the grid points there is a unique trigonometric polynomial (with Lagrange basis),

$$f^{tp}(t, \tau) = \frac{a_0}{2} + \sum_{l=1}^{N-1} \{a_l \cos l\tau + b_l \sin l\tau\} + \frac{a_N}{2} \cos N\tau, \text{ where}$$

$$a_l = \int_0^{2\pi} f(t, \tau) \cos(l\tau) d\tau \text{ and } b_l = \int_0^{2\pi} f(t, \tau) \sin(l\tau) d\tau.$$

Now using the Trapezoidal rule we evaluate the coefficients a_l, b_l and for instance,

$$\int_0^{2\pi} f(t, \tau) d\tau \approx \frac{\pi}{N} \sum_{s=0}^{2N-1} f(t, \tau_s) \implies a_0 = \frac{1}{N} \sum_{s=0}^{2N-1} f(t, \tau_s).$$

Similarly, we evaluate the rest of the coefficients a_l , $l : 1 \rightarrow N$ and b_l , $l : 1 \rightarrow N - 1$ using the Trapezoidal rule. Both these quadratures are known to have exponential convergence in case the integrands are periodic and analytic. Since we first convert our integrands to their trigonometric polynomials, we expect to observe spectral convergence (see Section 3.5 in [CK83] and Section 12.4 in [Kre99]). On simplifying (2.14) is replaced by the approximation,

$$\begin{aligned} & \sum_{j=0}^{2N-1} \left(R^N(t, \tau_j) L_1^{tp}(t, \tau_j) + \frac{\pi}{N} L_2^{tp}(t, \tau_j) \right) \psi^{tp}(\tau_j) + \psi^{tp}(t) \\ &= \sigma \sum_{j=0}^{2N-1} \left(R^N(t, \tau_j) M_1^{tp}(t, \tau_j) + \frac{\pi}{N} M_2^{tp}(t, \tau_j) \right) \psi^{tp}(\tau_j) \end{aligned} \tag{2.15}$$

2.4 Generalized eigenvalue problem

Now we discretize t exactly as we did τ , $t_k = \frac{k\pi}{N}$, $k : 0 \rightarrow 2N - 1$ to get a discrete eigenvalue problem of size $(2N)^2$. For $k : 0 \rightarrow 2N - 1$ we have,

$$\begin{aligned} & \sum_{j=0}^{2N-1} \left(R^N(t_k, \tau_j) L_1^{tp}(t_k, \tau_j) + \frac{\pi}{N} L_2^{tp}(t_k, \tau_j) \right) \psi^{tp}(\tau_j) + \psi^{tp}(t_k) \\ &= \sigma \sum_{j=0}^{2N-1} \left(R^N(t_k, \tau_j) M_1^{tp}(t_k, \tau_j) + \frac{\pi}{N} M_2^{tp}(t_k, \tau_j) \right) \psi^{tp}(\tau_j). \end{aligned} \quad (2.16)$$

We denote this as,

$$(A + Id)\psi^{tp} = \sigma B\psi^{tp}, \quad (2.17)$$

where Id (Identity matrix), A , B and σ are $2N \times 2N$ matrices with complex entries and ψ^{tp} is a column vector of length $2N$. The k^{th} rows A_k and B_k of A and B respectively are,

$$\begin{aligned} A_k &= [\alpha_{k0}, \alpha_{k1}, \dots, \alpha_{k,2N-1}] \text{ with} \\ \alpha_{kj} &= R^N(t_k, \tau_j) L_1^{tp}(t_k, \tau_j) + \frac{\pi}{N} L_2^{tp}(t_k, \tau_j), \quad j : 0 \rightarrow 2N - 1, \end{aligned}$$

$$\begin{aligned} B_k &= [\beta_{k0}, \beta_{k1}, \dots, \beta_{kk}, \dots, \beta_{k,2N-1}] \text{ with} \\ \beta_{kj} &= R^N(t_k, \tau_j) M_1^{tp}(t_k, \tau_j) + \frac{\pi}{N} M_2^{tp}(t_k, \tau_j), \quad j : 0 \rightarrow 2N - 1 \end{aligned}$$

and

$$\sigma = \text{diag}(\sigma_0, \dots, \sigma_{2N-1}).$$

The vector ψ^{tp} (which is the evaluation of the trigonometric interpolation polynomial of the density ψ at the grid points) is what we solve for along with σ ,

$$\psi^{tp} = [\psi(0), \psi(t_1), \dots, \psi(t_{2N-1})].$$

Remark 2.4.1 (Discretized layer potentials). *The $2N \times 2N$ matrix A in Equation 2.17 corresponds to the discretized adjoint of the double layer potential. The $2N \times 2N$ matrix B in Equation 2.17 corresponds to the discretized single layer potential. Depending on the context, we may modify the notation to A_μ in case we want to emphasize the wave number, or $B_{n_{RI}}$ in case we want to emphasize the refractive index. We may also use a combination of the two.*

Remark 2.4.2 (Boundary weighted Steklov-Helmholtz eigenvalue problem). *Suppose there is a positive and bounded weight function ρ on the boundary, i.e. on the boundary, $\partial_\nu U = \sigma \rho U$, where $0 < \rho \in L^\infty(M)$. We note that ρ is a function of t which maps to every point on M a positive*

number. For a boundary weighted Steklov-Helmholtz eigenvalue problem we can write,

$$(A + I)\psi^{2N} = \sigma B_\rho \psi^{2N}, \quad (2.18)$$

where the k^{th} row of B_ρ is $(B_\rho)_k = \rho(t_k)B_k$. In this thesis, we set $\rho \equiv 1$, unless specified otherwise.

Now to evaluate the trigonometric polynomials, we note that the coefficients $\{a_l\}_{l=0}^N$ and $\{b_l\}_{l=1}^{N-1}$ will change when we change t and include all values of τ . We recall the trigonometric interpolation polynomial and rewrite it in terms of dot products,

$$\begin{aligned} f^{tp}(t, \tau) &= \frac{a_0}{2} + \sum_{l=1}^{N-1} \{a_l \cos l\tau + b_l \sin l\tau\} + \frac{a_N}{2} \cos N\tau \\ &= a_f(t) \cdot \cos((0 : N)\tau) + b_f(t) \cdot \sin((1 : N-1)\tau), \end{aligned}$$

where $a_f(t) = (a_0/2, a_1, \dots, a_N/2)$ and $b_f(t) = (b_1, \dots, b_{N-1})$. At the node points, the trigonometric interpolation polynomials are exactly the function values, so we drop the tp superscript. Denoting the matrix of evaluations as f_m we have,

$$f_m = \begin{pmatrix} f(t_0, \tau_0) & f(t_0, \tau_1) & \cdots & f(t_0, \tau_{2N}) \\ f(t_1, \tau_0) & f(t_1, \tau_1) & \cdots & f(t_1, \tau_{2N}) \\ \vdots & \vdots & \ddots & \vdots \\ f(t_{2N}, \tau_0) & f(t_{2N}, \tau_1) & \cdots & f(t_{2N}, \tau_{2N}) \end{pmatrix}.$$

Now we create two matrices called A_{\cos} and A_{\sin} at grid values of t as,

$$A_{\cos} = \begin{pmatrix} \cos(0 \cdot t_0) & \cos(1 \cdot t_0) & \cdots & \cos(2Nt_0) \\ \cos(0 \cdot t_1) & \cos(1 \cdot t_1) & \cdots & \cos(2Nt_1) \\ \vdots & \vdots & \ddots & \vdots \\ \cos(0 \cdot t_{2N}) & \cos(1 \cdot t_{2N}) & \cdots & \cos(2Nt_{2N}) \end{pmatrix},$$

and

$$A_{\sin} = \begin{pmatrix} \sin(0 \cdot t_0) & \sin(1 \cdot t_0) & \cdots & \sin(2Nt_0) \\ \sin(0 \cdot t_1) & \sin(1 \cdot t_1) & \cdots & \sin(2Nt_1) \\ \vdots & \vdots & \ddots & \vdots \\ \sin(0 \cdot t_{2N}) & \sin(1 \cdot t_{2N}) & \cdots & \sin(2Nt_{2N}) \end{pmatrix}.$$

This allows us to construct all coefficients $(a_f(t), b_f(t))$ using matrix multiplications. First consider,

$${}_{2N+1}\tilde{a}_f(t)^{N+1} = \frac{1}{N} f_m[:, 1:(2N)] A_{\cos}[:, 1:(N+1)]$$

Note that we must divide the first and last column by 2 since in the trigonometric polynomials we have $a_0/2$ and $a_N/2$. The first row of $a_f(t)$ contains the coefficients a for $t = t_0$ and so on.

Similarly we get $b_f(t)$. Finally we get the evaluation matrix as

$${}_{2N+1}f_m^{tp^{2N+1}} = a_f(t) A_{\cos}[:, 1:(N+1)]^T + b_f(t) A_{\sin}[:, 2:N]^T.$$

From these matrices we can now construct the desired matrices A and B as in (2.17). The corresponding code is in Appendices B.2 and B.3. To solve the generalized eigenvalue problem (2.17) we use MATLAB's `eig` function which returns the eigendensities ψ with corresponding Steklov eigenvalues σ . We begin [Chapter 3](#) by testing whether the matrices of the discretized potentials, A and B work as intended on test cases.

Chapter 3

Numerical experiments for the Steklov-Helmholtz problem for smooth and bounded domains in \mathbb{R}^2

In Section 2.3 and Section 2.4 of Chapter 2, we have described a discretization strategy for the Steklov-Helmholtz problem. We first conduct tests to check its accuracy for known problems on the disk in Section 3.1. We demonstrate the use of our strategy to locate standard eigenvalues of the Laplacian in Section 3.2. We then explore the use of our method on domains of genus 1 in Section 3.3. In Section 3.4 we discuss convergence of our method and show some eigenpairs for various domains. In Section 3.5 we inspect various properties of the spectrum for domains of genus 0. We also experiment with various boundary weights in Section 3.6. Section 3.7 concludes this chapter with the discussion of a shape optimization problem and some experiments on the disk, deformed kite and ellipse.

3.1 Tests on a disk of radius $R > 0$

We perform three tests on the disk parametrized by $z(t) = R(\cos t, \sin t)$.

In the first test, we compute solutions of the interior Dirichlet and Neumann problems for the Helmholtz equation. As noted in Section 2.1 the single layer potential solves these problems for the Helmholtz equation with boundary functions $f(x)$ and $g(x)$. If we use a constant density $\psi \equiv c \in \mathbb{C}$, then along with rotational symmetry of the disk and $|z'(t)| = R$, we have that $\int_0^{2\pi} H_m^1(\mu r(t, \tau)) d\tau$, $m = 0, 1$ are constant for the disk. This implies constant boundary data for constant density. The goal is to check whether application of the corresponding discretized potential layers to these constant boundary data gives back c . Recall from Table 1.2 that $J_n(\mu r)e^{in\theta}$ solves the Helmholtz equation. For Bessel order $n = 0$ i.e. $J_0(\mu R)$, we get purely radial solutions. This is the corresponding solution we compute for the interior problems.

In the second test, we approximate the eigenvalues of the Dirichlet/Neumann/Robin-Laplace eigenvalue problems. We consider these eigenvalue problems as boundary value problems for the Helmholtz equation and therefore use the built discretized layer potentials to search for the respective eigenvalues.

Finally in the third test, we use the discretized potentials to compute the Steklov eigenvalues on the disk and compare them to the known true Steklov eigenvalues.

3.1.1 Interior Dirichlet and Neumann problems

For the Interior Dirichlet problem (IDP) as long as ψ is continuous, we have by Theorem 3.28 in [CK83],

$$\int_0^{2\pi} \frac{i}{4} H_0^1(\mu r(t, \tau)) \psi(\tau) |z'(\tau)| d\tau = f(z(t)) \iff B\psi = 2f,$$

where B is the matrix corresponding to the discretized single layer potential (see [Equation 2.17](#), [Remark 2.4.1](#)). Let us choose the boundary data $f(x) \equiv 1$. Now suppose that the constant density is $\psi \equiv c_D \in \mathbb{C}$ and $\frac{1}{2} + \int_0^{2\pi} \frac{i\mu}{4} H_1^1(\mu r(t, \tau)) \frac{X(t, \tau)}{r(t, \tau)} d\tau \equiv d_D \in \mathbb{C}$. Therefore we have $c_D = 1/d_D$. Then we apply the inverse of the matrix corresponding to the single layer B^{-1} to $2v_1$, where $v_1 = (1, \dots, 1)$ is a vector of ones of length $2N$. If the matrix B is working correctly, we expect $2B^{-1}v_1 \approx c_D v_1$.

Similarly, for the Interior Neumann problem (INP), we have by Theorem 3.16 in [CK83],

$$\frac{1}{2}\psi(z(t)) + \int_0^{2\pi} \frac{i\mu}{4|z'(t)|} H_1^1(\mu r(t, \tau)) \frac{X(t, \tau)}{r(t, \tau)} \psi(\tau) |z'(\tau)| d\tau = g(z(t)) \iff (I + A)\psi = 2g,$$

where A is the matrix corresponding to the discretized adjoint of the double layer potential (see [Equation 2.17](#), [Remark 2.4.1](#)). Here again we set $g \equiv 1$. Suppose that the constant density is $\psi \equiv c_N \in \mathbb{C}$ and $\int_0^{2\pi} \frac{iR}{4} H_0^1(\mu r(t, \tau)) d\tau \equiv d_N \in \mathbb{C}$. We now obtain $c_N = 1/d_N$. We apply $(I + A)^{-1}$ to $2v_1$ and expect to observe that $2(I + A)^{-1}v_1 \approx c_N$.

Using MATLAB's `integral` and `besselh` we compute the true densities using the relations $c_D = 1/d_D$ and $c_N = 1/d_N$. We denote the “true” solution by $(\psi_i^{comp})_{i=1}^{2N}$ and the approximate solution by $(\psi_i^N)_{i=1}^{2N}$. In [Table 3.1](#) and [Table 3.2](#) we show the first five entries of the true vector $(\psi_j^{comp})_{j=1}^5$ computed using MATLAB functions and the approximated vector $(\psi_j^N)_{j=1}^5$ using our approach for both the IDP and INP respectively. We report the values using the default tolerances of the `integral` function, we observe that our approach is gives higher digits of accuracy as compared to using MATLAB's functions. We also decrease both absolute and relative tolerances to $1e-15$ and yet again observe more constant digits through our approach. We expect ψ to be constant and in [Table 3.3](#) we show the differences between the first 5 values of the computed vectors.

ψ_j^{comp} IDP	ψ_j^N IDP
7.040346 02901207 - 7.0004 5190933563i	7.04034602931 813 - 7.00045196236 719i
7.040346 01016941 - 7.0004 4859362835i	7.04034602931 059 - 7.00045196236 159i
7.040346 07838167 - 7.0004 6059804515i	7.04034602931 584 - 7.00045196236 647i
7.040346 08567035 - 7.0004 6188097477i	7.04034602931 055 - 7.00045196236 260i
7.040346 18994246 - 7.0004 8023897127i	7.04034602931 458 - 7.00045196236 403i

Table 3.1: First 5 entries of the true and approximate densities, $\mu = 7$, $N = 729$, $R = 2\pi$. The columns correspond to the Interior Dirichlet Problem (IDP). The numbers in pink bold text are the digits for which the true densities ψ^{comp} computed using inbuilt MATLAB functions are constant. The numbers in blue bold text are the digits for which the densities ψ^N computed by our approach are constant.

ψ_j^{comp} INP	ψ_j^N INP
1.011430790 49955 - 1.005699 52557705i	1.011430790 50003 - 1.005699525658 39i
1.011430790 51798 - 1.005699 52882200i	1.011430790 50003 - 1.005699525658 38i
1.011430790 40697 - 1.005699 50928800i	1.011430790 49998 - 1.005699525658 34i
1.011430790 35299 - 1.005699 49978665i	1.011430790 50006 - 1.00569955658 41i
1.011430790 28834 - 1.005699 48841195i	1.011430790 49998 - 1.005699525658 34i

Table 3.2: First 5 entries of the true and approximate densities, $\mu = 7$, $N = 729$, $R = 2\pi$. The columns correspond to the Interior Neumann Problem (INP). The numbers in pink bold text are the digits for which the true densities ψ^{comp} computed using inbuilt MATLAB functions are constant. The numbers in blue bold text are the digits for which the densities ψ^N computed by our approach are constant.

$\psi_{j+1}^{comp} - \psi_j^{comp}$ IDP	$\psi_{j+1}^N - \psi_j^N$ IDP	$\psi_{j+1}^{comp} - \psi_j^{comp}$ INP	$\psi_{j+1}^N - \psi_j^N$ INP
-1.88427e-08 + 3.31571e-06i	-7.537082e-12 + 5.60263e-12i	1.84344e-11 - 3.24494e-09i	6.43929e-15 + 9.76996e-15i
6.82123e-08 - 1.20044e-05i	5.24381e-12 - 4.88409e-12i	-1.11010e-10 + 1.95340e-08i	-5.19584e-14 + 3.619327e-14i
7.28868e-09 - 1.28293e-06i	-5.28555e-12 + 3.87246e-12i	-5.39839e-11 + 9.50136e-09i	7.66054e-14 - 7.52731e-14i
1.04272e-07 - 1.83580e-05i	4.02878e-12 - 1.42819e-12i	-6.46438e-11 + 1.13747e-08i	-7.92670e-14 + 7.172041e-14i

Table 3.3: Differences between the first 5 entries of the true ψ^{comp} and approximate ψ^N densities, $\mu = 7$, $N = 729$, $R = 2\pi$. The first 2 columns correspond to the Interior Dirichlet Problem (IDP). The last 2 columns correspond to the Interior Neumann Problem (INP).

3.1.2 Dirichlet / Neumann / Robin eigenvalues of the Laplacian

One of the two most restrictive assumptions that we make in this thesis is that μ^2 is not a Dirichlet or Neumann eigenvalue of the Laplacian. Using the discretized single and adjoint of double layer potentials, we can locate the Dirichlet, Neumann and Robin eigenvalues of the Laplacian, which we recall are denoted by λ^D , λ^N and λ^R respectively (see [Table 1.1](#)). The idea is to search within a range of μ values for which S_μ or $K'_\mu + I$ or their linear combination (for Robin) have near singular kernels. Note that the corresponding μ^2 's are the respective Laplacian eigenvalues λ^i , $i = D, N, R$.

We refer now to the formulation of [Equation 2.6](#) and [Remark 2.4.1](#). Concretely, a Dirichlet eigenvalue μ^2 of the Laplacian (see [Table 1.1](#)) satisfies $S_\mu \phi = 0$. We search for values of μ such that the discretized operator $B_\mu := B$ has a near zero singular value. Similarly a Neumann-Laplace eigenvalue μ^2 satisfies $(K'_\mu + I)\phi = 0$. So we search for values of μ such that the discretized operator $A_\mu + Id := A + Id$ has a near zero singular value. Finally a Robin-Laplace eigenvalue μ^2 satisfies $S_\mu \phi - \sigma(K'_\mu + I)\phi = 0$. So we search for values of μ such that the discretized operator $C_\mu := -\sigma B + (A + Id)$ has a near zero singular value. Our search procedure is listed in [Algorithm 1](#) below.

Algorithm 1 Search for Laplace eigenvalues λ^D , λ^N and λ^R

Require: Curve details, σ , $[\mu_{\min}, \mu_{\max}]$ and number of points n_μ .

Create vector of n_μ equispaced wave numbers in $[\mu_{\min}, \mu_{\max}]$ and 3 vectors of length of n_μ , s_{\min}^i , $i = D, N, R$ to store minimum singular values for each problem.

for $j = 1, \dots, n_\mu$ **do**

$\mu = \mu_j$

Compute SVDs of B_μ , $A_\mu + Id$ and $C_\mu = -\sigma B_\mu + (A_\mu + Id)$.

Find smallest singular value of each and store in j th element of respective s_{\min}^i , $i = D, N, R$.

end for

We can solve the Laplace eigenvalue problems for the disk of radius R . From [Section 1.4.2](#), we observe that μ^2 is a Dirichlet-Laplace eigenvalue for the disk of radius R if $J_n(\mu R) = 0$. Similarly for the Neumann and Robin Laplace problems, μ^2 is an eigenvalue of the Neumann (respectively Robin) Laplacian if $J'_n(\mu R) = 0$ (respectively $-\sigma J_n(\mu R) + \mu J'_n(\mu R) = 0$). In [Figure 3.1](#) and [Figure 3.2](#) we test the use of the discretized layer potentials to search for wave numbers μ so that μ^2 's are standard eigenvalues of the Laplacian of disks (see [Algorithm 1](#)). In these figures we show the minimum singular values s_{\min}^i , $i = D, N, R$ of B_μ ($i = D$, top row, blue), $A_\mu + Id$ ($i = N$, middle row, red) and C_μ ($i = R$, bottom row, purple) as μ varies. The vertical black lines correspond with true eigenvalues which the local minimas of minimum singular values almost coincide with.

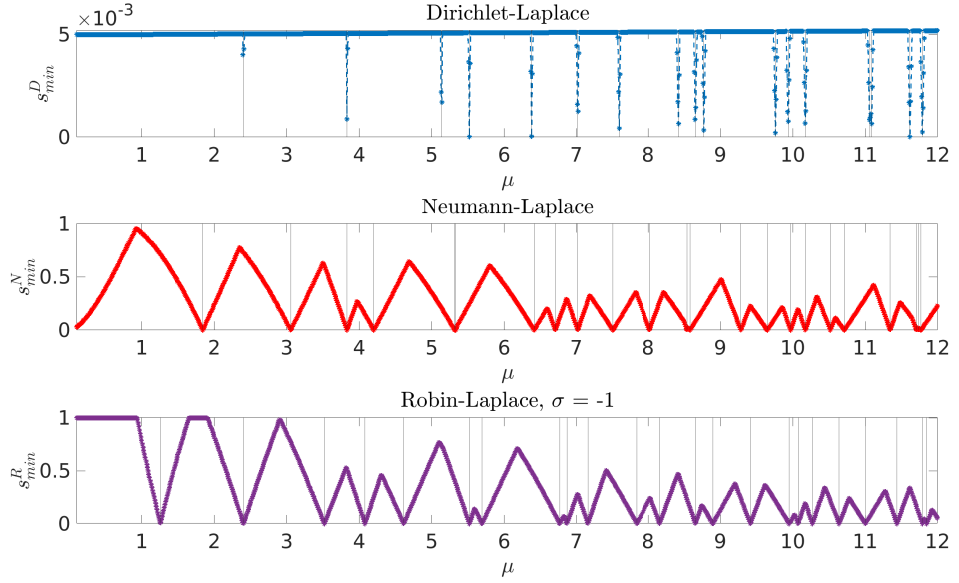


Figure 3.1: Minimum singular values of B_μ (Dirichlet-Laplace, s_{min}^D , top, blue), $A_\mu + Id$ (Neumann-Laplace, s_{min}^N , middle, red) and C_μ (Robin-Laplace $\sigma = -1$, s_{min}^R , bottom, purple) for the unit disk with $\mu \in [0.1, 12]$. Computed eigenvalues correspond to local minimas of s_{min}^i , $i = D, N, R$. The vertical lines correspond to the true eigenvalues.

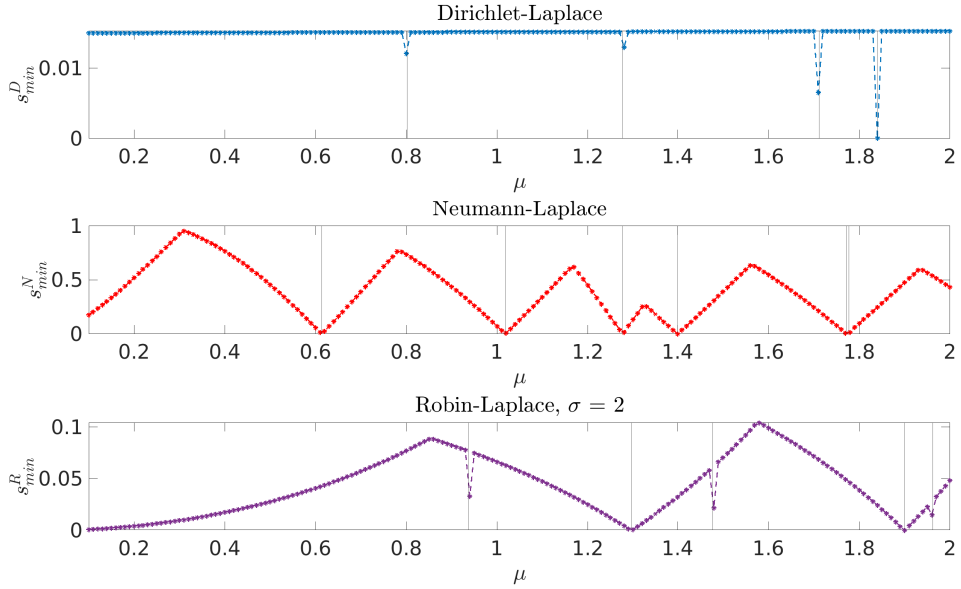


Figure 3.2: Minimum singular values of B_μ (Dirichlet-Laplace, s_{min}^D , top, blue), $A_\mu + Id$ (Neumann-Laplace, s_{min}^N , middle, red) and C_μ (Robin-Laplace $\sigma = 2$, s_{min}^R , bottom, purple) for the disk of radius 3 with $\mu \in [0.1, 2]$. Computed eigenvalues correspond to local minimas of s_{min}^i , $i = D, N, R$. The vertical lines correspond to the true eigenvalues.

We observe that our approach is able to locate the Dirichlet, Neumann and Robin eigenvalues of the Laplacian. To accurately find their value, we can perform a refined search around the local minima of singular values to get more digits of accuracy. We could also interpolate the singular values followed by a root finding algorithm. We first use sign flipping as described in [BT05] and then interpolate the sign flipped s_{min}^i , $i = D, N, R$ using Radial Basis Functions (RBFs)[Car+01].

Remark 3.1.1 (Sign Flipping). *From Figure 3.1 and Figure 3.2 we note that the values of μ that we are interested in, correspond to local minimas of the s_{min} curves. To convert to a problem of finding zeros instead of minimas we perform sign flipping at the local minimas as described in Section 9 of [BT05]. We borrow code from figure 9.1 in [BT05] corresponding to “signed subspace angles” to do this.*

Remark 3.1.2 (RBFs). *After sign flipping, we use RBFs to interpolate the sign flipped points of s_{min} using the inverse multiquadric as described in [Car+01]. We briefly describe the interpolation strategy. Suppose we have m function evaluations of some unknown function $f = \{f_i\}_{i=1}^m$. Now choose an RBF ϕ_{RBF} . We want to find an interpolating function f_{RBF} chosen from a particular space of distributions (see problem 3.1 in [Car+01]). The interpolant*

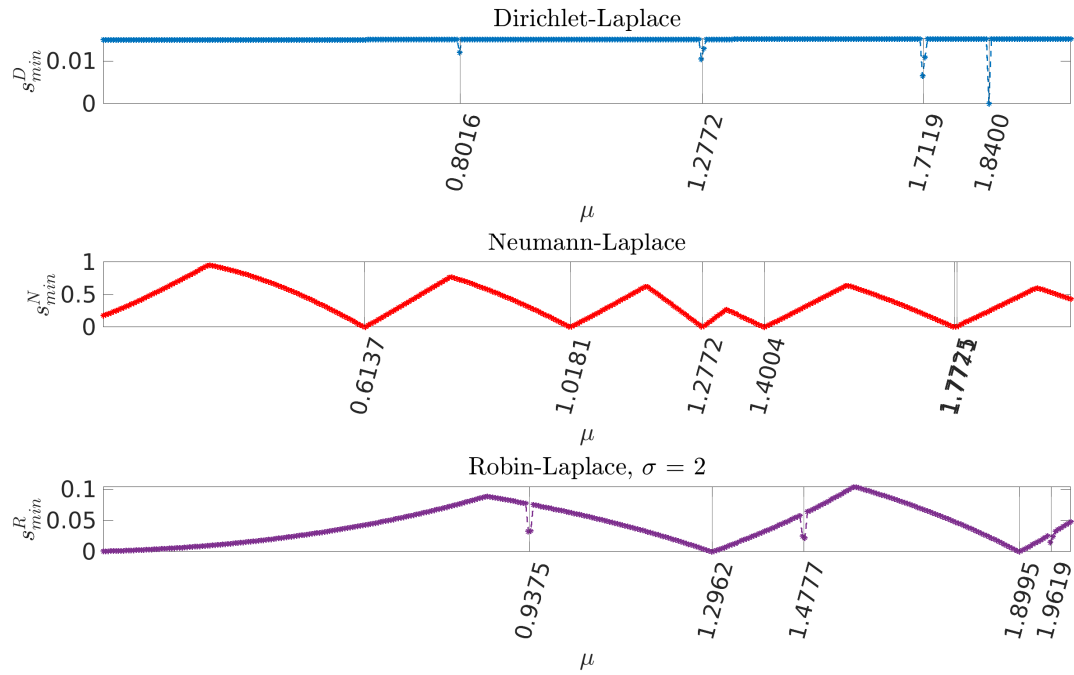
$$f_{RBF}(x) = \sum_{i=1}^{2N} \eta_i \phi_{RBF}(|x - x_i|) \quad (3.1)$$

minimizes a semi-norm which characterizes smoothness (see problem 3.1 and equations 5,6 in [Car+01], we do not use the polynomials). So our goal is to try to find these coefficients $\{\eta_i\}_{i=1}^{2N}$. For each point x_j that we have the function evaluation we require $f_j = f_{RBF}(x_j) = \sum_{i=1}^m \eta_i \phi_{RBF}(|x_j - x_i|)$, $j = 1, \dots, m$. This leads to a linear system $A_{rbf}\eta = f$, where $A_{rbf}^m = [\phi_{RBF}(|x_j - x_i|)]$. We can then obtain $\eta = A_{rbf}^{-1}f$. We use the inverse multiquadric RBF throughout this thesis $\phi_{RBF}(r) = \frac{1}{\sqrt{c^2 + r^2}}$, $c = 0.05$ (see Section 3 [Car+01]). We describe the process below in Algorithm 2.

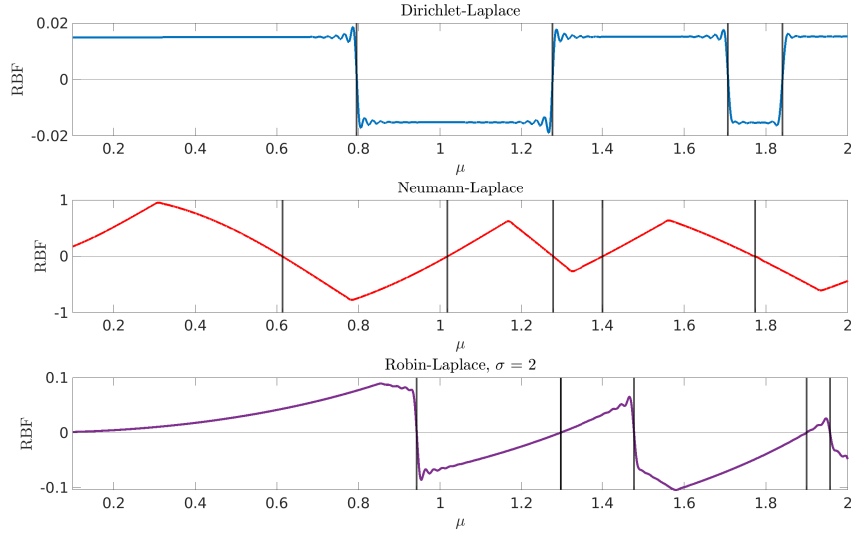
Algorithm 2 RBF interpolation of function evaluations for f , see Appendix B.6

Require: Evaluations $\{f_i\}_{i=1}^m$, evaluation points $\{X_i = (x_i, y_i)\}_{i=1}^m$, choice of `rbf` ϕ
The interpolation points are `rbf_points` = $\{X_i\}$ and the function to interpolate is `rbf_f` = $\{f_i\}$
Create `meshgrid` of $x_i = [x_\tau, x_t]$ and $y_i = [y_\tau, y_t]$
Compute the distance between all `rbf_points` and store in `R_rbf`.
Create matrix of rbf evaluations, `A_rbf`=[$\phi(x_t - x_\tau, y_t - y_\tau)$]
Compute the RBF coefficients $\eta = \text{rbf_coeffs} = \text{A_rbf}^{-1} \text{ rbf_f}$
To compute the function value of the interpolant f_{RBF} at any point $Z \subset \mathbb{R}^2$, set $f(Z) = 0$
for $i = 1, \dots, m$ **do**
 $r_i = |Z - X_i|$
 $f_{RBF}(Z) = f_{RBF}(Z) + \eta_i \phi(r_i)$
end for

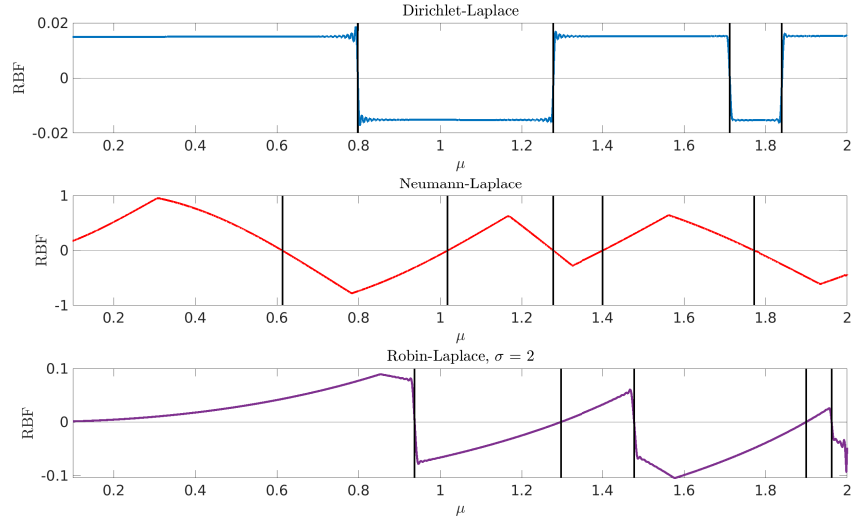
In [Figure 3.3](#) (a) we again show the minimum singular values for the configuration of [Figure 3.2](#). The vertical lines correspond with values of μ for which μ^2 corresponds to the Dirichlet, Neumann and Robin Laplace eigenvalues. In subfigure (b), we show the corresponding RBF interpolating function for the sign flipped s_{min} curves and the approximate zeros located by `fzero` in MATLAB. We observe that this approach recovers most of the eigenvalues with some exceptions, like the first true Dirichlet eigenvalue is incorrectly recovered as 0.7956 instead of 0.8016 and the last Neumann eigenvalue is missed altogether. If we reduce the step size in the μ search by half i.e. step with $0.5e - 2$ instead, we observe better recovery but still miss the last Neumann eigenvalue, see subfigure (c). However, we note from the minimum singular values of the Neumann-Laplace eigenvalues in subfigure (a) that there are 2 local minima very close by which might explain why sign-flipping was unable to capture them both. To resolve this, we suggest a combination of refining or shortening the search grid and subsequent sign-flipping, interpolation and root finding.



(a) Minimum singular values of B_μ (Dirichlet-Laplace, s_{min}^D , top, blue), $A_\mu + Id$ (Neumann-Laplace, s_{min}^N , middle, red) and C_μ (Robin-Laplace $\sigma = 2$, s_{min}^R , bottom, purple) for the disk of radius 3 with $\mu \in [0.1, 2]$. Computed eigenvalues correspond to local minimas of $s_{min}^i, i = D, N, R$. The vertical lines correspond to the true eigenvalues.



(b) Sign flip and RBF interpolation of s_{min}^i , $i = D, N, R$ with μ search step size $1e-2$. Computed eigenvalues correspond to zeros of the RBFs. The vertical lines correspond to the approximated eigenvalues.



(c) Sign flip and RBF interpolation of s_{min}^i , $i = D, N, R$ with μ search step size $0.5e-2$. Computed eigenvalues correspond to zeros of the RBFs. The vertical lines correspond to the approximated eigenvalues.

Figure 3.3: Roots of sign-flipped and RBF interpolated s_{min}^i , $i = D, N, R$, for the disk of radius 3 with $\mu \in [0.1, 2]$.

As discussed above, these wave numbers μ are particularly important because our method only works away from these and so we need to avoid these numbers. We observe through our experiments that for λ^D of multiplicity m , as $\mu^2 \rightarrow \lambda^D$ from the left, $\sigma_i \rightarrow -\infty$, $i = 1 \rightarrow m$, which is

expected from Theorem 7.4.8 in [LMP22]. In [Section 3.2](#) we investigate the behaviour of eigenvalues and eigenfunctions as we approach λ^D . There is also a connection between the Robin-Laplace ([Equation 1.1](#)) and Steklov-Helmholtz ([Equation 1.2](#)) eigenvalue problems. We note that for the Robin problem we fix σ and look for μ whereas for the Steklov problem we do the opposite. In fact, they share a reciprocity of eigenvalues and similar homothetic properties (see [Section 3.5.2](#)).

Remark 3.1.3 (Computing eigenfunctions of the Dirichlet-Laplace eigenvalue problem). *In [Algorithm 1](#), we compute the SVD of the matrix B_μ which corresponds to the discretized single layer. The right vectors corresponding to the local minima of the minimum singular values s_{\min}^D are the corresponding eigendensities and we compute the corresponding eigenfunctions using B_μ . We can similarly compute the Neumann/Robin-Laplace eigenfunctions.*

3.1.3 Steklov-Helmholtz problem on the disk

Consider the Steklov-Helmholtz problem ([1.2](#)) on a disk of radius R . As we saw in [Section 1.4.2](#), on a disk of radius R , the function $u_n(r, \theta) = J_n(\mu r)e^{in\theta}$ satisfies $-\Delta u - \mu^2 u = 0$, where $0 \leq r \leq R$ and $\theta \in [0, 2\pi)$. Applying the Steklov boundary condition we get,

$$\mu J'_n(\mu R)e^{in\theta} = \tilde{\sigma}_n J_n(\mu R)e^{in\theta} \implies \tilde{\sigma}_n = \frac{\mu J'_n(\mu R)}{J_n(\mu R)} = \frac{\mu}{2} \frac{J_{n-1}(\mu R) - J_{n+1}(\mu R)}{J_n(\mu R)},$$

with eigenfunctions $J_n(\mu r)e^{in\theta}$. When $n = 0$ we get $u_0(r, \theta) = J_0(\mu r)$ with a single eigenvalue $\tilde{\sigma}_0$. The rest $\tilde{\sigma}_n$, $n \in \mathbb{N}$ are of multiplicity 2 with eigenfunctions $J_n(\mu r) \cos(n\theta)$ and $J_n(\mu r) \sin(n\theta)$.

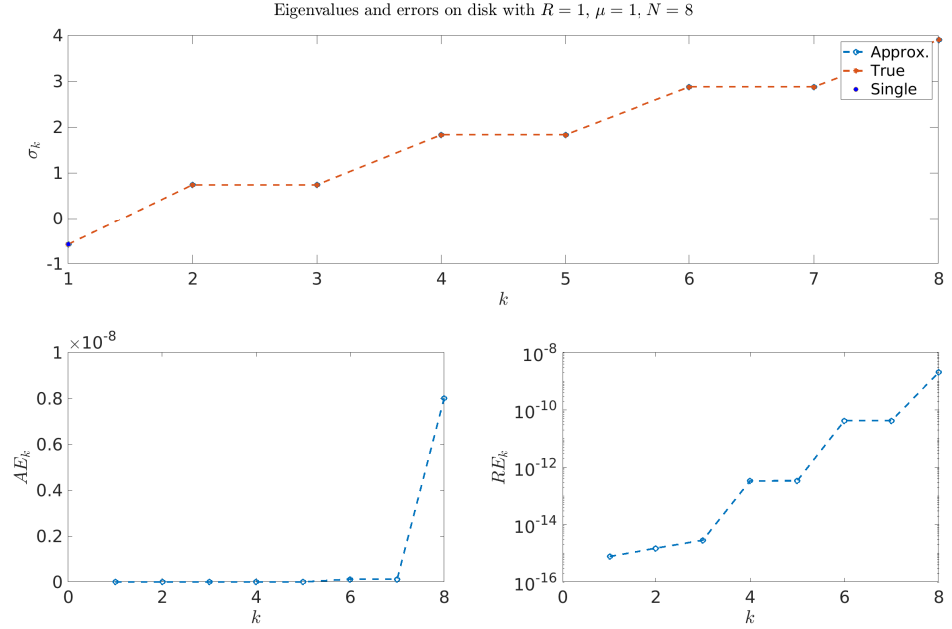
Remark 3.1.4 (Sorting eigenvalues). *From [Figure 1.4](#), we observe that the Steklov-Helmholtz eigenvalue of the circle are not necessarily in ascending form. That is, $\tilde{\sigma}_0$ is not the smallest eigenvalue. So, we compare the eigenvalues after sorting them and refer to the set $\{\sigma_k\}_{k=1}^N$ as the sorted eigenvalues.*

Let σ_k^{true} be the k th sorted eigenvalue and σ_k be its approximation. The absolute error of the k th sorted eigenvalue AE_k and its absolute relative error RE_k are computed as,

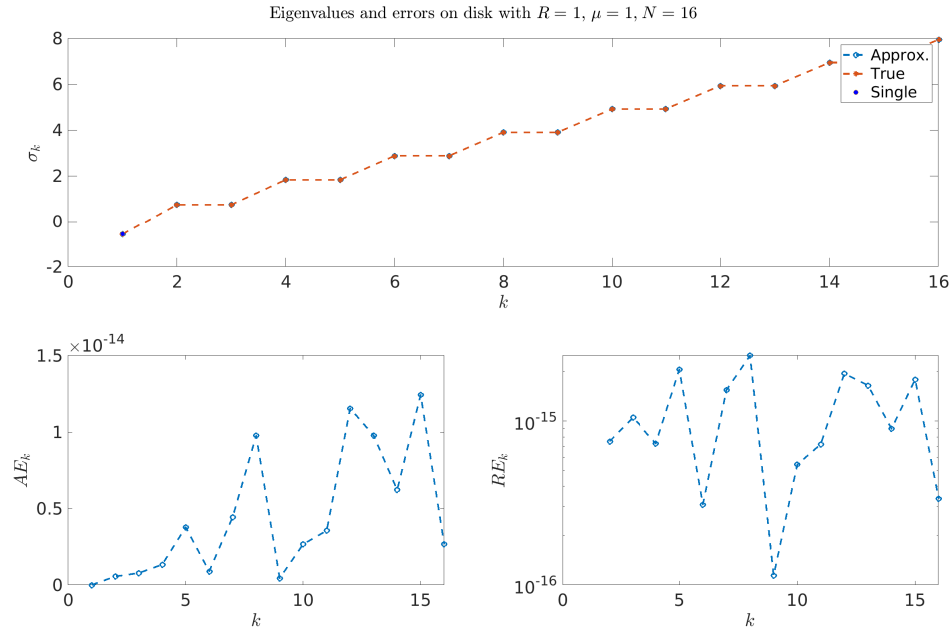
$$AE_k := |\sigma_k^{true} - \sigma_k|, \quad (3.2) \quad RE_k := AE_k / |\sigma_k^{true}|. \quad (3.3)$$

In [Figure 3.4](#) we show the true and computed eigenvalues along with the absolute errors and absolute relative errors. There are six subfigures (a)-(f), each of which has three plots over two rows. In a single plot in the top row of each subfigure, we show σ_k^{true} (red), σ_k (light blue) for $k = 1, \dots, N$ and point out the eigenvalue of multiplicity one for the disks. The second row of each subfigure contains two plots of the errors, AE_k (left) and RE_k (right). We observe that if N is not large enough in relation to the radius R and wave number μ , then our method is unable to capture the Steklov-Helmholtz eigenvalues. We observe in subfigure (c) that for $R = 1$ and $\mu = 5$, $N = 16$ is not large enough but as we see in subfigure (d), $N = 32$ works very well. Then we observe

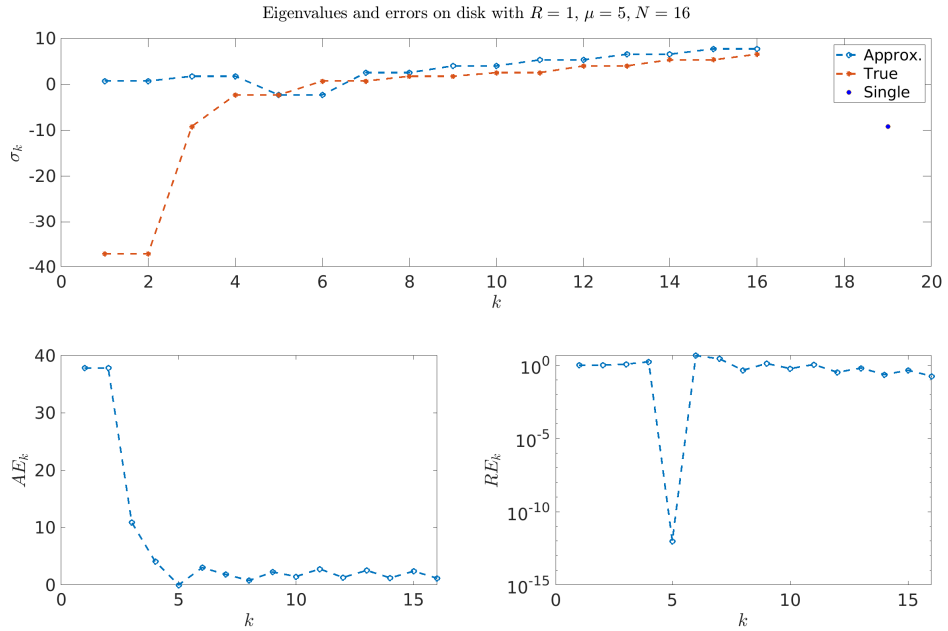
in subfigures (e) and (f) that for $R = 7$ and $\mu = 20$, $N = 300$ is not enough but $N = 380$ is large enough.



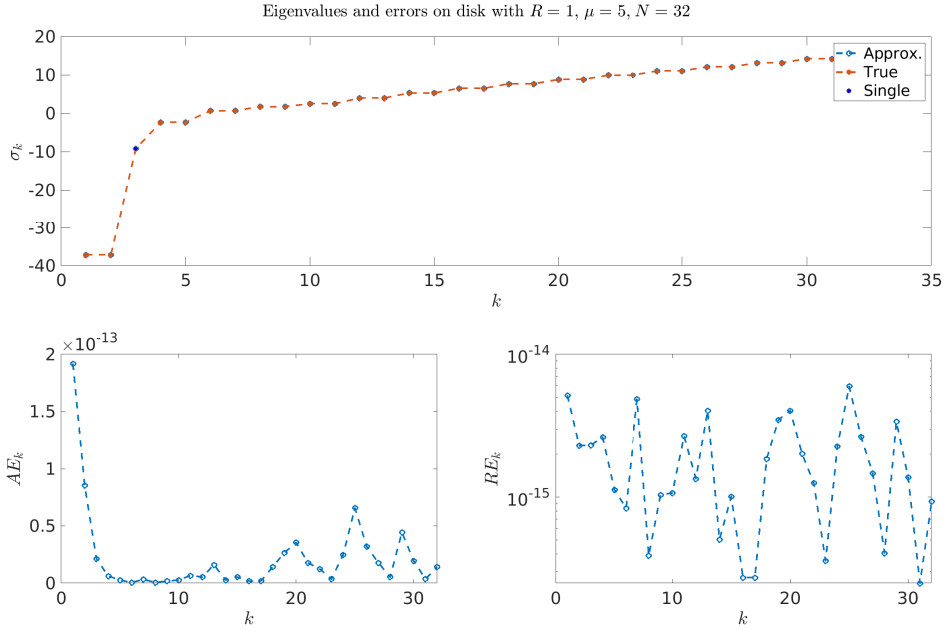
(a) For $R = 1, \mu = 1$ and $N = 8$, we observe convergence of the first 8 eigenvalues, and the errors increase with k .



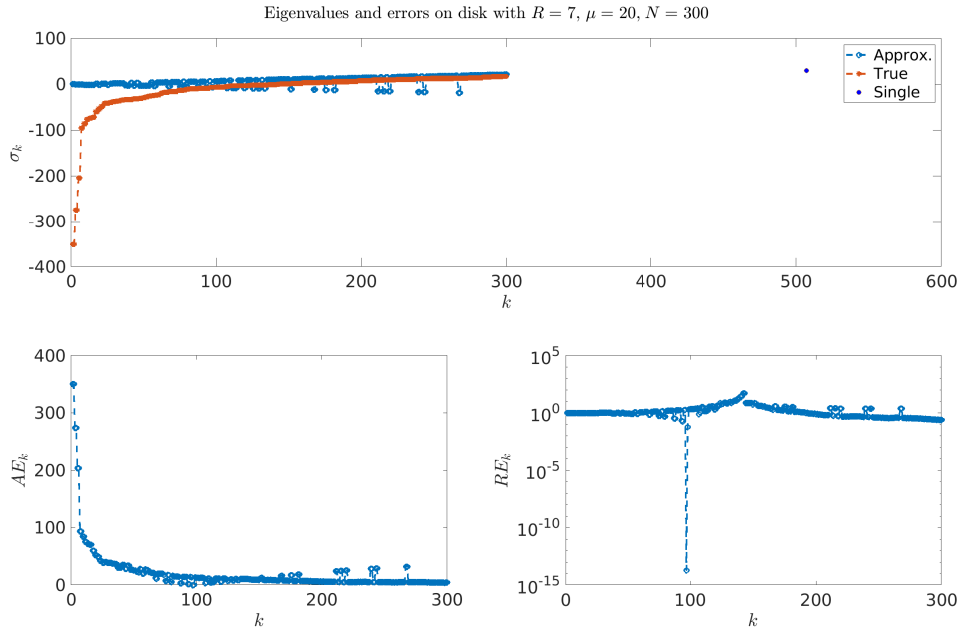
(b) For $R = 1, \mu = 1$ and $N = 16$, we observe machine precision for the first 16 eigenvalues.



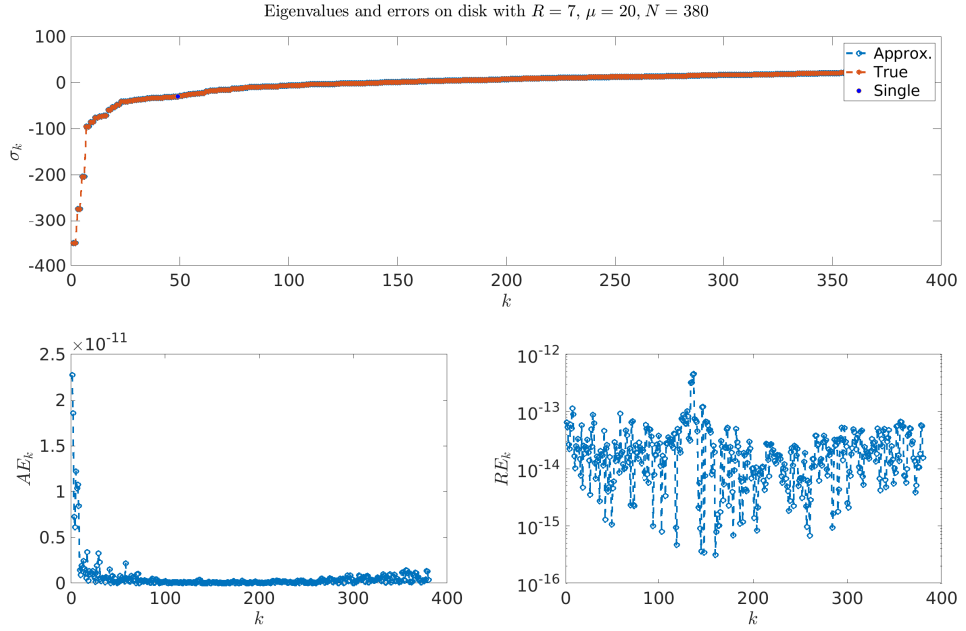
(c) For $R = 1, \mu = 5$ and $N = 16$, we observe that N is not large enough to recover σ_k^{true} .



(d) In comparison to subfigure(c) for $R = 1$ and $\mu = 5$ we increase N to 32. We observe machine precision for the first 32 eigenvalues.



(e) For $R = 7, \mu = 20$ and $N = 300$, we observe that N is not large enough to recover σ_k^{true} .



(f) In comparison to subfigure(e) for $R = 7$ and $\mu = 20$ we increase N to 380. We observe machine precision for the first 380 eigenvalues.

Figure 3.4: In each subfigure we show the first N sorted eigenvalues σ_k^{true} (red) and σ_k (light blue) $k = 1, \dots, N$ and the eigenvalue of multiplicity 1 (top row). We show the absolute errors AE_k (bottom row, left) and absolute relative errors RE_k (bottom row, right) for disks with various configurations of radius R , wave number μ and N .

We observe that we are able to approximate the first N eigenvalues of disks with machine precision as long as we take N large enough with respect to the radius R and wave number μ . As we increase the input (μR) and order (n) of MATLAB's `besselj` function, numerical errors increase as well, i.e. `besselj` is not able to compute σ_k^{true} correctly for large inputs. This might explain to some degree why we see slightly worse relative error for the higher eigenvalue numbers k . We compute,

$$\|RE\|_2 := \sqrt{\sum_{k=1}^N RE_k^2} = \sqrt{\sum_{k=1}^N \frac{|\sigma_k^{true} - \sigma_k|^2}{|\sigma_k^{true}|^2}}, \quad (3.4)$$

where RE_k is as defined in [Equation 3.3](#).

To investigate this further, we plot the squares of the discrete 2-norm of the relative errors (3.4) for fixed R and different μ s in [Figure 3.5](#) and [Figure 3.6](#). In [Figure 3.5](#), we compute $\|RE\|_2$ with respect to σ_k^{true} . Since MATLAB is unable to compute σ_k^{true} for all $k \leq 1024$, we instead consider the true Steklov-Helmholtz eigenvalues as those computed by a larger N in [Figure 3.6](#). Recall the notation σ_k^N where we emphasize N used in our approximation. In [Figure 3.6](#) we consider the true eigenvalues to be those as computed by setting $\sigma_k^{true} := \sigma_k^{1024}$ for $R < 7$ and $\sigma_k^{true} := \sigma_k^{2048}$. We observe a better convergence of eigenvalues when we consider approximated eigenvalues (compare [Figure 3.5](#) and [Figure 3.6](#)). We note a higher increase in errors for larger N in [Figure 3.5](#) due to errors in MATLAB's `besselj` (and possibly round-off errors) as compared to the round-off errors in the approximated eigenvalues in [Figure 3.6](#). In any case, we observe exponential convergence.

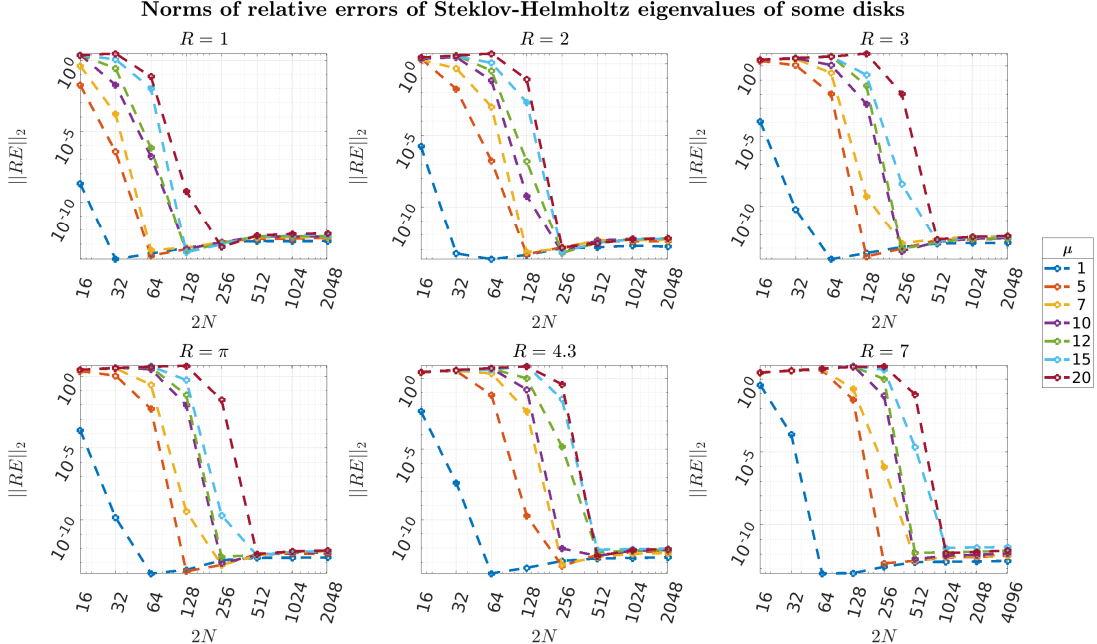


[Figure 3.5](#): Norms of relative errors $\|RE\|_2$ of σ_k against $2N$ across various disks and wave numbers μ with respect to σ_k^{true} . In each subplot, we fix R and vary μ .

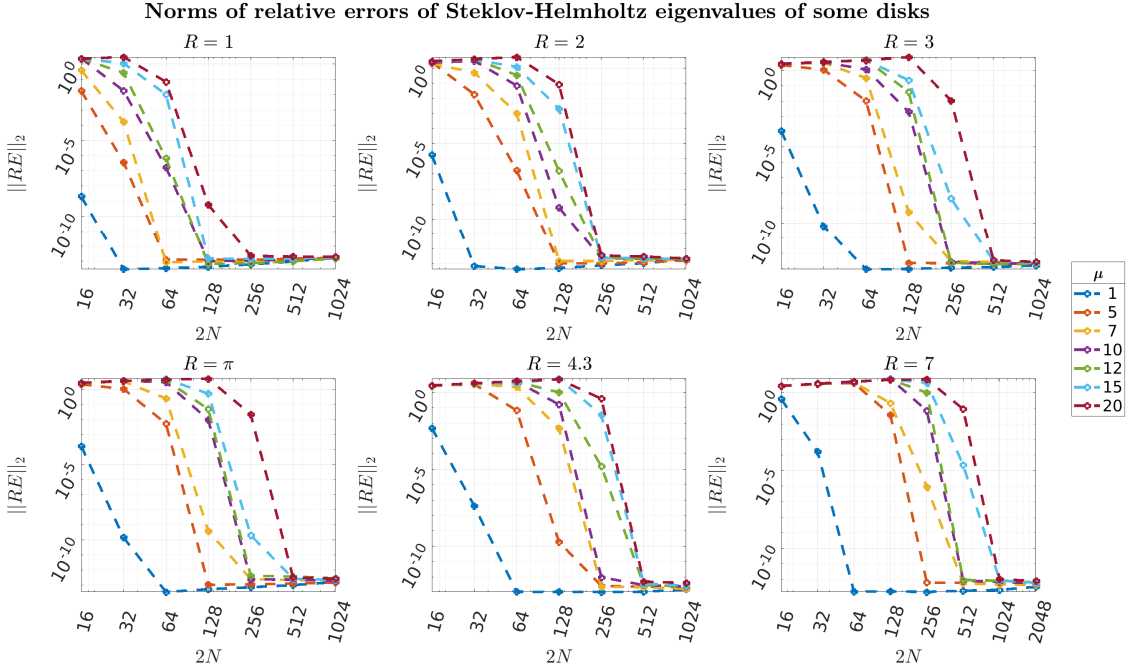


Figure 3.6: Norms of relative errors $\|RE\|_2$ of σ_k against $2N$ of across various disks and wave numbers μ where we set $\sigma_k^{true} := \sigma_k^{1024}(R \neq 7)$ and $\sigma_k^{true} := \sigma_k^{2048}(R = 7)$. In each subplot, we fix R and vary μ .

Like in [Figure 3.4](#), we observe a clear dependence of N on μ and R to achieve a given precision for the Steklov-Helmholtz eigenvalues $\{\sigma_k\}$. On increasing either μ or R , we need to take more points on the M .

In [Figure 3.7](#) we try to explore this dependence which seems to be on the product of R and μ , equivalently $|M|\mu$ for the circle (see [Figure 3.15](#) for other curves). We compute $\{\sigma_k^N\}_{k=1}^N$ for $N = 2^i, i = 3, \dots, 9$ for various combinations of R, μ and record in the heatmap below the first value of N for which we observe machine precision for $\|RE\|_2$. So for $\mu = 7$ and 10 , $N = 128$ is the smallest power of 2 for which $\|RE\|_2$ gives required precision.

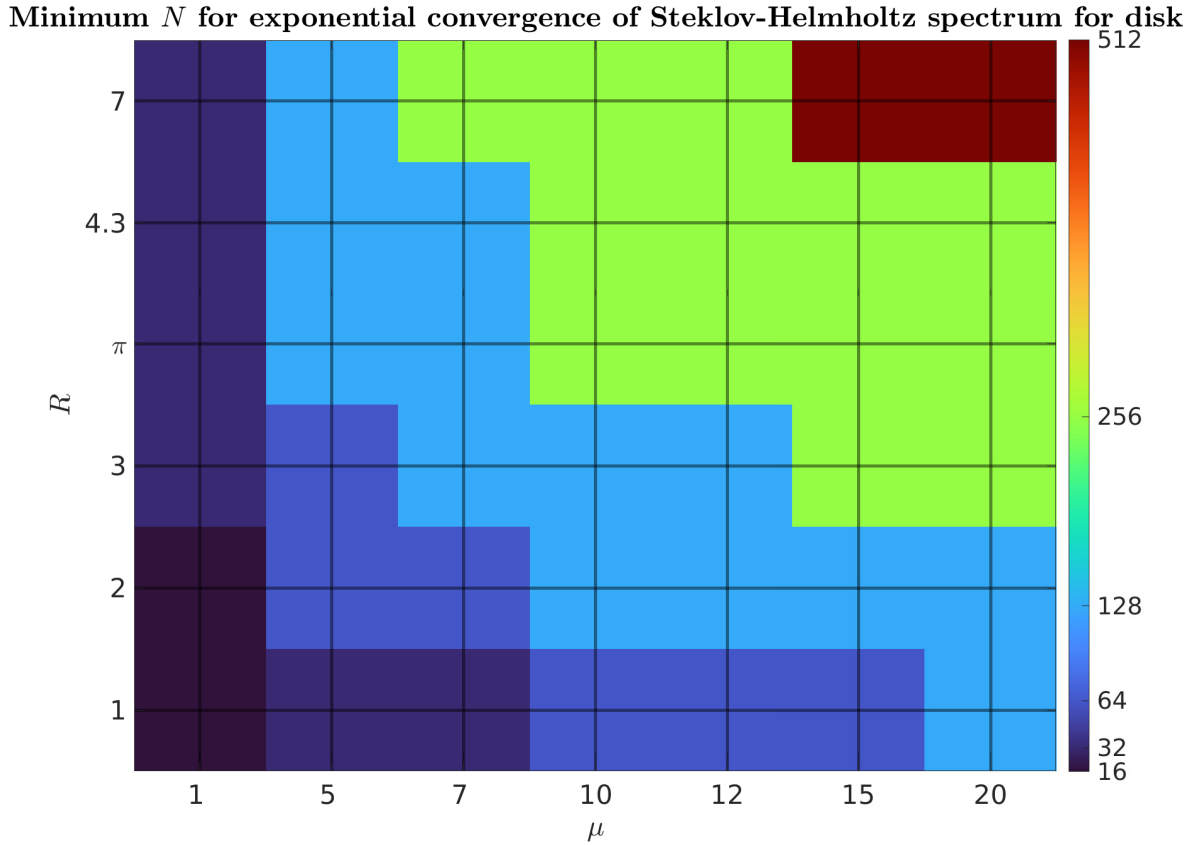


Figure 3.7: N , which is the smallest power of 2 for which $\|RE\|_2$ is of machine precision for the Steklov-Helmholtz spectrum of disks of various radii R and various wave numbers μ .

3.1.3.1 Errors of eigenfunctions on the disk

By construction we have that the single layer potential solves the Helmholtz equation inside the domain. So using the computed eigendensities and the matrix of the discretized single layer, B (see [Equation 2.17](#)) we can compute the eigenfunctions inside the domain Ω . We recall that a disk has one eigenvalue of multiplicity one (corresponding to Bessel order 0) and the rest of the eigenvalues are each of multiplicity two. So for the double eigenvalues the computed eigenfunction is in the span of $\{u_{k,i}\}_{i=1}^2$. First we discretize the domain Ω , with a grid of $m \times m$ points $\{x_i\}_{i=1}^{m^2}$ inside each disk and we interpolate $\{u_k(x_i)\}_{i=1}^{m^2}$ [similarly $\{u_k^N(x_i)\}$] by the `griddata` function with cubic interpolation. We set $m = 150$ and denote the true solution for the k th density by $u_k(x_j)$ and the approximate solution by $u_k^N(x_j)$. At each grid point we compute for fixed $x_j \in \Omega$,

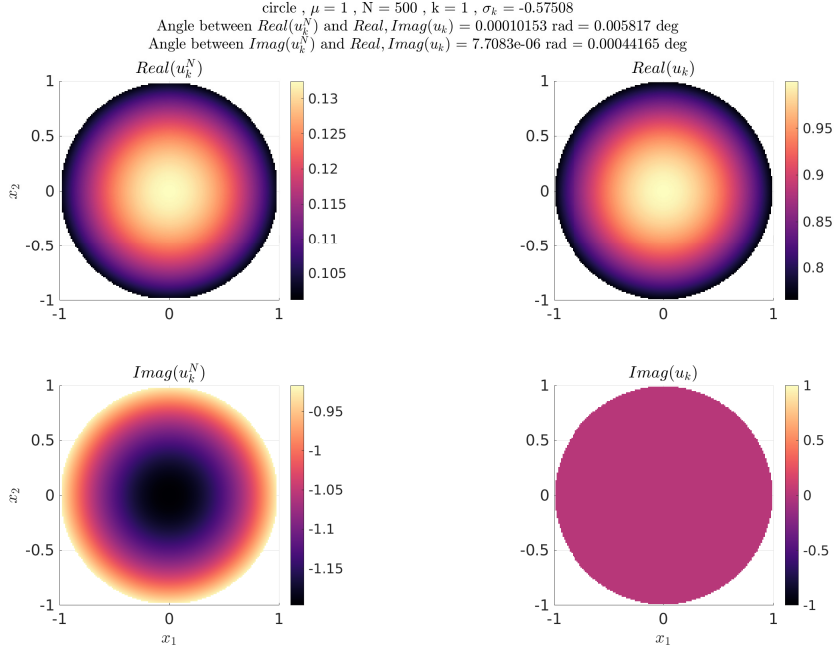
$$u_k(x_j) = \int_0^{2\pi} \frac{i}{4} H_0^1(\mu r(x_j, \tau)) \psi_k(\tau) |x'(\tau)| d\tau, \quad \text{similarly for } u_k^N(x_j). \quad (3.5)$$

For the disk since $|x'(\tau)| = R$ this becomes

$$u_k(x_j) = R \int_0^{2\pi} \frac{i}{4} H_0^1(\mu r(x_j, \tau)) \psi_k(\tau) d\tau, \text{ similarly for } u_k^N(x_j).$$

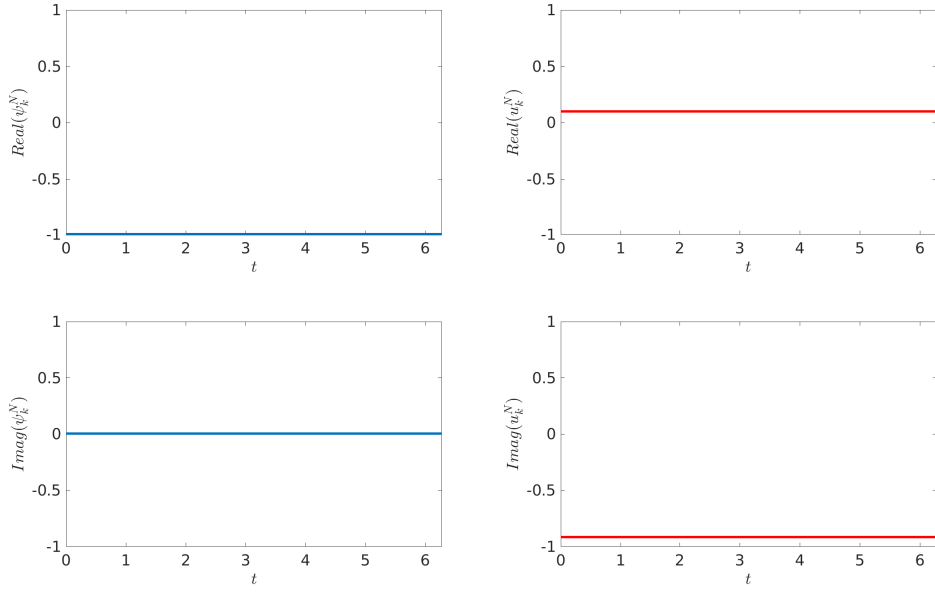
As noted in [Table 1.2](#), we know that the Steklov-Helmholtz eigenvalues for the disk are $u_k(r, \theta) = J_k(\mu r) \exp(ik\theta)$ and directly compute them. To compare how well we approximate the Steklov-Helmholtz eigenfunctions for the disk we use MATLAB's `subspace` function. We compute the angle between the subspace generated by the approximate k th eigenfunction (u_k^N) and the true k th eigenfunction (u_k) in the disk. The function works by projecting the vector of smaller dimension onto the *bigger* vector (matrix) and then computing the \sin^{-1} of the norm of the projection (the projection is computed as equation 28 in [\[BG73\]](#)). MATLAB's `subspace` function first computes an orthogonal basis for the range of the vectors (in case of rank deficiency). If the subspace angles are *small*, we interpret that involved vectors are linearly dependent. So when comparing the true and computed eigenfunctions, we hope to see small subspace angle values.

In [Figure 3.8](#) and [Figure 3.9](#) we show some eigenfunctions for various μ, R, k inside the disk and on the boundary. In [Figure 3.8](#) we look at the first and 20th eigenfunctions without counting multiplicities and wave number $\mu = 1$ for the unit disk. Here σ_1 is a single eigenvalue, and the rest are double. In the subfigures on the left, we compare the computed and true eigenfunctions inside Ω . In the subfigures on the right, we compare the computed and true eigenfunctions on the boundary M . For the configuration in [Figure 3.9](#) we set $\mu = 10$ and $R = 7$. Now the subspace angles are much higher in the domain. So we increase the number of grid points inside from $m = 150$ to $m = 300$. We note the subspace angles between the real part (similarly imaginary part) of the computed solution and the real and imaginary parts of the true solution. Note that the eigenfunctions on the boundary approximate the true eigenfunctions better than on the inside and this is expected because we construct the functions on the boundary using the spectral method. Inside Ω we are interpolating out to a grid after evaluating $u_k(x_j)$, $\forall j$ with the use of MATLAB's `griddata` function. We could possibly improve on the inside by refining the grid or by using a better interpolation strategy (we will explore this in future work).

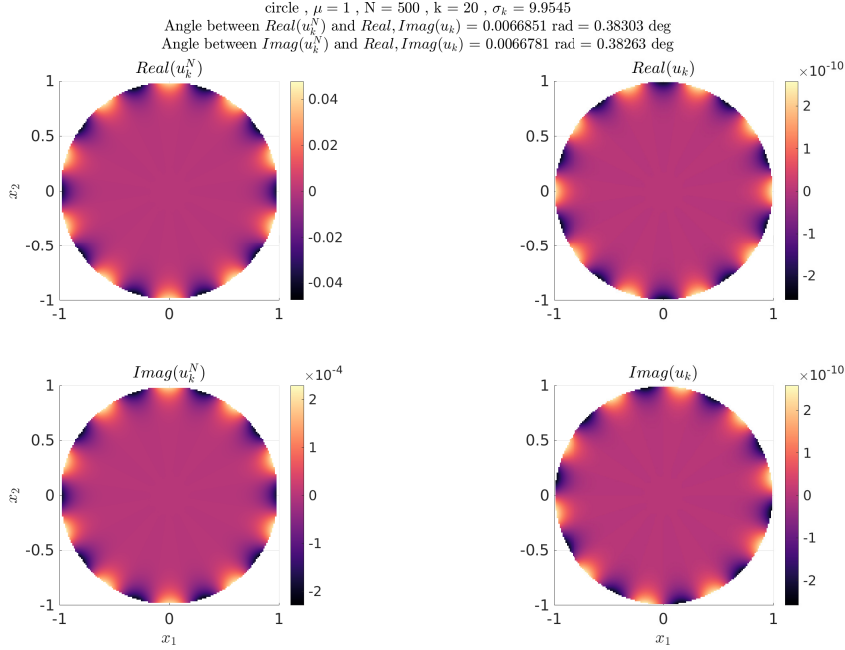


(a) For wave number $\mu = 1$ and disk radius $R = 1$, for $k = 1$ the subspace angles in Ω are small. We note that the imaginary part of the computed solution with the true solution is smaller than the subspace angle for the real part of the computed solution.

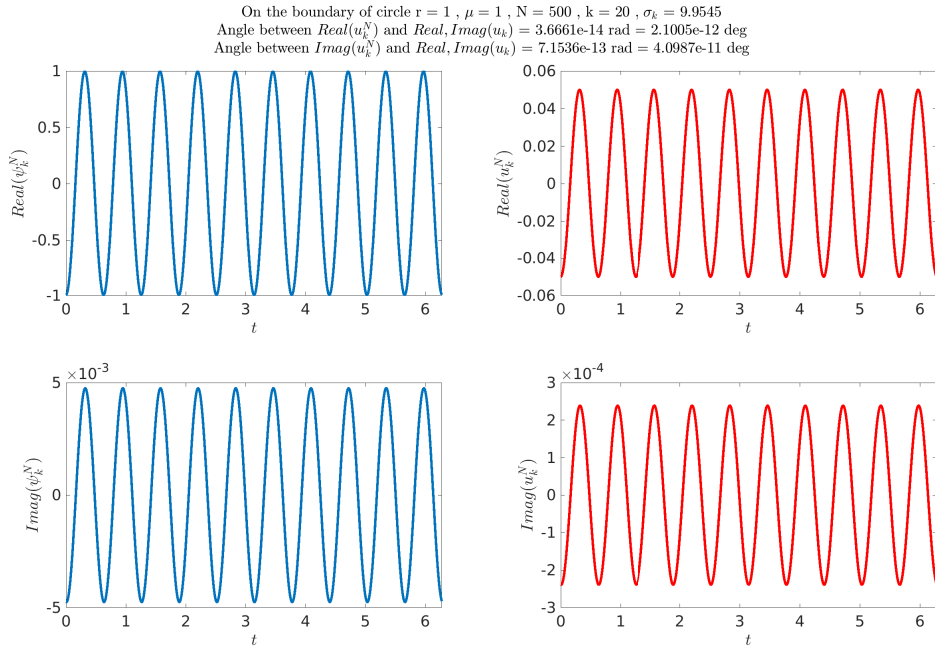
On the boundary of circle $r = 1$, $\mu = 1$, $N = 500$, $k = 1$, $\sigma_k = -0.57508$
 Angle between $Real(u_k^N)$ and $Real, Imag(u_k)$ = 8.3957e-15 rad = 4.8104e-13 deg
 Angle between $Imag(u_k^N)$ and $Real, Imag(u_k)$ = 1.1868e-15 rad = 6.7996e-14 deg



(b) For wave number $\mu = 1$ and disk radius $R = 1$, for $k = 1$ the subspace angles on M are of machine precision.

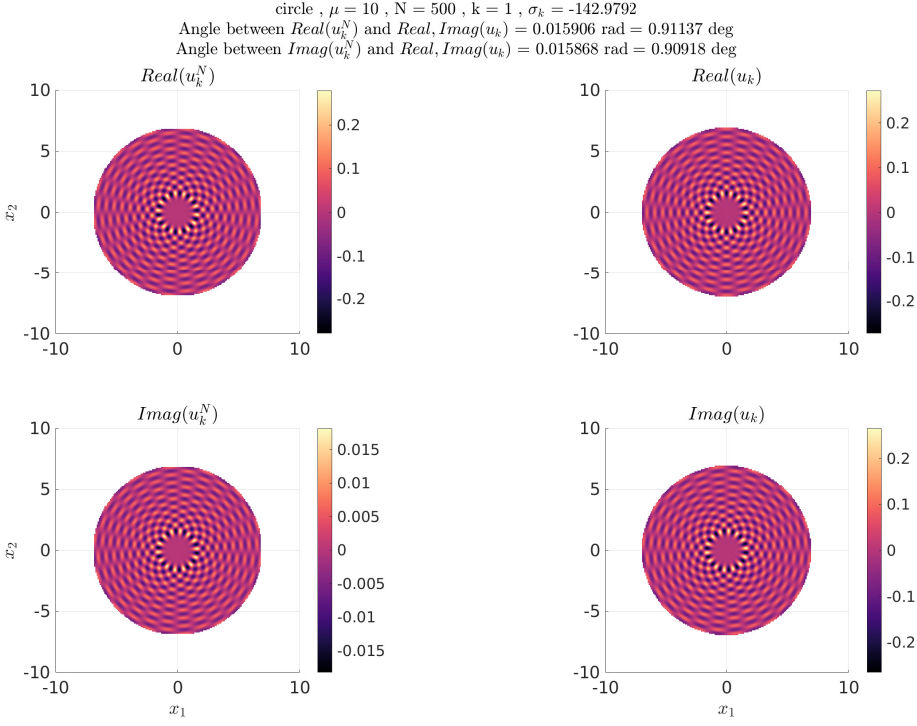


(c) For wave number $\mu = 1$ and disk radius $R = 1$, for $k = 20$, the subspace angles in Ω are have increased as compared to $k = 1$.

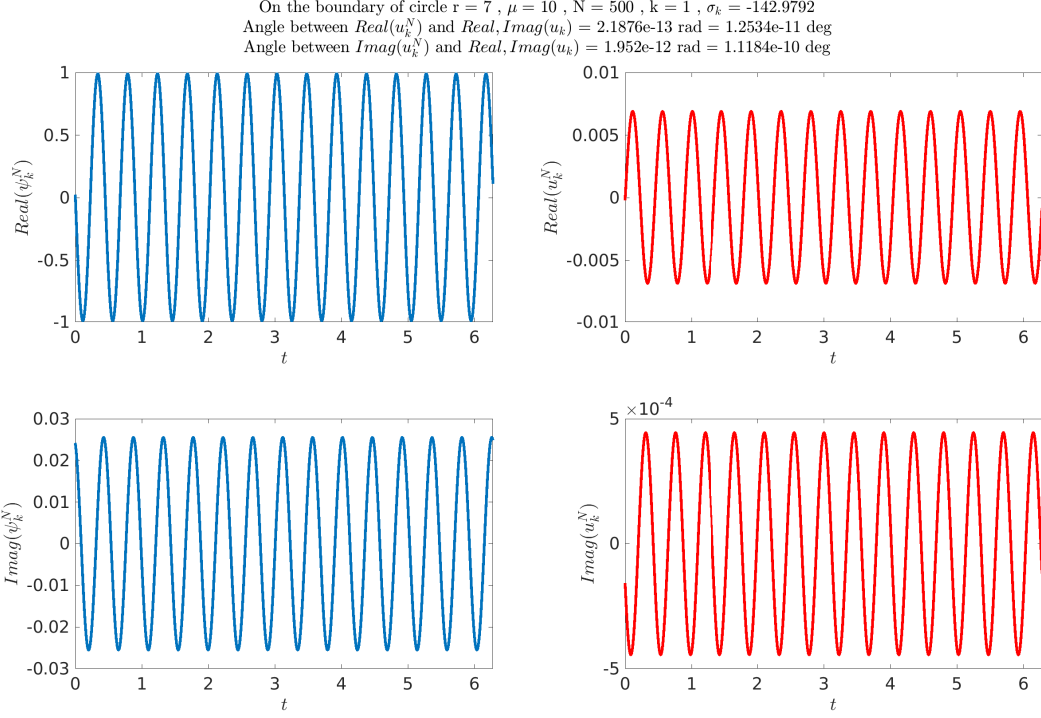


(d) For wave number $\mu = 1$ and disk radius $R = 1$, for $k = 20$ the subspace angles on M are *almost* of machine precision.

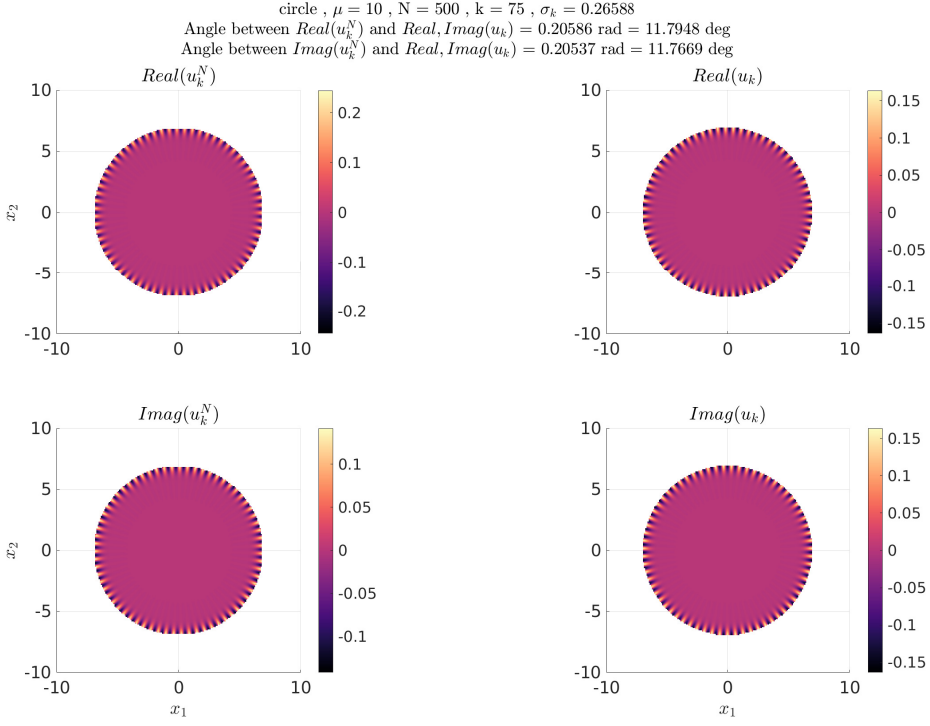
Figure 3.8: Comparing the computed and true, 1st and 20th Steklov-Helmholtz eigenfunctions of the unit disk, $\mu = 1$. We set $N = 500$ and $m = 150$. The subspace angles are reported in the figure titles.



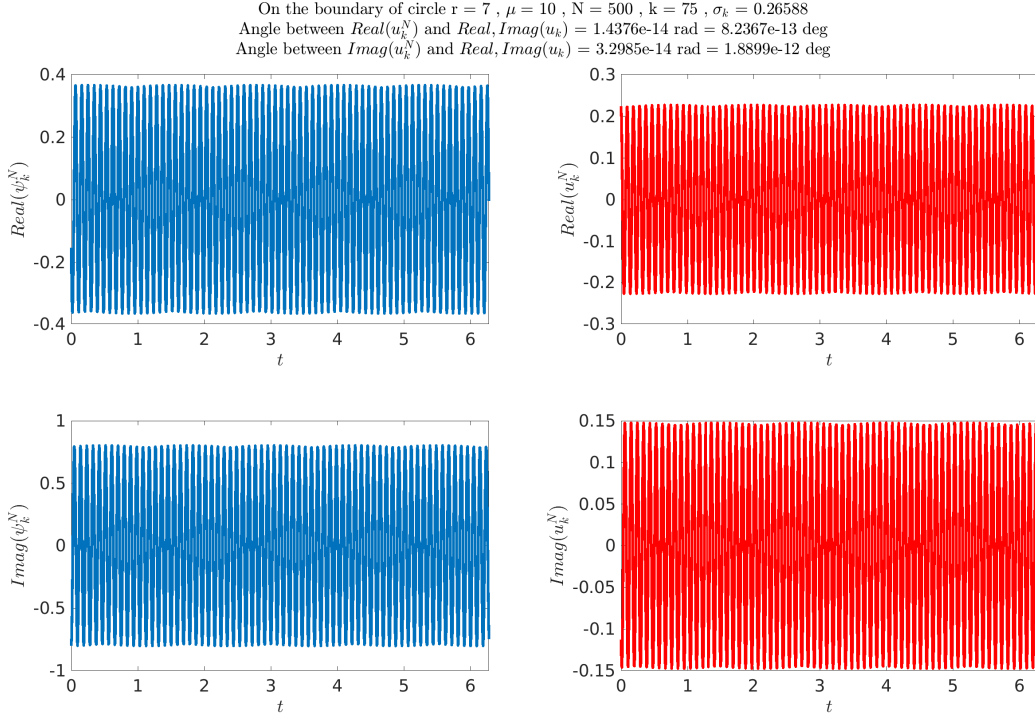
(a) For wave number $\mu = 10$ and disk radius $R = 7$, for $k = 1$ the subspace angles in Ω are small but almost 1 degree.



(b) For wave number $\mu = 10$ and disk radius $R = 7$, for $k = 1$ the subspace angles on M are much smaller as expected.



(c) For wave number $\mu = 10$ and disk radius $R = 7$, for $k = 75$ the subspace angles in Ω are quite large.



(d) For wave number $\mu = 10$ and disk radius $R = 7$, for $k = 75$ the subspace angles on M are much smaller as expected.

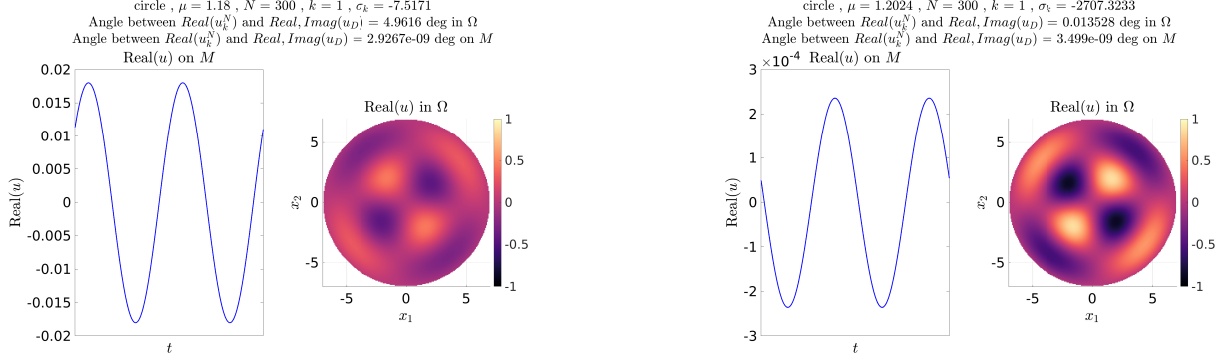
Figure 3.9: 1st and 75th Steklov-Helmholtz eigenfunctions of the disk of radius 7 with wave number 10. We set $N = 500$ and $m = 150$. The subspace angles are reported in the figure titles.

For this configuration, we increase m from 150 to 300 to check whether the subspace angles in Ω improve. We observe that for $k = 1$ the subspace angle for the real part decreases to 0.10414 degrees and to 0.008549 degrees for the imaginary part. For $k = 75$ the subspace angle for the real part decreases to 1.5825 degrees and to 1.6504 degrees for the imaginary part.

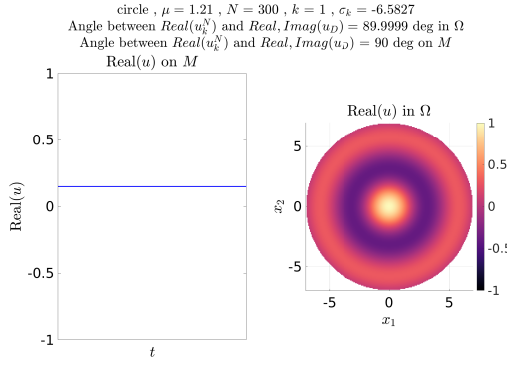
In the next section we test whether our approach behaves as expected when we push μ^2 to a Dirichlet-Laplace eigenvalue λ^D from the left. From Theorem 7.4.8 in [LMP22], we expect that $\sigma_1 \rightarrow -\infty$ as $\mu^2 \rightarrow \lambda^D$.

3.2 Approaching Dirichlet-Laplace eigenvalues

We have noted the behaviour of the first m Steklov-Helmholtz eigenvalues $\{\sigma_i\}_{i=1}^m$ as $\mu^2 \rightarrow \lambda^D$ at the end of [Section 3.1.2](#). We now consider sequences of wave numbers (μ_i) such that the sequences of (μ_i^2) approach Dirichlet eigenvalues of $-\Delta$. For each μ_i , we solve the related Steklov-Helmholtz eigenvalue problem. In [Figure 3.10](#) and [Figure 3.11](#), the angles in the plots are the **subspace** angles between the Dirichlet eigenfunctions u_D (computed as discussed in [Remark 3.1.3](#)) and Steklov-Helmholtz eigenfunctions u . As $\mu \rightarrow \mu_D$ we observe that $u \rightarrow u_D$ in Ω and $\sigma_1 \rightarrow -\infty$. For curves other than the disk and ellipse however, we note that on M the approximation is not as good as inside Ω (see figure [Figure 3.11b](#)). In this Section we show our experiments for a disk and the kite (see [Appendix A](#)). A Dirichlet-Laplace eigenvalue of the disk of radius 7 is $\approx 1.4459 = \lambda^D$ with $\mu_D = \sqrt{\lambda^D} \approx 1.20246$. We take wave numbers $\mu = 1.18, 1.19, 1.2, 1.2024, 1.21, 1.22$ and observe the behaviour of Steklov-Helmholtz eigenpairs. In [Figure 3.10](#) we show some of the Steklov-Helmholtz eigenfunctions and the Dirichlet-Laplace eigenfunction along with σ_1 against μ . Similarly we look at the kite where we compute a $\lambda^D \approx 2.20986$ in [Figure 3.11](#). Each figure has five subfigures. The first four subfigures have two plots, the eigenfunction on M (left) and the eigenfunction in Ω (right). In the first subfigure, we consider a wave number smaller than μ_D . In the second subfigure, we consider a wave number $\lesssim \mu_D$. In the third subfigure, we consider a wave number after μ_D . In the fourth subfigure, we show the Dirichlet-Laplace eigenfunction at μ_D . In the final subfigure, we plot σ_1 against μ for μ before and after μ_D .

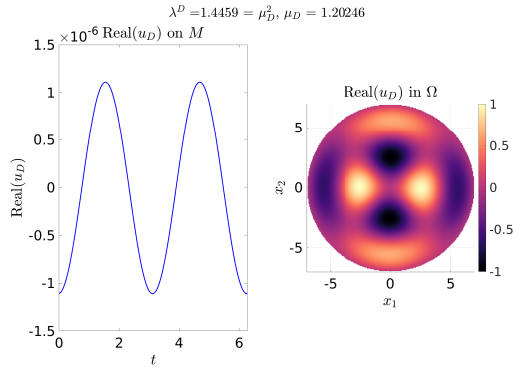


(a) $\mu^2 < \lambda^D$, we observe that the subspace angles between the Steklov-Helmholtz and Dirichlet-Laplace (d) eigenfunctions are not small enough, except on the boundary.

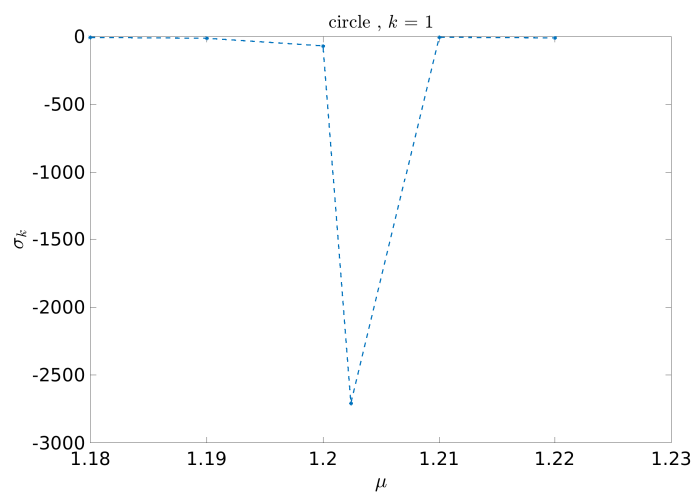


(c) $\mu^2 > \lambda^D$, we observe that the subspaces of Steklov-Helmholtz and Dirichlet-Laplace (d) eigenfunctions are perpendicular.

(b) $\mu^2 \approx \lambda^D$, we observe that the subspace angles between the Steklov-Helmholtz and Dirichlet-Laplace (d) eigenfunctions are small and note that $\sigma_1 \ll 0$.

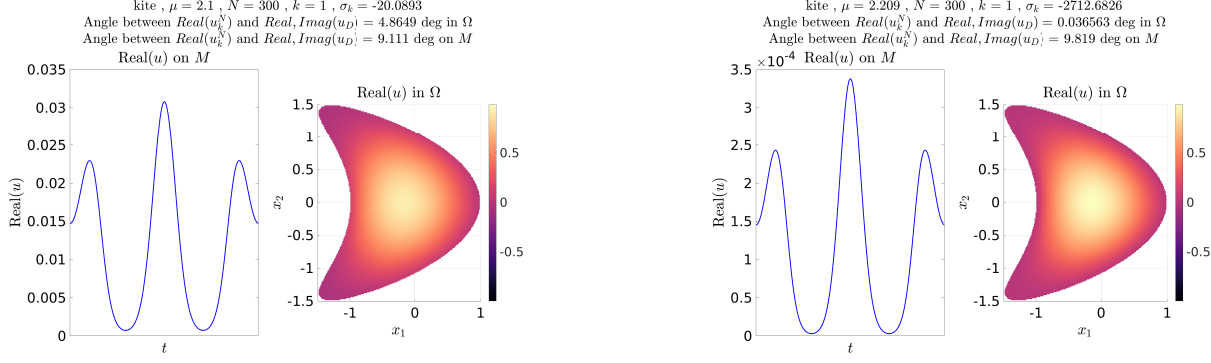


(d) Laplace-Dirichlet eigenfunction. We compare with (a),(b),(c).

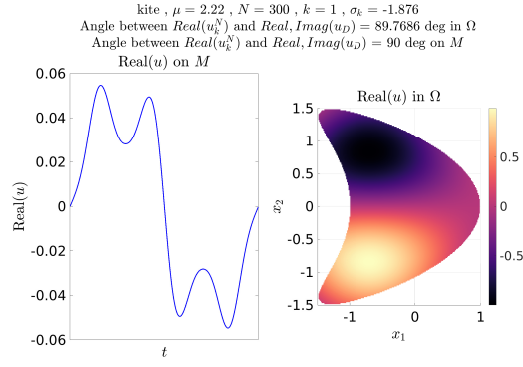


(e) σ_1 for wave numbers μ approaching μ_D and after μ_D . Observe that close to $\mu_D \approx 1.20246$ from the left, $\sigma_1 \rightarrow -\infty$.

Figure 3.10: Steklov-Helmholtz eigenpairs of the disk of radius 7 as $\mu^2 \rightarrow \lambda^D$. In subfigures (a)-(c) show Steklov-Helmholtz eigenfunctions and in (d) shows the Dirichlet-Laplace eigenfunction. In subfigure (e) shows σ_1 against μ .

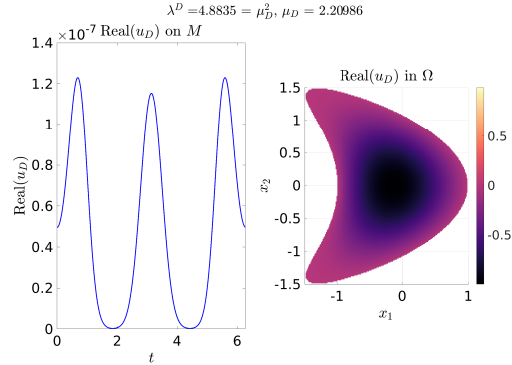


(a) $\mu^2 < \lambda^D$, we observe that the subspace angles between the Steklov-Helmholtz and Dirichlet-Laplace (d) eigenfunctions are not small enough, except on the boundary.

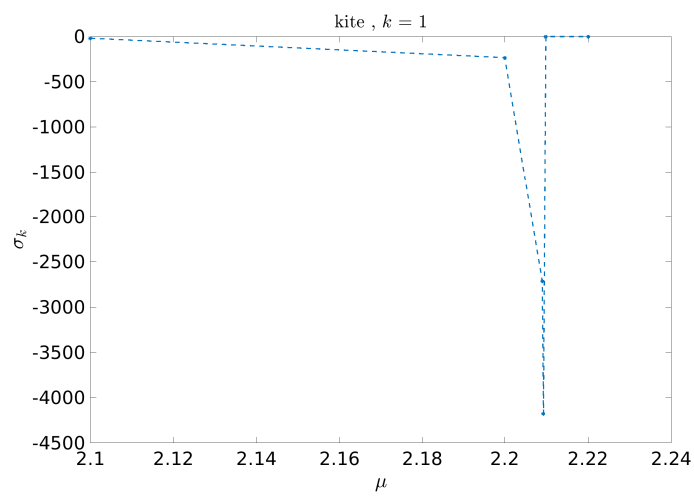


(c) $\mu^2 > \lambda^D$, we observe that the subspaces of Steklov-Helmholtz and Dirichlet-Laplace (d) eigenfunctions are perpendicular.

(b) $\mu^2 \approx \lambda^D$, we observe that the subspace angles between the Steklov-Helmholtz and Dirichlet-Laplace (d) eigenfunctions are small and note that $\sigma_1 \ll 0$.



(d) Laplace-Dirichlet eigenfunction. We compare with (a),(b),(c).

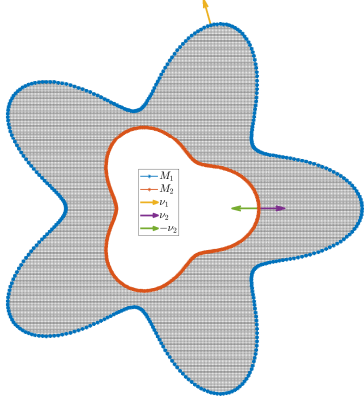


(e) σ_1 for wave numbers μ approaching μ_D and after μ_D . Observe that close to $\mu_D \approx 2.20986$ from the left, $\sigma_1 \rightarrow -\infty$.

Figure 3.11: Steklov-Helmholtz eigenpairs of the disk of the kite as $\mu^2 \rightarrow \lambda^D$. In subfigures (a)-(c) show Steklov-Helmholtz eigenfunctions and in (d) shows the Dirichlet-Laplace eigenfunction. In subfigure (e) shows σ_1 against μ .

3.3 The Steklov-Helmholtz problem on domains of genus 1

Recall the Steklov-Helmholtz problem (1.2) where we now consider Ω domains of genus 1. We define the boundary of Ω by $M = \cup_{i=1}^2 M_i$. In this setup, note that the outward normal on M_1 points in the opposite direction of the normal on M_2 . Problem (1.2) becomes to find: u, σ so that,



$$\begin{cases} -\Delta u - \mu^2 u = 0 & \text{in } \Omega, \\ \frac{\partial u}{\partial \nu_2} = \sigma \rho u & \text{on } M_2, \\ \frac{\partial u}{\partial \nu_1} = \sigma \rho u & \text{on } M_1. \end{cases} \quad (3.6)$$

As before, we set $\rho \equiv 1$ and recall Remark 2.4.2. In terms of our setup we have the boundary $M = M_1 \cup M_2$ with outer unit normals (yellow [ν_1] and purple [ν_2] arrows above). So when working on the inner boundary M_2 with normal derivatives, to point inward (green arrow $[-\nu_2]$) we have an extra negative sign. For $i = 1, 2$ with $x_i \in M_i$ and denoting $\nu_{x_i} := \nu_i$ the Steklov boundary condition gives,

$$\partial_{\nu_i} u = \tilde{\sigma} u \implies \sum_{j=1}^2 \int_{M_j} \partial_{\nu_{x_i}} G_\mu(x_i, y) \psi_j(y) \, ds_y + \frac{\psi_i(x_i)}{2} = \tilde{\sigma} \sum_{j=1}^2 \int_{M_j} G_\mu(x_i, y) \psi_j(y) \, ds_y.$$

Each boundary is discretized with $2N$ points. Fix $x_1 \in M_1$ and we have:

$$\begin{aligned} & \int_{M_1} \partial_{\nu_{x_1}} G_\mu(x_1, y) \psi_1(y) \, ds_y + \int_{M_2} \partial_{\nu_{x_1}} G_\mu(x_1, y) \psi_2(y) \, ds_y + \\ & \frac{\psi_1(x_1)}{2} = \tilde{\sigma} \left[\int_{M_1} G_\mu(x_1, y) \psi_1(y) \, ds_y + \int_{M_2} G_\mu(x_1, y) \psi_2(y) \, ds_y \right]. \end{aligned}$$

The first integral on the left (and right) relates every point on M_1 to fixed $x_1 \in M_1$. The second integral on the left (and right) relates every point on M_2 to fixed $x_1 \in M_1$. On discretizing similar to Chapter 2, we obtain the discretized operators corresponding to the single layer and adjoint of the double layer. For every $x_1 \in M_1$ we get one such equation and in total there are $2N$ equations. On the left we have the effect of the adjoint of the double layer and we denote the matrices like we did in Chapter 2. We denote the matrix relating the fixed point x_1 with every point on its

boundary M_1 (first integral on the left along with the density term) by $A_1 + Id$. We denote the matrix relating the fixed point x_1 with every point on the other boundary M_2 (first integral on the left along with the density term) by \tilde{A}_2 . Similarly on the right hand side we have the effect of the single layer and the corresponding matrices are denoted by B_1 and \tilde{B}_2 .

Exactly like this, we have another set of $2N$ equations for all x_2 fixed on M_2 . Writing the entire system of $4N$ equations we have the following generalized eigenvalue problem:

$$\begin{pmatrix} A_1 + Id & \tilde{A}_2 \\ -\tilde{A}_1 & -A_2 + Id \end{pmatrix} \begin{pmatrix} \psi_1 \\ \psi_2 \end{pmatrix} = \tilde{\sigma} \begin{pmatrix} B_1 & \tilde{B}_2 \\ \tilde{B}_1 & B_2 \end{pmatrix} \begin{pmatrix} \psi_1 \\ \psi_2 \end{pmatrix}. \quad (3.7)$$

Further, the matrices with superscript \sim have no singular behaviour since they denote the effect of the 2 boundaries on each other. For instance, consider $\tilde{A}_2 = \int_{M_1} \partial\nu_{x_1} G_\mu(x_1, y) \psi_2(y) ds_y$, where $x_1 \in M_1$ and $y \in M_2$ and so $G_\mu(x_1, y) \neq 0$. Therefore we can evaluate these integrals using the trapezoidal rule on the trigonometric polynomials of the integrands.

Remark 3.3.1 (Discretized layer potentials for domains of genus 1). *The $2N \times 2N$ matrix $A_1 + Id$ (B_1) in Equation 3.7 corresponds to the discretized adjoint of the double layer potential (single layer potential) which relates fixed points $x_1 \in M_1$ to every point on M_1 . The $2N \times 2N$ matrix \tilde{A}_2 (\tilde{B}_2) in Equation 3.7 corresponds to the discretized adjoint of the double layer potential (single layer potential) which relates fixed points $x_1 \in M_1$ to every point on M_2 . The $2N \times 2N$ matrix $-A_2 + Id$ (B_2) in Equation 3.7 corresponds to the discretized adjoint of the double layer potential (single layer potential) which relates fixed points $x_2 \in M_2$ to every point on M_1 . The $2N \times 2N$ matrix $-\tilde{A}_1$ (\tilde{B}_1) in Equation 3.7 corresponds to the discretized adjoint of the double layer potential (single layer potential) which relates fixed points $x_2 \in M_2$ to every point on M_2 .*

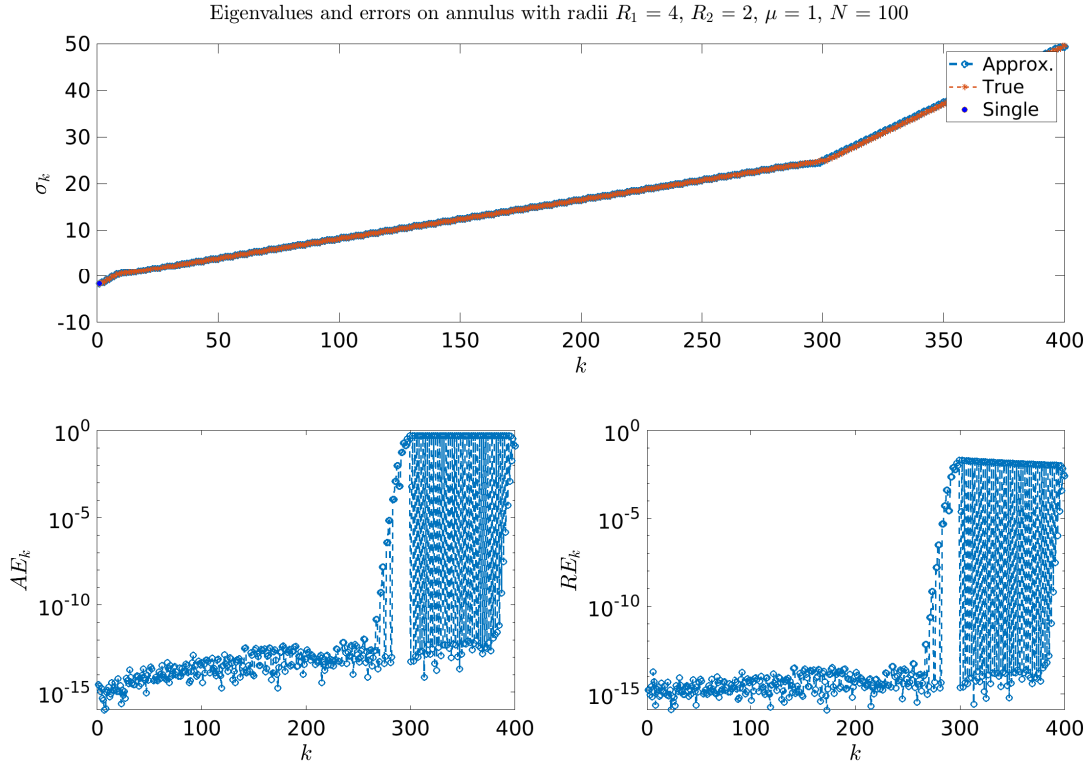
We can compute the exact eigenvalues if M_1 and M_2 are concentric circles with inner and outer radii $0 < R_2 \leq R_1$. Compared to a single disk (see Section 3.1.3), the radial part of the solution of the Helmholtz equation is modified to $c_1 J_n(\mu r) + c_2 Y_n(\mu r)$ for constants c_1, c_2 . We get the system,

$$\begin{pmatrix} \sigma_n J_n(\mu R_1) - \mu J'_n(\mu R_1) & \tilde{\sigma}_n Y_n(\mu R_1) - \mu Y'_n(\mu R_1) \\ \tilde{\sigma}_n J_n(\mu R_2) + \mu J'_n(\mu R_2) & \tilde{\sigma}_n Y_n(\mu R_2) + \mu Y'_n(\mu R_2) \end{pmatrix} \begin{pmatrix} c_1 \\ c_2 \end{pmatrix} = \begin{pmatrix} 0 \\ 0 \end{pmatrix}.$$

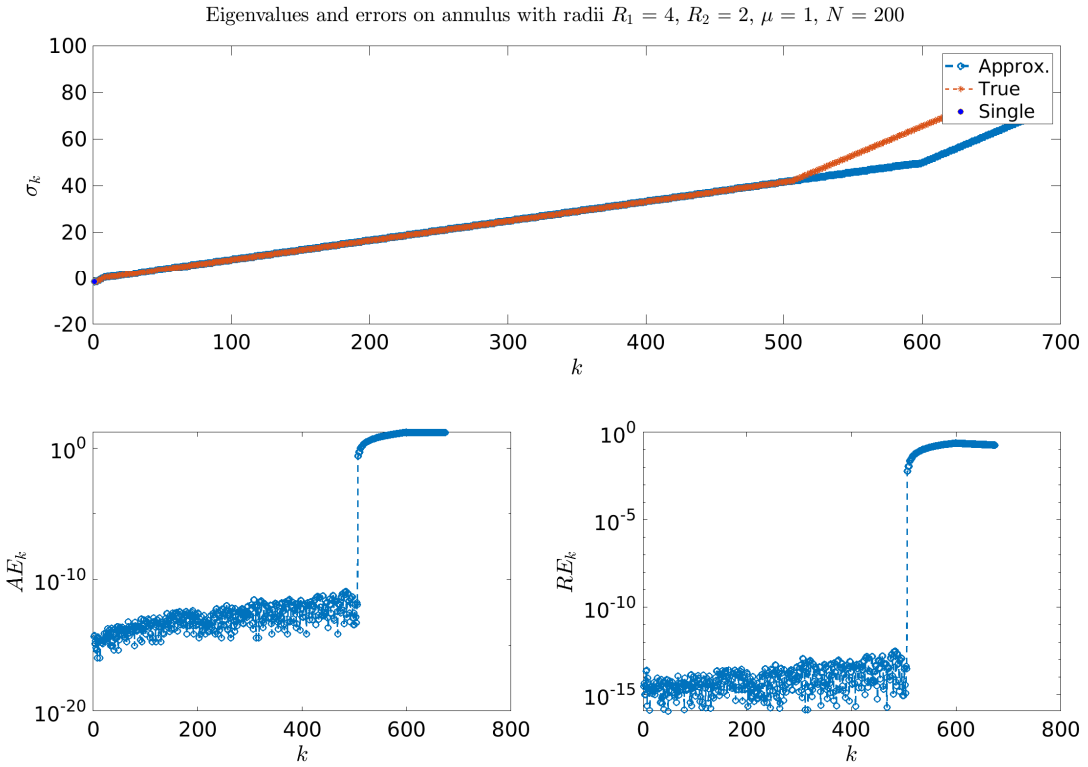
We set the determinant to zero solution and obtain a quadratic equation in $\tilde{\sigma}_n$,

$$\begin{pmatrix} J_n(\mu R_1)Y_n(\mu R_2) - J_n(\mu R_2)Y_n(\mu R_1) \\ \mu [J_n(\mu R_1)Y'_n(\mu R_2) - J'_n(\mu R_1)Y_n(\mu R_2) - J'_n(\mu R_2)Y_n(\mu R_1) + J_n(\mu R_2)Y'_n(\mu R_1)] \\ \mu^2 [-J'_n(\mu R_1)Y'_n(\mu R_2) + J'_n(\mu R_2)Y'_n(\mu R_1)] \end{pmatrix}^\top \begin{pmatrix} \tilde{\sigma}_n^2 \\ \tilde{\sigma}_n \\ 1 \end{pmatrix} = 0. \quad (3.8)$$

We recall [Remark 3.1.4](#) regarding the sorting of eigenvalues. As for the disk, on the annulus σ_0 is a single eigenvalue and the rest are double. In [Figure 3.12](#), we show the eigenvalues and AE_k , RE_k (see [Equation 3.2](#) and [Equation 3.3](#)) for an annulus of radii 2, 4 using two values of $N = 200, 400$. We observe that after a certain value of k , the eigenvalues *turn* for both the true and approximated eigenvalues. We note however that the errors are of the order of machine epsilon before the turn. Each subfigure has three plots over two rows. In the top row we show the true σ_k^{true} (red) and approximate σ_k (light blue) eigenvalues along with the eigenvalue of multiplicity one (blue). In the second row we show the errors AE_k (left) and errors RE_k (right).



(a) For $N = 100$, we are able to recover the first 200 eigenvalues with machine precision. We observe that the true eigenvalues *turn* around $k = 300$.



(b) For $N = 200$, we are able to recover the first 400 eigenvalues with machine precision. We observe that the true eigenvalues *turn* around $k = 500$.

Figure 3.12: Errors of the Steklov-Helmholtz eigenvalues for annulus of radii $R_1 = 2$ and $R_2 = 4$.

We investigate this curious *turning* behaviour of the eigenvalues. From [Equation 3.8](#) we note that the true eigenvalues of the annulus are combinations of the Bessel and Neumann functions. In [Remark 3.1.4](#) we have discussed that the Bessel function of order n is not the n th value when sorting Bessel functions in ascending order. In subfigures (a) and (b) above we compare the first $N_1 = 400$ and $N_2 = 700$ sorted eigenvalues respectively. When increasing from N_1 to N_2 we have $N_2 - N_1$ more eigenvalues. While sorting, some of the additional eigenvalues may be smaller than some of the first N_1 sorted eigenvalues. Further, as we take more grid points on the boundary M , we are able to resolve higher oscillatory behaviour of the eigenfunctions $e^{in\theta}$, which is not captured by the smaller number of grid points. We observe this behaviour in the turning in the figure above. The red curve is the curve of true eigenvalues and observe that even this curve *turns* at different values of k . In [Figure 3.13](#) we vary N from 50 to 250 with a step of 50 and plot the sorted $2N$ true eigenvalues. In this configuration, we can see that for $N = 200, 250$, the turning point does not move and is fixed near $k = 506$, which corresponds to a Bessel order of $n = 168$. Coefficients in [Equation 3.8](#) for Bessel order more than 168 are either $\pm \text{Inf}$ or NaN in MATLAB. In either case the turning seems to appear after $2N$ eigenvalues (we compute a total of $4N$) which we do not expect

to be recovered accurately anyway due to increasing approximation errors for higher eigenvalue numbers k . For the same configuration, since the turning of the true eigenvalues occurs at different values of k on increasing N , we conclude that it is an artifact arising possibly due to numerical errors for higher values of k .

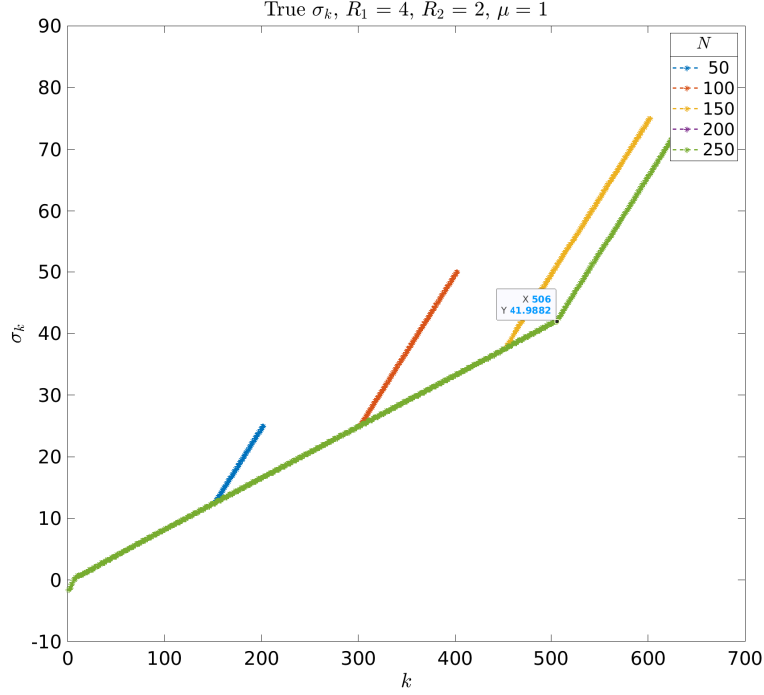


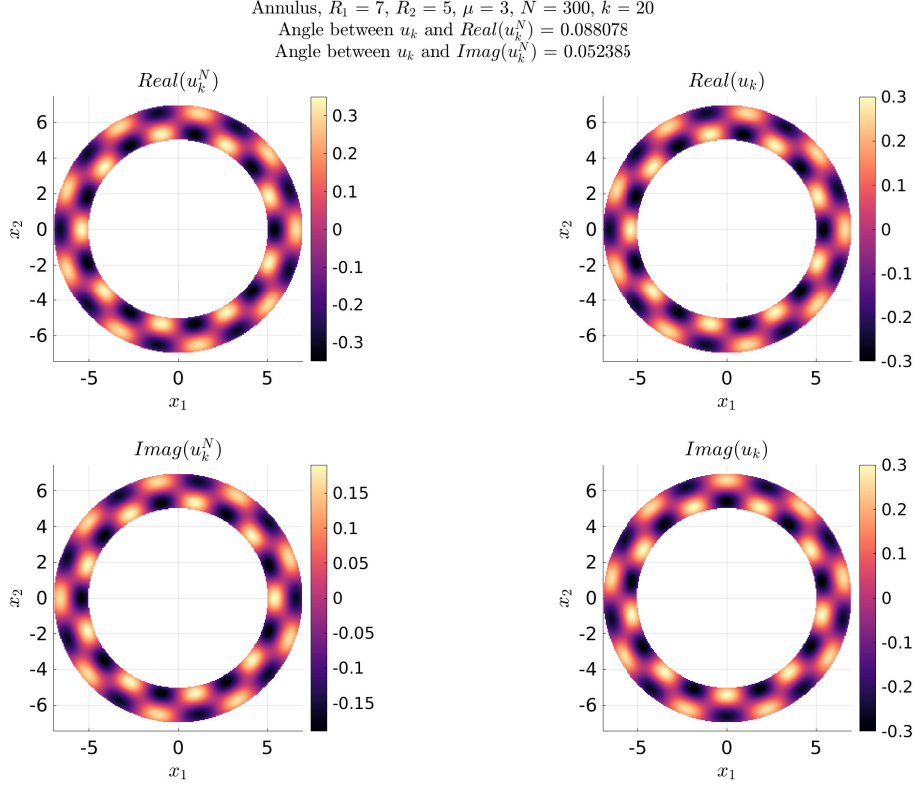
Figure 3.13: The true solution seems to turn at different points, till a certain value of N .

To construct the eigenfunctions, the idea is still to use the single layer potential as in [Equation 3.5](#). Since there are since boundary components M_1 and M_2 , we add the solutions to capture the effect of all boundary points on any given point inside Ω . So we have for $x_j \in \Omega$,

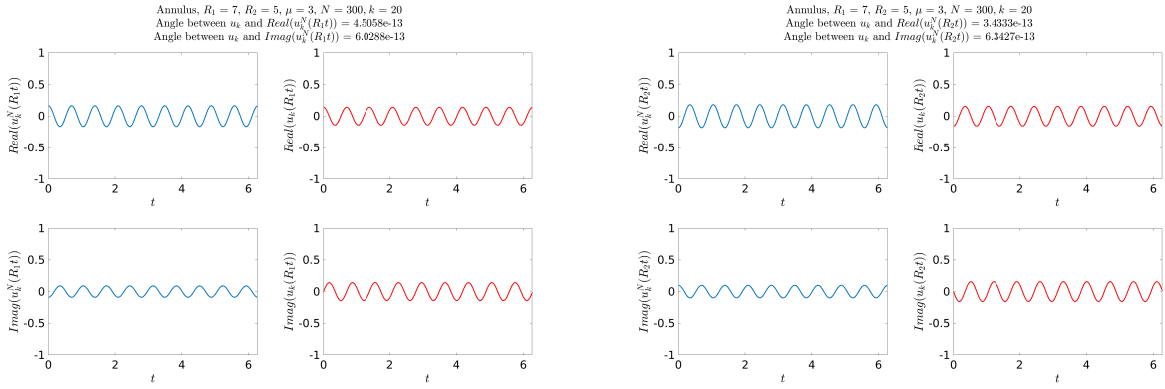
$$u_k(x_j) = \int_0^{2\pi} \frac{i}{4} H_0^1(\mu r(x_j, \tau)) \psi_{k,1}(\tau_1) |x'(\tau_1)| d\tau_1 + \int_0^{2\pi} \frac{i}{4} H_0^1(\mu r(x_j, \tau_2)) \psi_{k,2}(\tau_2) |x'(\tau_2)| d\tau_2, \text{ similarly } u_k^N(x_j), \quad (3.9)$$

where the first term corresponds to the outer boundary M_1 and the second term corresponds to the inner boundary M_2 (recall that $r(x, y)$ computes the Euclidean distance between $x, y \in \mathbb{R}^2$).

In [Figure 3.14](#) we show the eigenfunctions inside an annulus. There are three subfigures. Subfigure (a) shows the comparison of the eigenfunctions in Ω . Subfigures (b), (c) show the eigenfunctions on M_1 and M_2 respectively. We also report the subspace angles.



(a) The subspace angles between the true and computed eigenfunctions in Ω for $k = 20$ are small.



(b) The subspace angles between the true and computed eigenfunctions on M_1 for $k = 20$ are of machine precision.
 (c) The subspace angles between the true and computed eigenfunctions on M_2 for $k = 20$ are of machine precision.

Figure 3.14: Computed and expected eigenfunctions ($k = 20$) on M and inside an annular ring with outer radius 7 and inner radius 5, $\mu = 3$ and $N = 300$. Subfigure (a) compares the eigenfunctions inside Ω . Subfigures (b), (c) compare the eigenfunctions on M_1 , M_2 respectively. The titles contain the subspace angles in degrees.

3.4 Convergence tests on genus 0 and genus 1 domains

In this section we numerically test for convergence of the Steklov-Helmholtz eigenvalues of various curves of genus 0 (simply connected) and genus 1 (annular domains).

3.4.1 Experiments on genus 0 domains

The numerical scheme works for any boundary curve M that has a smooth 2π periodic parametrization. In this section we consider a subset of some suitable curves besides the disk (the full list with boundary parametrization is in [Appendix A](#)). For some of these curves in [Figure 3.15](#) we show the convergence of the eigenvalues with respect to those obtained for a *large* value of $N = 1024$. For each value of N we get $2N$ eigenvalues and we consider the smallest N eigenvalues to compute the discrete 2-norm of the relative errors, i.e. $\|RE\|_2$ (see [Equation 3.4](#)).

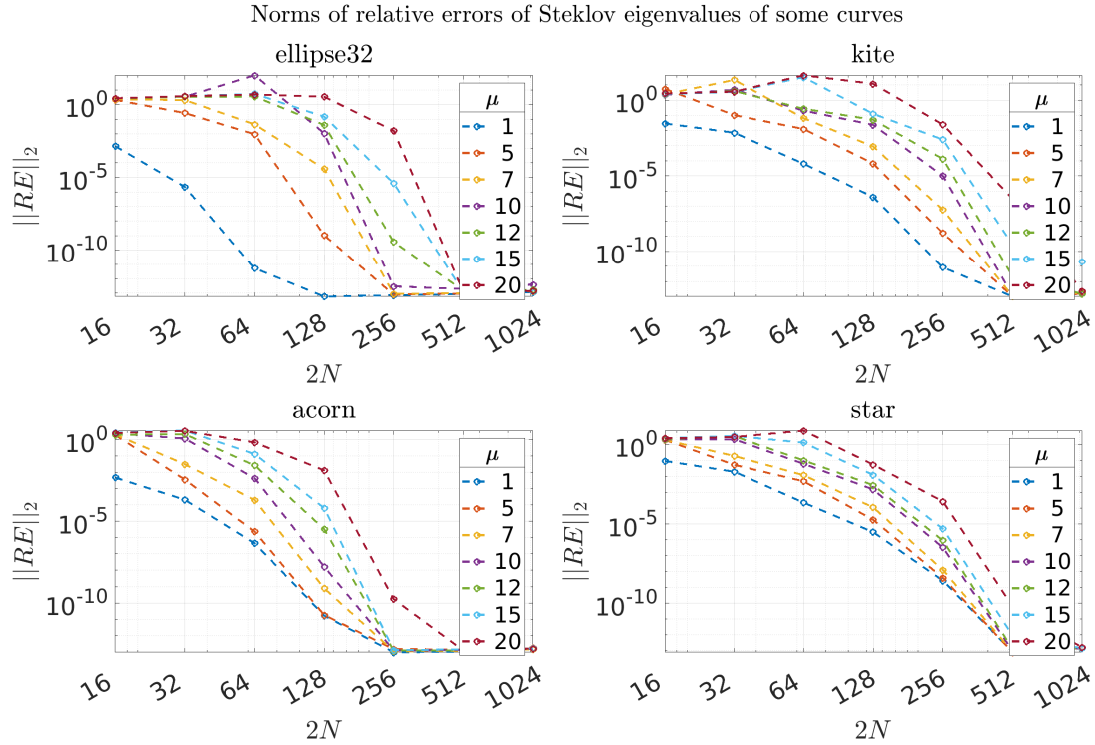


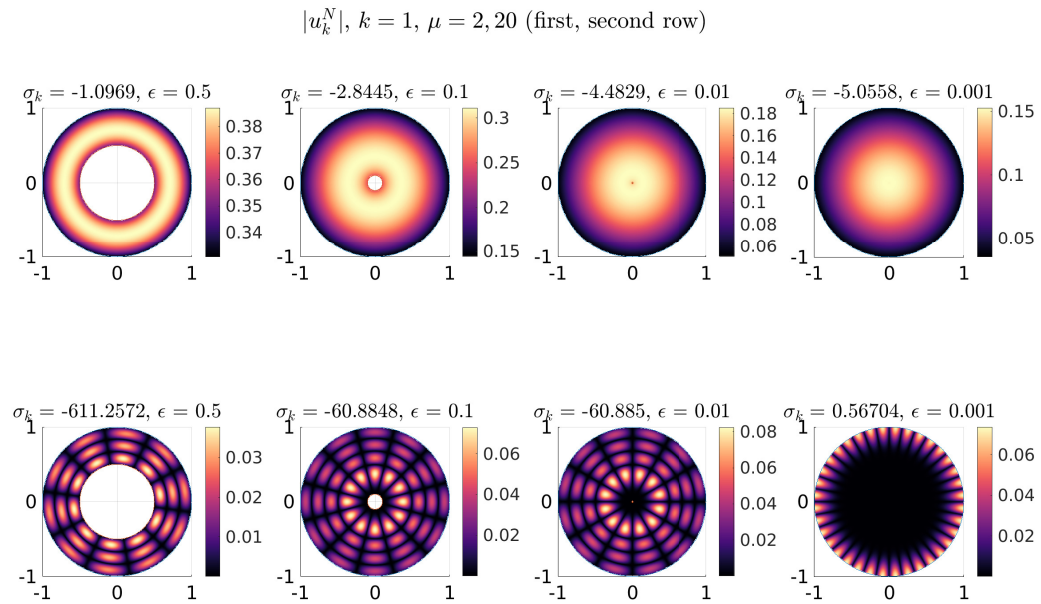
Figure 3.15: Convergence of Steklov-Helmholtz eigenvalues for some curves.

We observe exponential convergence of the eigenvalues to those at $2N = 2048$ for a few curves. As expected, when we increase μ more points are required.

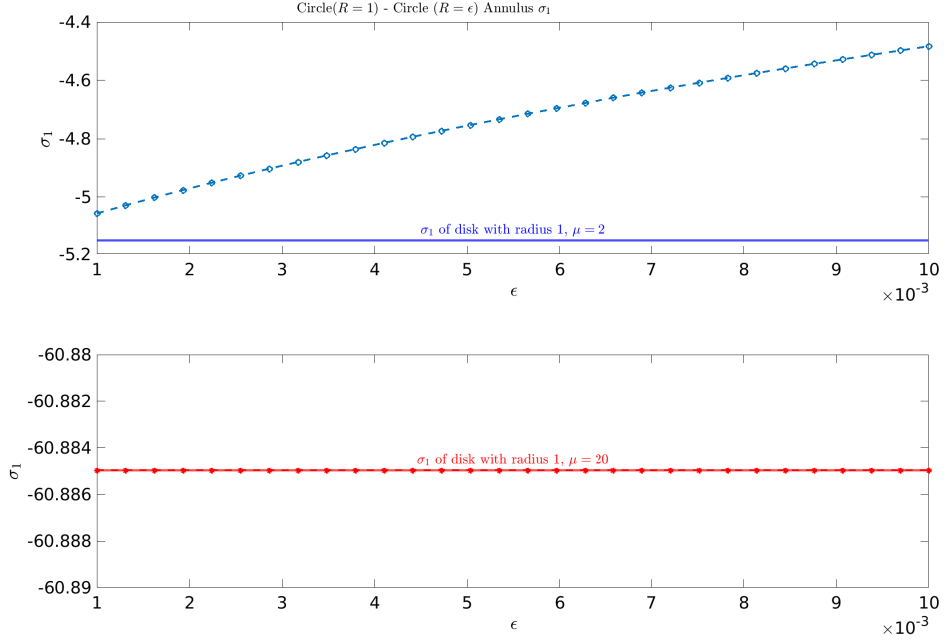
Remark 3.4.1 (Convergence of fewer eigenvalues). *We note that for smooth domains that have a sharp curvature in their parametrization, our method is unable to recover higher eigenvalues since the quadratures we use are not able to capture the singularities.*

3.4.2 Experiments on genus 1 domains

In this section, we primarily test what happens when the inner domain is shrunk to a point and show the behaviour in [Figure 3.16](#) and [Figure 3.17](#). We use ϵ as the scaling parameter for the inner domain. Each figure has two subfigures. Both subfigures have two rows corresponding to $\mu = 2$ (top) and $\mu = 20$ (bottom). Subfigures (a) show the absolute values of the corresponding eigenfunctions. Subfigures (b) show σ_1 against ϵ . The horizontal blue line is the first Steklov-Helmholtz eigenvalue of the outer domain alone for $\mu = 2$. The horizontal red line is the first Steklov-Helmholtz eigenvalue of the outer domain alone for $\mu = 20$. We note that as the inner domain shrinks, σ_1 of the annular domain approaches σ_1 of the outer domain.

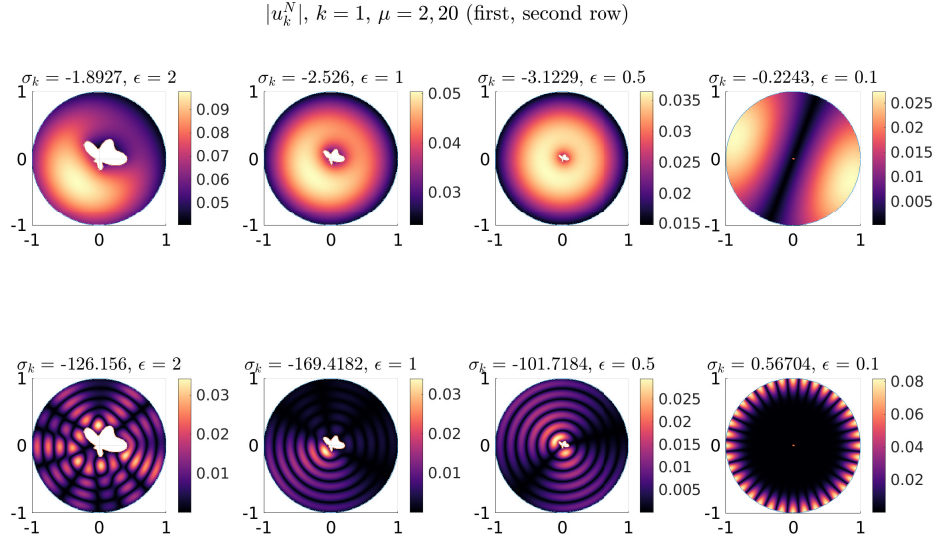


(a) Absolute values of the first eigenfunction for $\mu = 2$ (top), $\mu = 20$ (bottom).

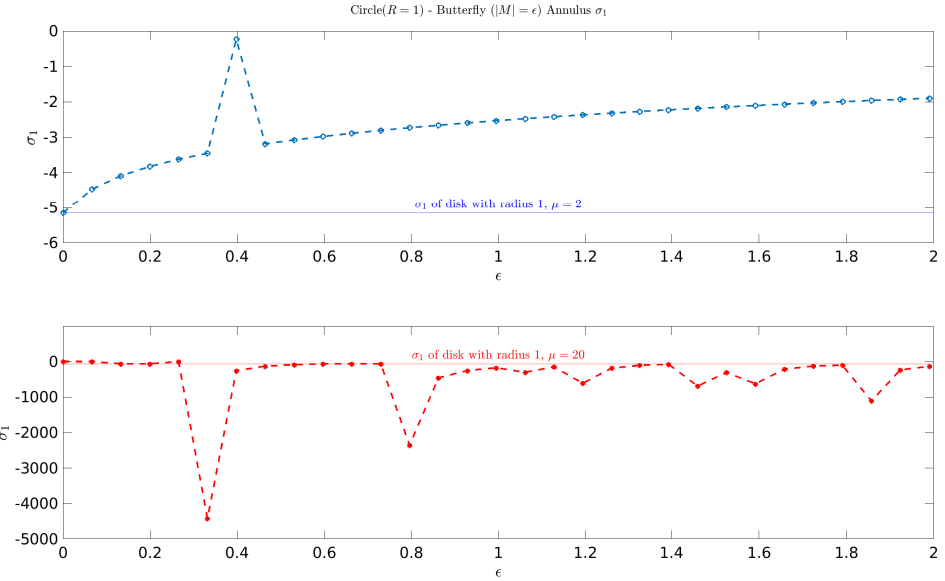


(b) σ_1 against ϵ . The horizontal lines are σ_1 for the unit disk.

Figure 3.16: We observe that the first eigenvalue of the annular domain (circle, circle) goes to σ_1 of the disk of radius 1. Subfigure (a) shows the absolute values of the eigenfunctions.. Subfigure (b) shows σ_1 . First row corresponds to $\mu = 2$, second row corresponds to $\mu = 20$. Horizontal blue line (top right) is σ_1 of the disk of radius 1. Horizontal red line (bottom right) is σ_1 of the disk of radius 1.



(a) Absolute values of the first eigenfunction for $\mu = 2$ (top), $\mu = 20$ (bottom).



(b) σ_1 against ϵ . The horizontal lines are σ_1 for the unit disk.

Figure 3.17: We observe that the first eigenvalue of the annular domain (circle, butterfly) goes to σ_1 of the disk of radius 1. Subfigure (a) shows the absolute values of the eigenfunctions. Subfigure (b) shows σ_1 . First row corresponds to $\mu = 2$, second row corresponds to $\mu = 20$. Horizontal blue line (top right) is σ_1 of the disk of radius 1. Horizontal red line (bottom right) is σ_1 of the disk of radius 1.

3.5 Negative eigenvalues and spectral asymptotics for domains of genus 0

In the preceding section, we saw convergence of the Steklov-Helmholtz eigenvalues for a variety of genus 0 and genus 1 domains. Therefore we can use the approximated spectrum to look for some of its own properties. In this section we perform some experiments which hint at a dependence of the Steklov-Helmholtz spectrum on the domain Ω and the wave number μ . Specifically we investigate a relation between the counting function

$$N(x) := N_{SH}(x) = \#\{k \in \mathbb{N}, \sigma_k \leq x\}, \quad (3.10)$$

and the spectral asymptotics of the Steklov-Helmholtz eigenvalue problem. From Theorem 7.4.17 in [LMP22], we have that $N(0) \geq 1$, i.e. the Steklov-Helmholtz eigenvalue problem has at least one negative eigenvalue. The proof follows by the use of the weak form of the DtN operator (equation 7.4.5 in [LMP22]) and choosing a function that solves the Helmholtz equation, $g = \exp(i\tilde{\mu} \cdot x)$, where $\tilde{\mu}, x \in \mathbb{R}^d$ and $|\tilde{\mu}|^2 = \mu^2$. We know that the Steklov-Laplace eigenvalues approach a line of slope $\pi/|M|$ as the eigenvalue number $k \rightarrow \infty$ (see equations (1.6) and (1.7)). Then in Section 1.4.2 we compared the Steklov eigenvalue problem for the Laplace and Helmholtz operators on the unit

disk. An important distinction between the two spectra is that at least one of the Steklov-Helmholtz eigenvalues is negative. We observed that as $k \rightarrow \infty$, the Steklov-Helmholtz eigenvalues approach the Steklov-Laplace eigenvalue. In [Section 3.5.1](#) we observe that $N(0)$ depends on $|M|$ and μ . Before moving on to the asymptotics, we establish a scaling property in [Section 3.5.2](#). Next, in [Section 3.5.3](#), we see that the Steklov-Helmholtz and Steklov-Laplace eigenvalues have the same asymptotic behaviour.

3.5.1 Number of negative Steklov-Helmholtz eigenvalues

In view of the counting function, we now consider $N(0)$. Our study begins with the circle and an idea to see whether it is possible to tell the “shape” (radius) of the circle from the spectrum. We fix the wave number μ and vary the radius R in [Figure 3.18](#). Then we fix R and vary μ in [Figure 3.19](#). In both these figures, we show the absolute eigenvalues $|\sigma_k|$ v/s k . We observe that the negative eigenvalues are sufficient to differentiate between different disk radii and wave numbers. So in [Figure 3.20](#) we plot heatmaps of the number of negative eigenvalues across various wave numbers μ and radii R . We observe that the number of negative eigenvalues is approximately the product μR , which we speculate translates to $\frac{|M|\mu}{2\pi}$ for curves in general (see [Figure 3.21](#)).

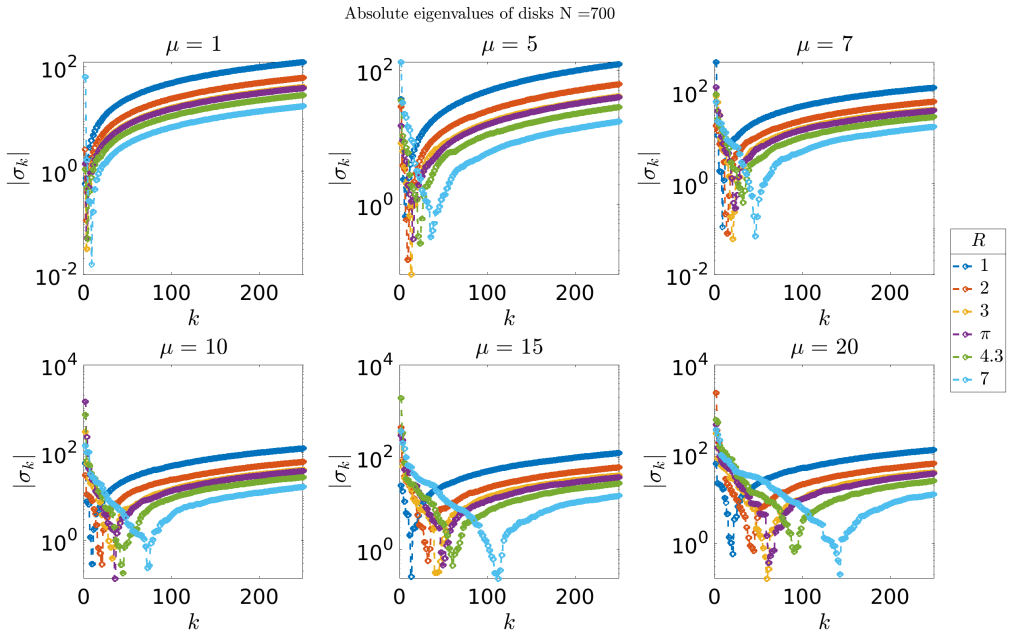


[Figure 3.18](#): Comparison of absolute eigenvalues $|\sigma_k|$ of disks of varying radii. In each subfigure μ is fixed and R varies. The eigenvalues across various radii exhibit similar behaviour later on in the spectrum.

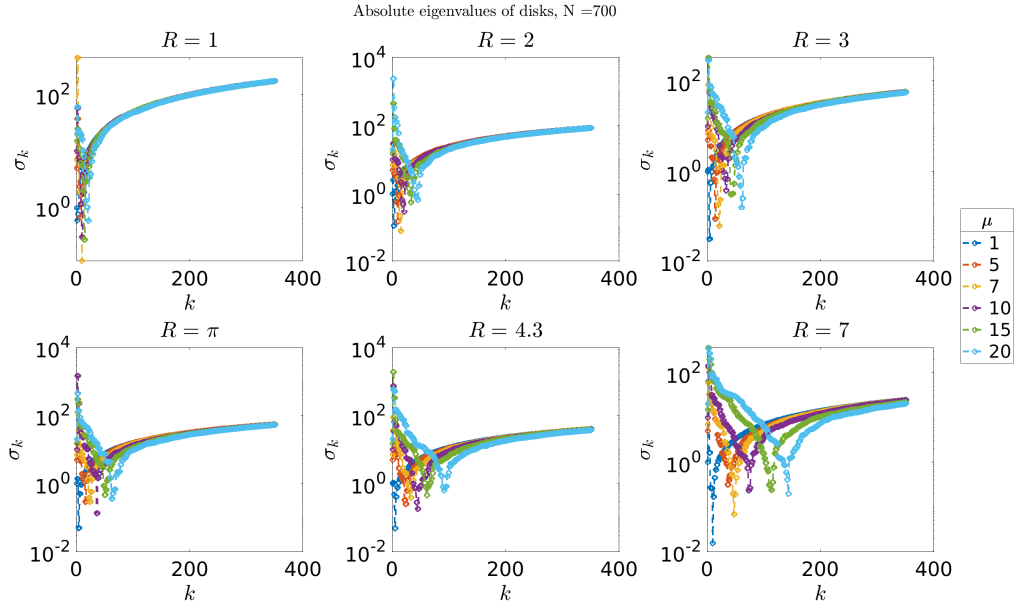


Figure 3.19: Comparison of absolute eigenvalues $|\sigma_k|$ of disks with varying μ . In each subfigure R is fixed and μ varies. The eigenvalues across various wave numbers exhibit similar behaviour later on in the spectrum.

Looking at the heat map below in Figure 3.20, we can see that the number of negative eigenvalues are almost μR . For curves other than the circle, we may have to consider the length of M i.e. $|M|$ or consider domain scaling.

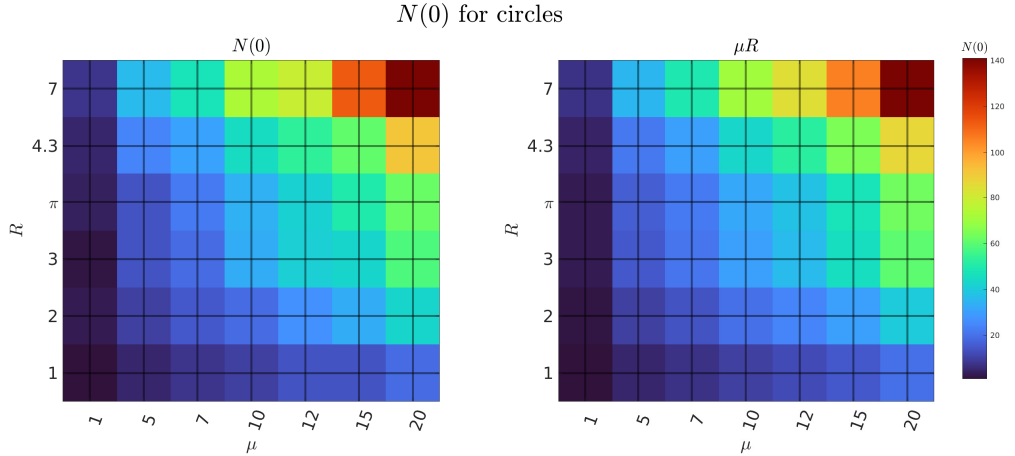


Figure 3.20: $N(0)$ for Steklov-Helmholtz eigenvalues. The figure shows heat maps of $N(0), \mu R$ for given μ, R . The two heatmaps are very similar, i.e. $N(0) \approx \mu R$.

We observe that $N(0) \approx \mu R$ for disks. We write $R = \frac{|M|}{2\pi}$ for a disk of radius R . So we check whether for a given domain with a perimeter of $|M|$ there is a similar dependence on $N(0)$. In figures we show heat maps of $N(0)$ for $|M|$ v/s μ across various curves in Figure 3.21 and Figure 3.22. Both

figures contain six heat maps. The first five subfigures correspond to the heat maps of the disk, ellipse, kite, acorn and star (see [Appendix A](#)). The sixth subfigure is a heat map for the value $\frac{|M|\mu}{2\pi}$. For [Figure 3.21](#) we take various values of $|M|$ in $[1, 20]$. For [Figure 3.22](#) we take various values of $|M|$ in $[1, 50]$. For both figures we set $\mu = 1, 5, 10, 15, 20$. We observe that for given perimeter $|M|$ and wave number μ , the number of negative eigenvalues $N(0)$ is approximately the same. As the product $|M|\mu$ increases, $N(0)$ gets closer to the speculated ratio $\frac{|M|\mu}{2\pi}$ which can be seen in [Figure 3.22](#).

We observe that for any given smooth and bounded domain Ω of fixed perimeter $|M|$, and wave number μ , the number of negative Steklov-Helmholtz eigenvalues $N(0) \approx \frac{|M|\mu}{2\pi}$.

As an interesting aside, a known relation between the counting functions of the Steklov-Helmholtz and Neumann and Dirichlet Laplace eigenvalues is $N_{SH}(0) = N_N(\mu^2) - N_D(\mu^2)$ (see Theorem 7.4.16 in [\[LMP22\]](#)).

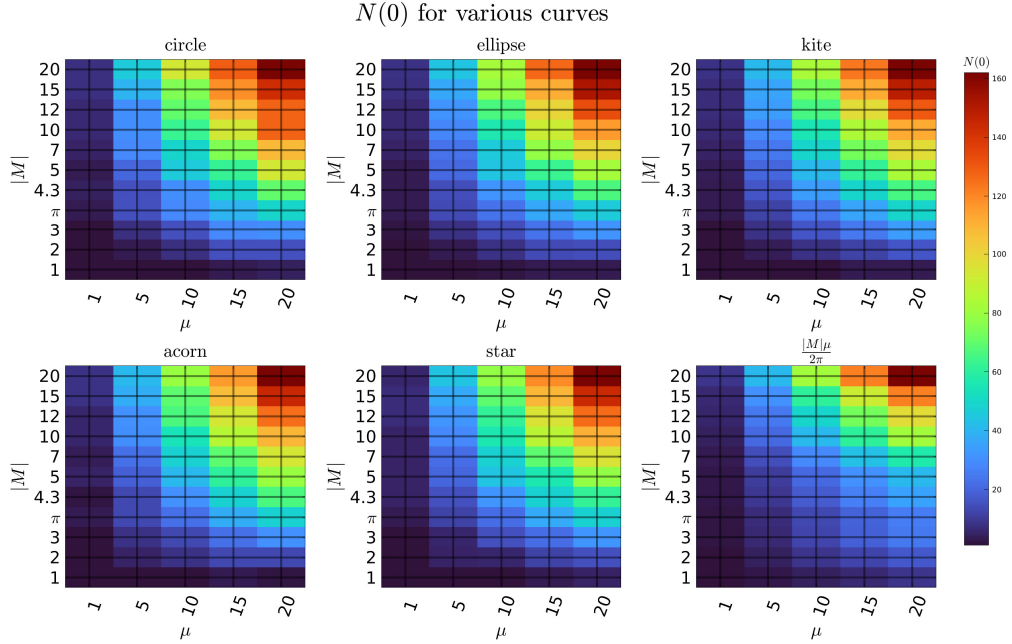


[Figure 3.21](#): Number of negative Steklov-Helmholtz eigenvalues across various curves. The first 5 subfigures are heat maps of $N(0)$ across some curves. The 6th heat map (bottom right) is of the value $|M|\mu/(2\pi)$. Here $|M|, \mu \in [1, 20]$.

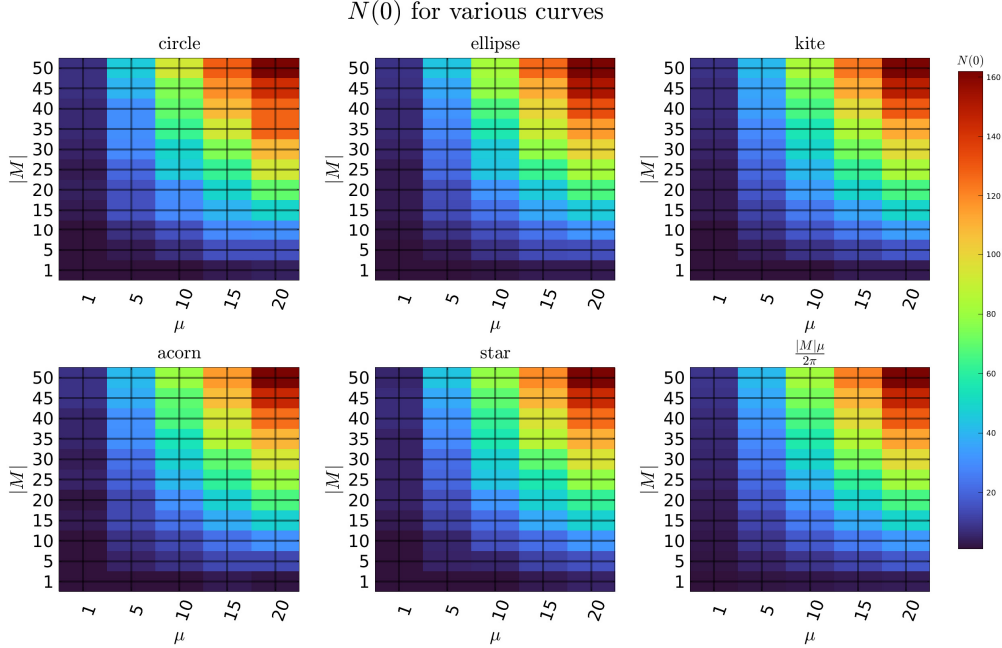
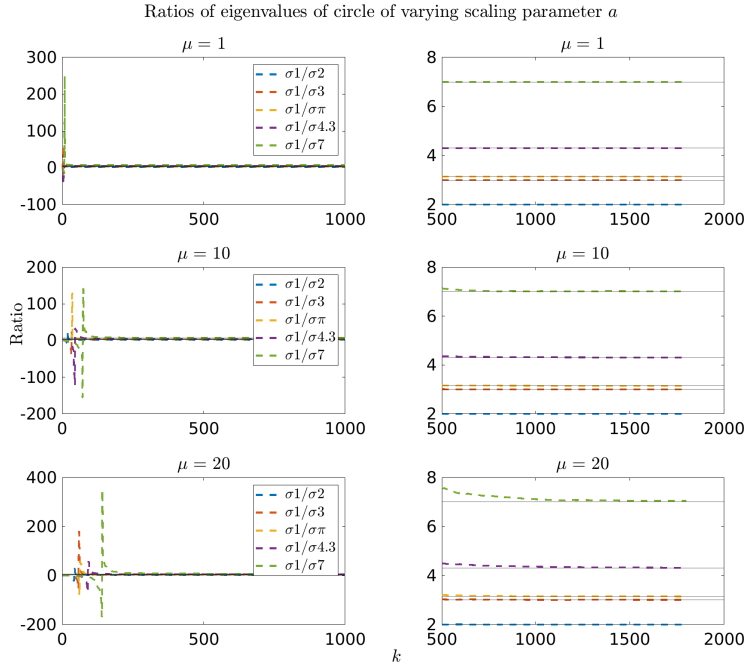


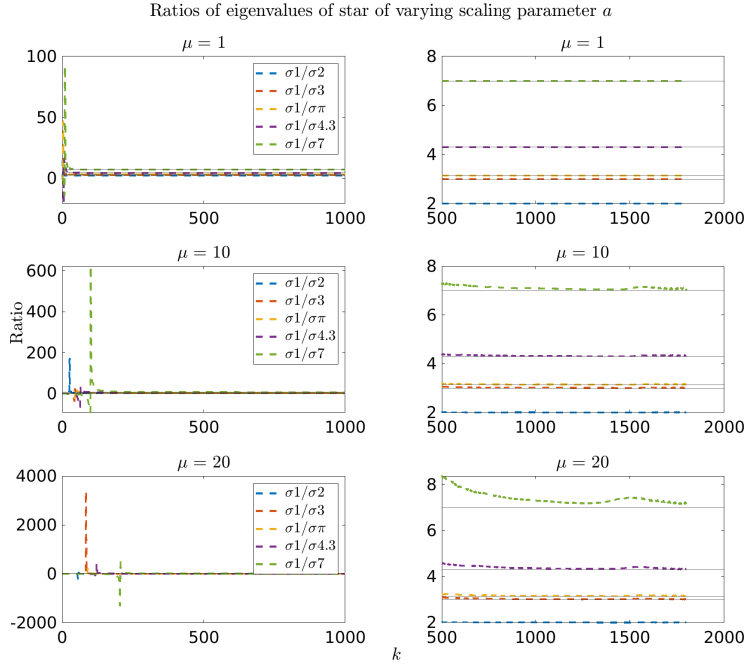
Figure 3.22: Number of negative Steklov-Helmholtz eigenvalues across various curves. The first 5 subfigures are heat maps of $N(0)$ across some curves for given $\mu, |M|$. The 6th heat map (bottom right) is of the value $|M|\mu/(2\pi)$ for given $\mu, |M|$. Here $|M| \in [1, 50]$, $\mu \in [1, 20]$.

3.5.2 Standard homothety of Steklov-Helmholtz eigenvalue problem and connection to the Robin-Laplacian

In Figure 3.23 we show the ratios of eigenvalues of scaled domains for disks and kites. Now in Figure 3.23(a) we look at the ratios of the eigenvalues $\sigma_k(\Omega)$ of the unit disk Ω with the other disks i.e. $\frac{\sigma_k(\Omega)}{\sigma_k(\Omega_R)}$, where Ω is the unit disk and Ω_R is a disk of radius R . We observe that the ratios of the first *few* (the meaning of *few* depends on μ and R) eigenvalues does not relate to the radius R . As we go further into the spectrum, the ratio approaches R . Note that as μ increases we need to go farther into the spectrum. We denote $\sigma_1/\sigma_2 := \frac{\sigma_k(\Omega)}{\sigma_k(\Omega_2)}$, $\sigma_1/\sigma_3 := \frac{\sigma_k(\Omega)}{\sigma_k(\Omega_3)}$ and so on. So the homothetic property of Steklov-Laplace eigenvalues (see Equation 3.13) does not hold and we need to establish what the standard homothety is for the Steklov-Helmholtz eigenvalues. Similar behaviour is exhibited by other curves and for reference we show the ratios for the kite (see Appendix A) in Figure 3.18(b).



(a) $\sigma a := \{\sigma_k(\Omega_a)\}$, where Ω_a is the disk of radius a .



(b) $\sigma a := \{\sigma_k(\Omega_a)\}$, where Ω_a is the kite scaled by a factor of a .

Figure 3.23: Ratios of Steklov-Helmholtz eigenvalues of original domain over Steklov-Helmholtz eigenvalues of scaled domains. In each subfigure every row corresponds to the same wave number μ and shows the first 1000 eigenvalue ratios on the left panel and eigenvalue ratios (500-1700) on the right panel. The horizontal lines in the plots above are the scaling parameters $a > 0$.

We now investigate this in detail.

Lemma 3.5.1. *Let $\sigma_k(\Omega, \mu)$ be the Steklov-Helmholtz eigenvalues for $\Omega \subset \mathbb{R}^d$ (Ω closed and bounded) with wave number μ and consider the scaled domain $a\Omega = \{x : x/a \in \Omega\}$. Then the Steklov-Helmholtz eigenvalues share the scaling property with the Robin eigenvalue problem (equation 4.9 in [BFK17]) and in particular we have*

$$\sigma_k(a\Omega, \mu) = \frac{\sigma_k(\Omega, a\mu)}{a}. \quad (3.11)$$

Proof. Consider the domain $a\Omega = \{x \in a\Omega : x/a \in \Omega, a > 0\}$ and the variational formulation of $\sigma_k^{a\Omega}$ given by the Rayleigh quotient,

$$\sigma_k(a\Omega, \mu) = \min_{\substack{v \in \mathcal{H}_\mu(a\Omega) \\ v \neq 0}} \left\{ \frac{\|\nabla v\|_{a\Omega}^2 - \mu^2 \|v\|_{a\Omega}^2}{\|v\|_{aM}^2}, v \perp \text{first } k-1 \text{ eigenfunctions on } M \right\}.$$

To relate the objective function to Ω , a natural change of variables is $z = \frac{x}{a}$, with $\partial_{x_k} v = \partial_{z_k} v / a$, $\partial_{x_k} z_k = a \partial_{z_k} v$ and $dx_k = a dz_k$, where $k = 1, \dots, d$ and d is the number of dimensions. This gives

$$\frac{\|\nabla v\|_{a\Omega}^2 - \mu^2 \|v\|_{a\Omega}^2}{\|v\|_{aM}^2} = \frac{a^{d-2} \|\nabla v\|_\Omega^2 - a^d \mu^2 \|v\|_\Omega^2}{a^{d-1} \|v\|_M^2} = \frac{\|\nabla v\|_\Omega^2 - a^2 \mu^2 \|v\|_\Omega^2}{a \|v\|_M^2}. \quad (3.12)$$

Consider now the Helmholtz equation, $\Delta u + a^2 \mu^2 u = 0$ with the Steklov boundary condition. Then Equation 3.12 becomes $\frac{\|\nabla v\|_\Omega^2 - a^2 \mu^2 \|v\|_\Omega^2}{\|v\|_M^2}$. This proves the lemma. \square

Note that if $\mu = 0$, we get back the Laplacian and its homothetic property for the Steklov-Laplace eigenvalues, i.e.

$$\sigma_k(a\Omega, 0) = \frac{\sigma_k(\Omega, 0)}{a}. \quad (3.13)$$

This is the standard homothety property of the Steklov-Laplace eigenvalues. On scaling the domain by a factor of a , the Steklov-Laplace eigenvalues also scale by the same factor a . In contrast, the Steklov-Helmholtz eigenvalues do not scale by a . We show the homothety property Equation 3.11 of the Steklov-Helmholtz eigenvalues in Figure 3.24. We consider the butterfly (see Appendix A) and note the scaling ratio to hold for all eigenvalues.

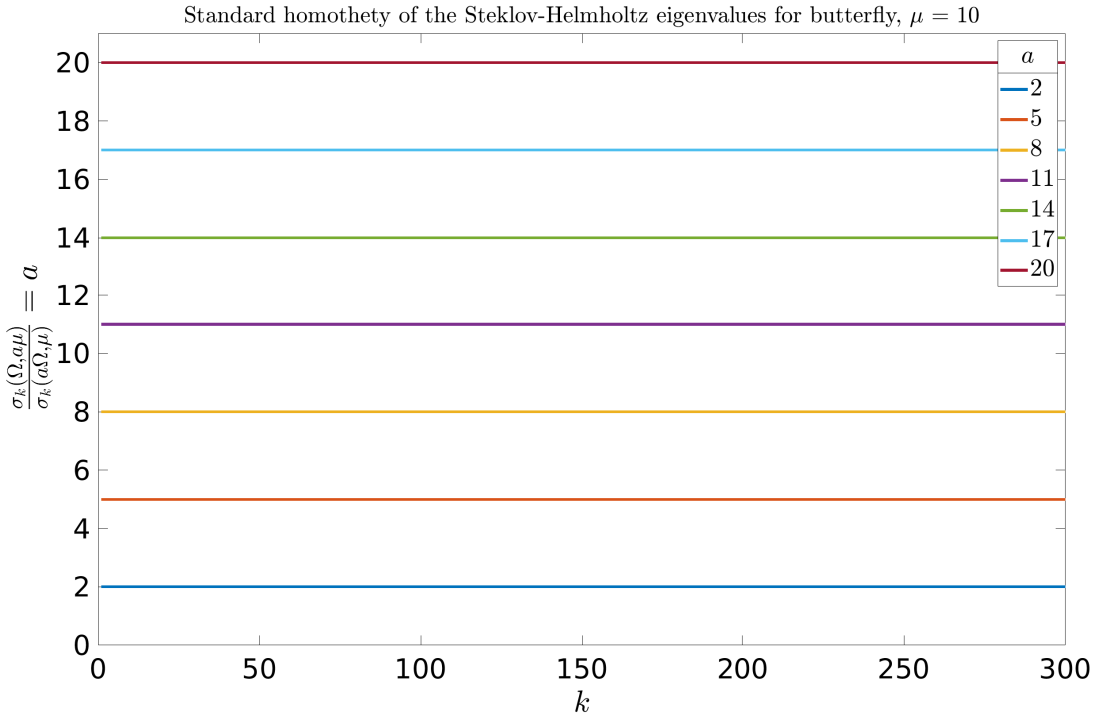


Figure 3.24: Homothetic property (3.11) for the Steklov-Helmholtz eigenvalues, where Ω is the butterfly and $\mu = 10$.

Now we explore the reciprocity of the Steklov-Helmholtz and Robin-Laplace eigenvalues as stated in proposition 7.4.4 of [LMP22] which states that μ^2 is an eigenvalue of the Robin-Laplacian if and only if σ is an eigenvalue of the Steklov-Helmholtz problem. Recall Equation 1.24 for the Steklov-helmholtz eigenvalue problem where we solved for σ to obtain Equation 1.25 and consider boundary weight $\rho \equiv 1$. For the Robin problem, in Equation 1.24 we have to solve for μ^2 instead and on rearranging we get in comparison with Equation 1.25,

$$\mu^2 = \frac{\|\nabla U\|_{L^2(\Omega)}^2 - \sigma \|TU\|_{L^2(M)}^2}{\|U\|_{L^2(\Omega)}^2}, \quad (3.14)$$

$$\sigma = \frac{\|\nabla U\|_{L^2(\Omega)}^2 - \mu^2 \|U\|_{L^2(\Omega)}^2}{\|TU\|_{L^2(M)}^2}. \quad (1.25)$$

We consider the cavity domain and set $\sigma = -1$. Using Algorithm 1, the first two eigenvalues that we locate correspond with $\mu \approx 1.96702$ and 2.41355 . Then, we set $\mu = 1.96702$ and compute the Steklov-Helmholtz eigenvalues. We observe for the first eigenvalue that $|\sigma_1 - (-1)| = 5.8894e - 07$. Next we set $\mu = 2.41355$ and compute the Steklov-Helmholtz eigenvalues. For the next eigenvalue we compute $|\sigma_2 - (-1)| = 3.6263e - 06$.

Remark 3.5.1. We observe that the Robin-Laplace and Steklov-Helmholtz eigenvalue reciprocity holds with respect to the eigenvalue number.

3.5.3 Asymptotic behaviour of Steklov-Helmholtz eigenvalues

We take disks of perimeters 1, 2, 3 along with wave numbers $\mu = 1, 5, 10$. We check what happens when we scale the eigenvalues by a factor $a = |M|$ and in Figure 3.25 we observe that not scaling with $|M|$ clearly separates eigenvalues according to perimeter whereas scaling makes the asymptotic behaviour of the eigenvalues very similar. We can see that for fixed perimeter, the μ curves are different from each other very early in the spectrum.

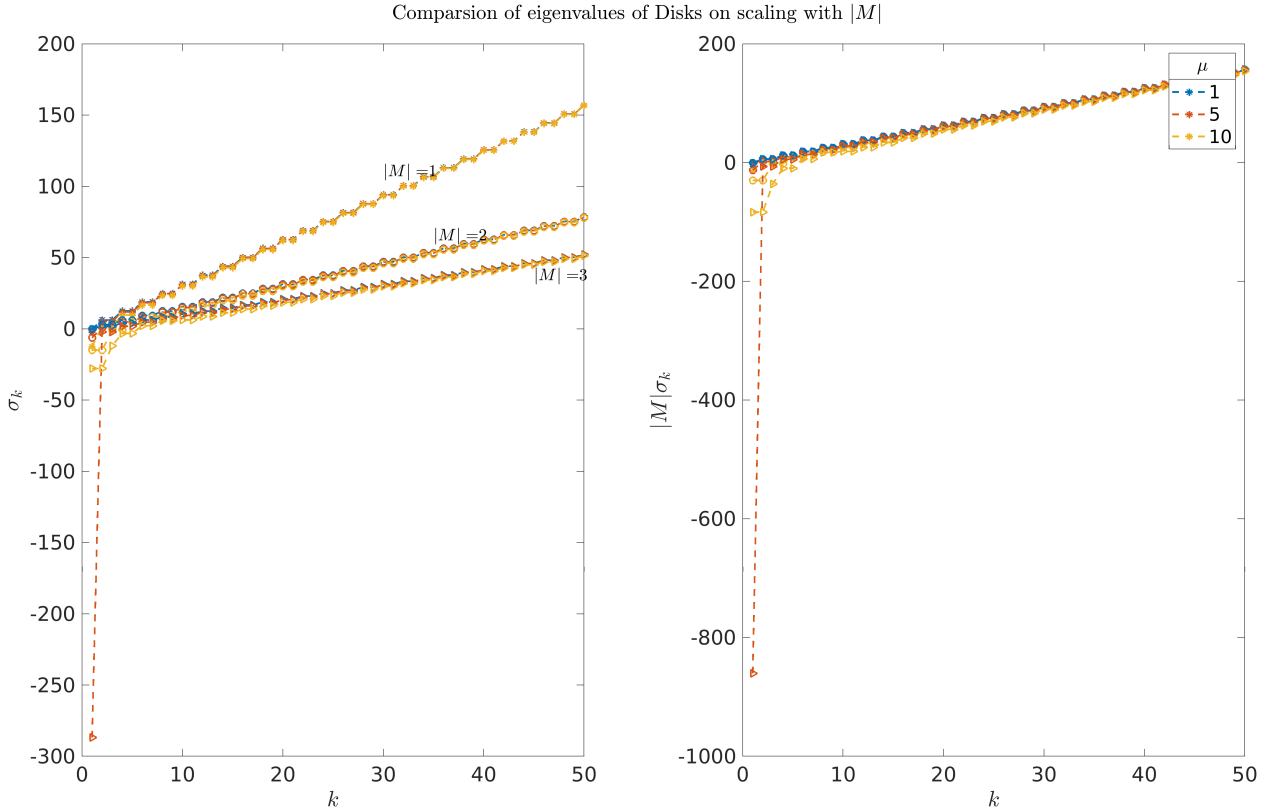


Figure 3.25: Comparison of scaling $\sigma_k(\Omega)$ with $|M|$ for disks. The Steklov-Helmholtz eigenvalues for $\mu = 1, 5, 10$ and lengths $|M| = 1, 2, 3$ are shown on the left. On the right, The Steklov-Helmholtz eigenvalues scaled by $|M| = 1, 2, 3$ are shown for $\mu = 1, 2, 3$.

Now we attempt to fit to Steklov-Helmholtz eigenvalues functions of type $\sigma_k(\Omega) \approx A_{\mu,|M|}k + B_{\mu,|M|}\sqrt{k} + \frac{C_{\mu,|M|}}{\sqrt{k}} + D_{\mu,|M|}$. We document the coefficient values in Tables 3.4 - 3.7.

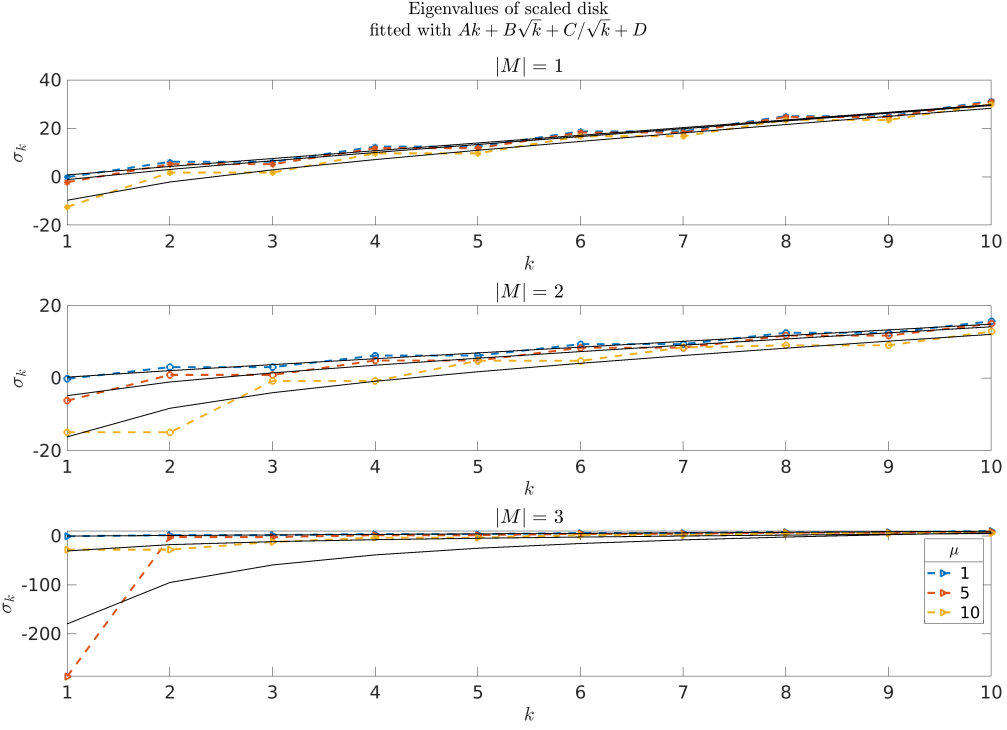


Figure 3.26: Fits of the type $\sigma_k(\Omega) \approx A_{\mu,|M|}k + B_{\mu,|M|}\sqrt{k} + \frac{C_{\mu,|M|}}{\sqrt{k}} + D_{\mu,|M|}$ for disks of perimeter $|M| = 1, 2, 3$ and $\mu = 1, 5, 10$.

	$\mu = 1$	$\mu = 5$	$\mu = 10$
$ M = 1$	3.1454	3.1474	3.1629
$ M = 2$	1.5728	1.5815	1.5919
$ M = 3$	1.0487	1.7800	1.0945

Table 3.4: Coefficients $A_{\mu,|M|}$ of k for disks

	$\mu = 1$	$\mu = 5$	$\mu = 10$
$ M = 1$	-0.0952	-0.1550	-0.5951
$ M = 2$	-0.0507	-0.2975	-0.6220
$ M = 3$	-0.0375	-19.3648	-1.3707

Table 3.5: Coefficients $B_{\mu,|M|}$ of \sqrt{k} for disks

	$\mu = 1$	$\mu = 5$	$\mu = 10$
$ M = 1$	-1.3384	-3.8154	-15.8091
$ M = 2$	-0.8132	-7.9045	-22.3419
$ M = 3$	-0.7064	-310.1316	-42.1684

Table 3.6: Coefficients $C_{\mu,|M|}$ of $1/\sqrt{k}$ for disks

	$\mu = 1$	$\mu = 5$	$\mu = 10$
$ M = 1$	-0.8843	-0.2744	3.6138
$ M = 2$	-0.4089	1.8069	5.2060
$ M = 3$	-0.2338	148.3093	12.1082

Table 3.7: Coefficients $D_{\mu,|M|}$ of k^0 for disks

We observe that the coefficient $A_{\mu,|M|} \lesssim \frac{\pi}{|M|}$. Further, at $|M| = 3, \mu = 5$ we see that the coefficients for σ_1 have higher magnitude compared to the other coefficient values. For wave number $\mu \approx 5.0367$, $\lambda^D = \mu^2$ is a Dirichlet eigenvalue of the Laplacian for a disk of radius $3/(2\pi)$, see [Section 3.1.2](#) and [Section 3.2](#). So this configuration ($|M| = 3, \mu = 5$) is such that $\mu^2 = 25$ is approximately a

Dirichlet eigenvalue is not helpful and we omit it. Similar to the disk, in Figure 3.27 we try fits of the type $\sigma_k(\Omega) \approx A_{\mu,|M|}k + B_{\mu,|M|}\sqrt{k} + \frac{C_{\mu,|M|}}{\sqrt{k}} + D_{\mu,|M|}$ on the ellipse (left) and cavity (right) (see Appendix A).

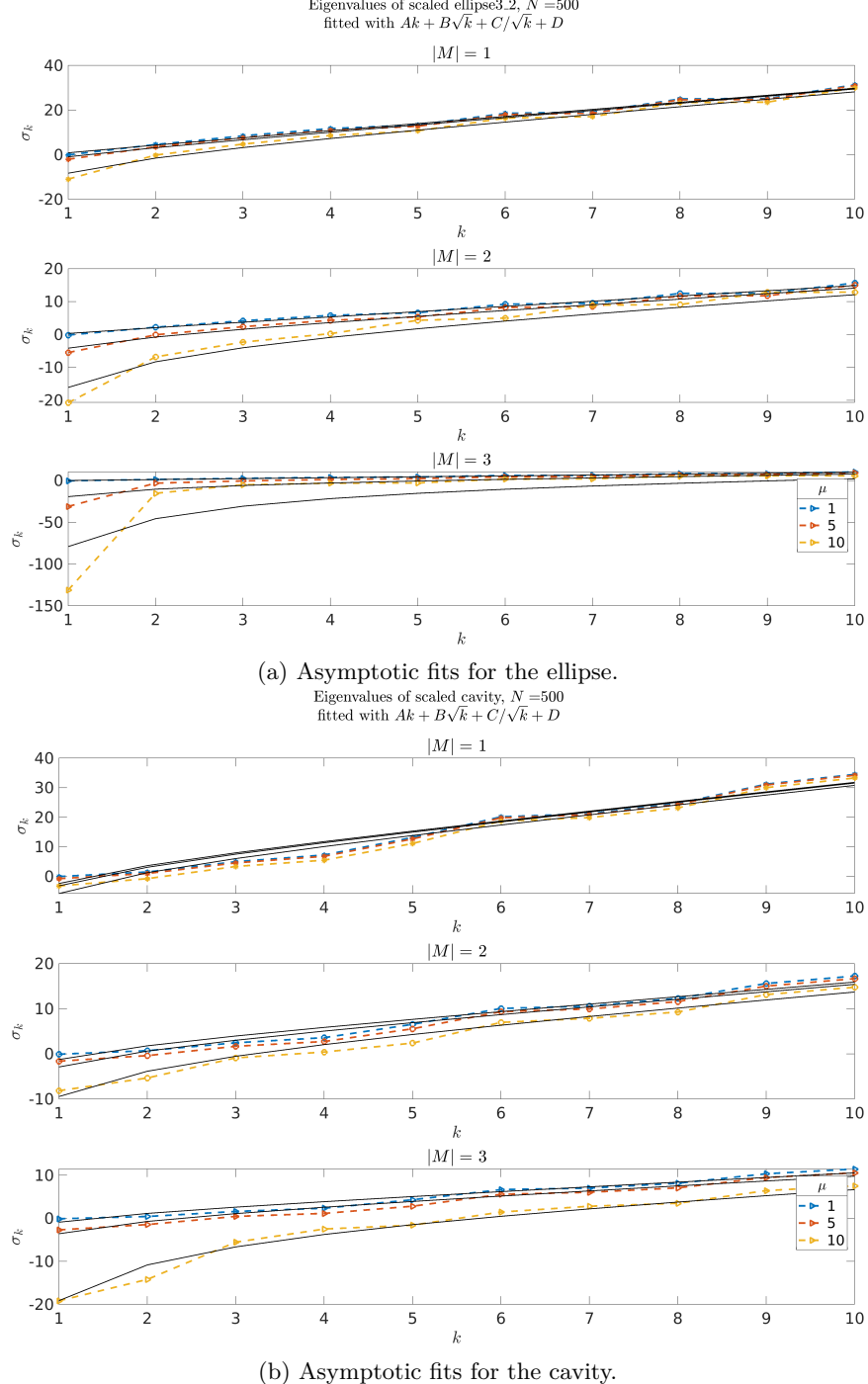


Figure 3.27: Fits of the type $\sigma_k(\Omega) \approx A_{\mu,|M|}k + B_{\mu,|M|}\sqrt{k} + \frac{C_{\mu,|M|}}{\sqrt{k}} + D_{\mu,|M|}$ for the ellipse (left) and cavity (right). Perimeters $|M| = 1, 2, 3$ and $\mu = 1, 5, 10$.

We observe again that the $A_{\mu,|M|}$ s are approximately $\pi/|M|$. Next, we show the first 50 Steklov-Helmholtz eigenvalues in figures 3.28 and 3.29. We consider some domains of perimeter $|M| = 1$ across various wave numbers μ .

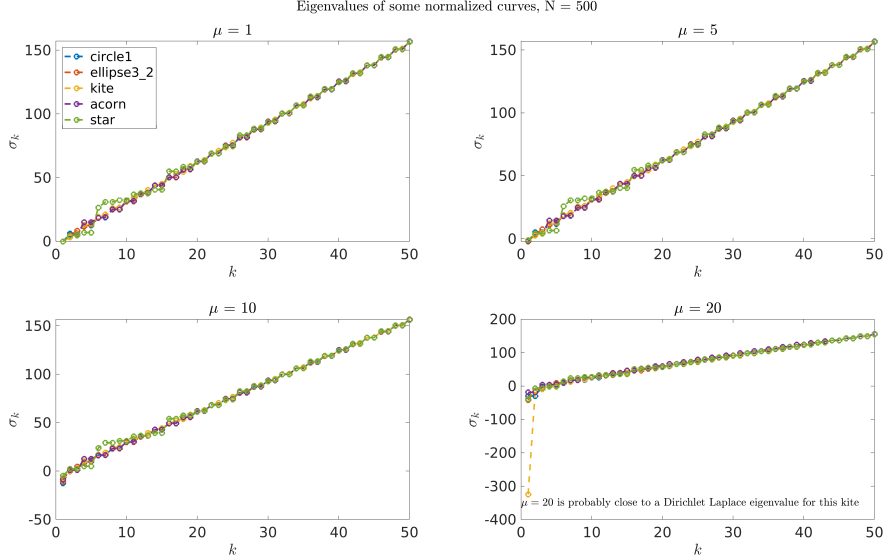


Figure 3.28: First 50 Steklov-Helmholtz eigenvalues $\{\sigma_k\}$ of some curves of length 1. In each figure the wave number μ is fixed and we consider the disk, ellipse, kite, acorn and star.

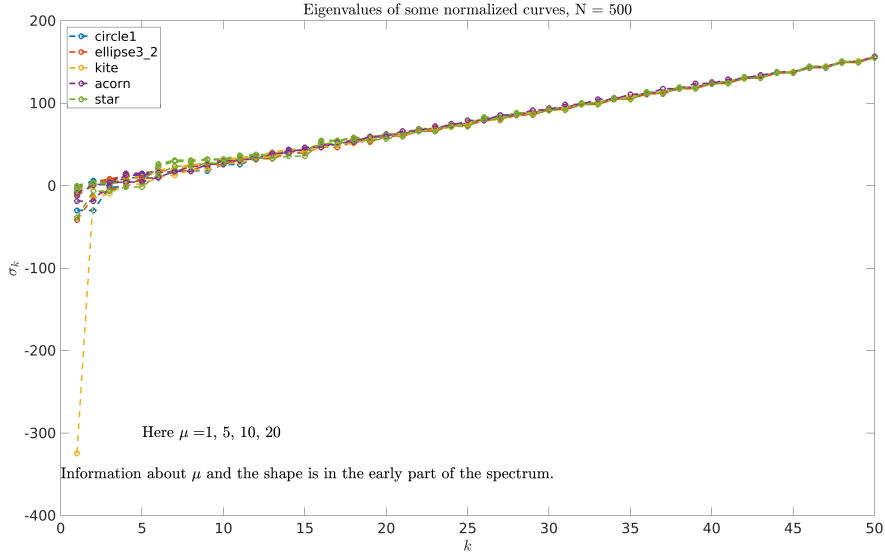


Figure 3.29: Plots in figure 3.28 superimposed on each other.

In Figure 3.28 and Figure 3.29 we observe bunching of eigenvalues after a certain number. For a fixed wave number μ , the early part of the spectrum may be able to differentiate between shapes. Changing μ does not affect bunching later on. As speculated, it is possible that the early part of the spectrum holds vital information about geometry and the wave number μ . We now keep $\mu = 15$

fixed and consider the first 100 Steklov-Helmholtz eigenvalues. In [Figure 3.30](#) on the left we show the first 100 $\{\sigma_k\}$ for the unit disk, ellipse, kite, acorn and star. On the right, we show the first 100 $\{\sigma_k\}$ for unit perimeter disk, ellipse, kite, acorn and star (see [Appendix A](#)).

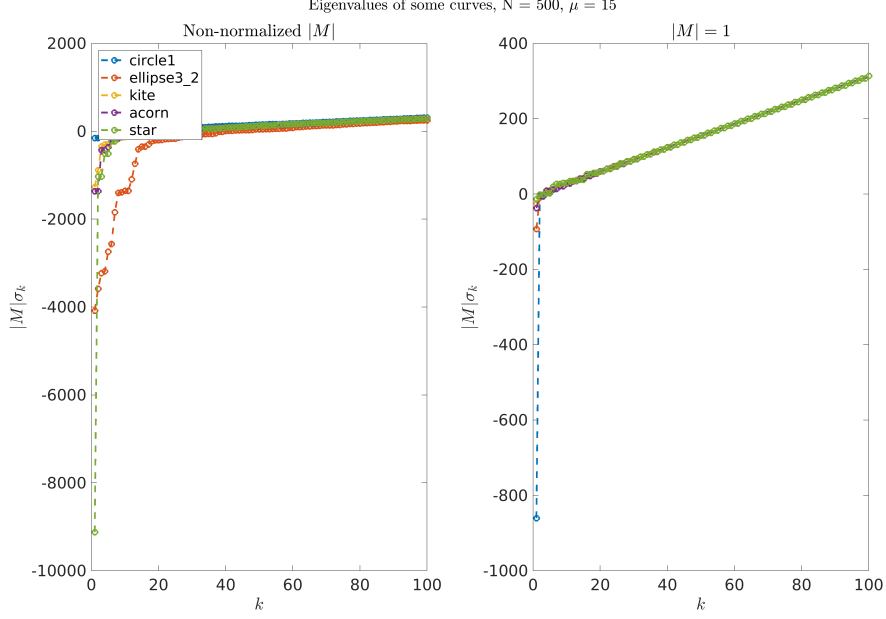
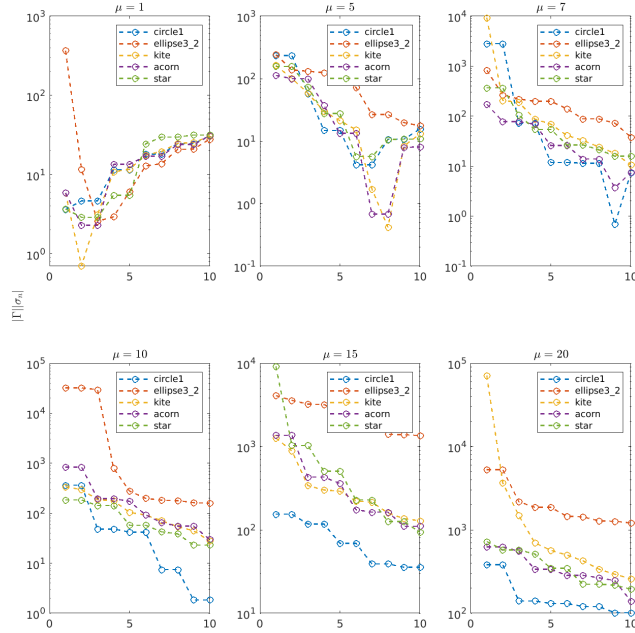


Figure 3.30: First 100 Steklov-Helmholtz eigenvalues of the disk, ellipse, kite, acorn and star with $\mu = 15$. On the right, $|M| = 1$.

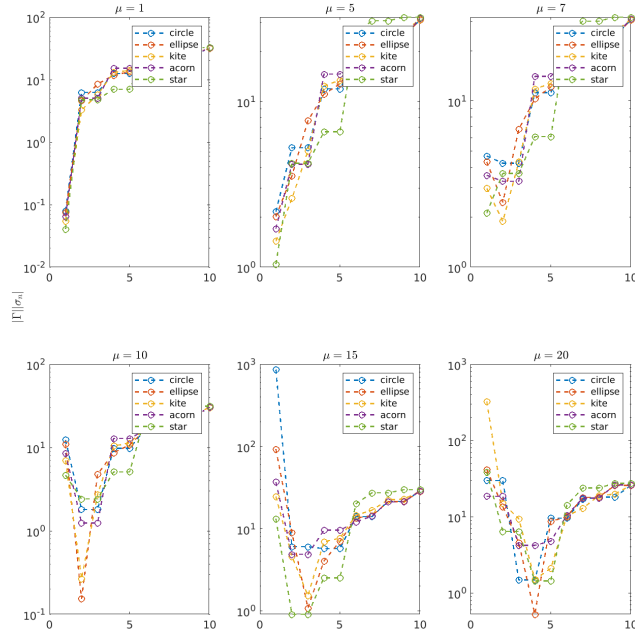
In [Figure 3.30](#) for non-normalized curves, we observe that the eigenvalues have very similar values later into the spectrum as compared to when $|M| = 1$. Next, we numerically test for some type of Weinstock inequality for the first eigenvalue and quickly see that it fails. In [Figure 3.31](#) we show the scaled eigenvalues of various domains and across various values of μ . On the left, we scale the absolute values of the first ten eigenvalues with the perimeters of the domains. On the right, we consider domains of perimeter $|\Gamma| := |M| = 1$. In each subplot, the wave number μ is fixed and we show the domains circle, ellipse, kite, acorn and star. We see on the left subfigure that for $\mu = 7$, $|M||\sigma_1|$ (top, right) the kite has the largest absolute eigenvalue. Since we take the absolute values and $\sigma_1 < 0$ for these domains, we have that the disk does not have smallest σ_1 . On the right subfigure for $\mu = 20$ (bottom, right) where all domains have perimeter one, we see that $|M||\sigma_1|$ the disk does not have smallest σ_1 .

First 10 $|\Gamma||\sigma_n|$ of some curves, $N = 1000$



(a) Here the perimeter is not 1.

First 10 $|\Gamma||\sigma_n|$ of some curves of length 1, $N = 1000$



(b) Here the perimeter is 1.

Figure 3.31: First 10 perimeter scaled absolute eigenvalues for the disk, ellipse, kite, acorn and star. On the left, the perimeter $|\Gamma| := |M| = 1$ is not 1. On the right we set $|\Gamma| = 1$. In each subplot the wave number μ is fixed. For different μ a different curve has the smallest eigenvalue.

In Figures 3.25-3.30 we observed that after a certain eigenvalue number k , the Steklov-Helmholtz spectrum can be fitted with a line. So, we fit a line to the eigenvalues for $k = 300 - 500$ for various domains (circle, ellipse, kite, acorn and star, see [Appendix A](#)) of perimeter 1. We consider wave numbers $\mu = 1, 5, 7, 10, 15, 20$. In [Table 3.8](#) we record the slopes and intercepts of the lines that we fit. We note that as μ increases, the slope values grow slightly bigger than π .

μ	Curve	Slope	Intercept	μ	Curve	Slope	Intercept
1	circle1	3.14159367971359	-1.56379687243969	10	circle1	3.14169527117375	-1.64452947454361
1	ellipse3_2	3.14159367972987	-1.56379688112999	10	ellipse3_2	3.14169527280023	-1.64453034290672
1	kite	3.14159368027954	-1.56379716835422	10	kite	3.14169532325044	-1.64455735641873
1	acorn	3.14159367994409	-1.56379699527511	10	acorn	3.1416952942226	-1.6445175838761
1	star	3.14159367283583	-1.5637939568997	10	star	3.14169549197768	-1.64464705270008
5	circle1	3.14161830699958	-1.58336790671401	15	circle1	3.14182355794865	-1.74647244441055
5	ellipse3_2	3.14161830740615	-1.58336812377562	15	ellipse3_2	3.1418235616092	-1.74647439869441
5	kite	3.14161832005116	-1.58337488924813	15	kite	3.14182367509261	-1.74653517085741
5	acorn	3.14161831276091	-1.58337097723548	15	acorn	3.14182360982237	-1.74650008974936
5	star	3.14161835529158	-1.58339418993543	15	star	3.14182406671124	-1.74674238073209
7	circle1	3.14164293489148	-1.60293926457575	20	circle1	3.14200318705751	-1.8892073545682
7	ellipse3_2	3.1416429356884	-1.60293969004139	20	ellipse3_2	3.14200319356746	-1.88921082997793
7	kite	3.14164296042987	-1.60295293430465	20	kite	3.14200339534883	-1.88931888925866
7	acorn	3.14164294618424	-1.60294528307894	20	acorn	3.14200327931181	-1.88925651846923
7	star	3.14164303836912	-1.60299475385583	20	star	3.14200410050772	-1.88969128925606

Table 3.8: Slopes and intercepts of lines of best fit to the Steklov-Helmholtz eigenvalues for $k = 300, \dots, 500$, for various domains of perimeter 1. The table on the left has $\mu = 1, 5, 7$ and the table on the right has $\mu = 10, 15, 20$. All slopes are $\approx \pi$.

We briefly summarize our observations.

- $\sigma_k \approx \frac{k\pi}{|M|}$,
- $N(x) \approx \frac{x|M|}{\pi}$.

We are currently exploring these asymptotics further with searches for dependence on the wave number μ possibly in the second term.

3.6 Boundary weights

As mentioned in [Remark 2.4.2](#), we consider adding positive and bounded weights ρ on M . We begin with checking for a breakdown of our method. Suppose we take a continuous density such that $\rho(0) \neq \rho(2\pi)$. In [Figure 3.32](#) we consider a continuous weight $\rho(t) = 10t^3$ which is not 2π -periodic. We take the star (see [Appendix A](#)) with $\mu = 5$. The weighted problem does not converge with real eigenvalues. We show in the first row on the left the eigenvalues σ_k (blue) and $\text{real}(\sigma_{\rho,k})$

(red). In the first row on the right we show the ratio $\sigma_k/\text{real}(\sigma_{k,\rho})$. In the second row we show the density $\rho(t)$.

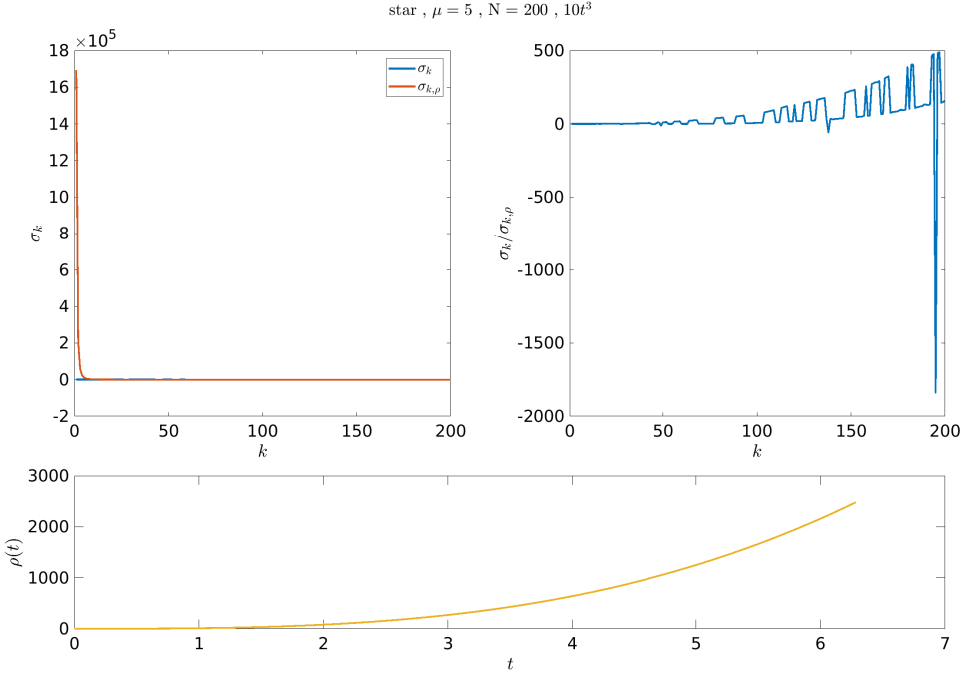


Figure 3.32: In the top left are the Steklov-Helmholtz eigenvalues σ_k (blue) and real part of the $\sigma_{k,\rho}$ (red). Note that $\sigma_{k,\rho} \in \mathbb{C}$ which means that our method does not work since $\rho(0) \neq \rho(2\pi)$. In the top right are the ratios of the $\sigma_k/\text{real}(\sigma_{k,\rho})$. The bottom row shows the density $\rho(t) = 10t^3$.

Now we recall [Equation 1.25](#),

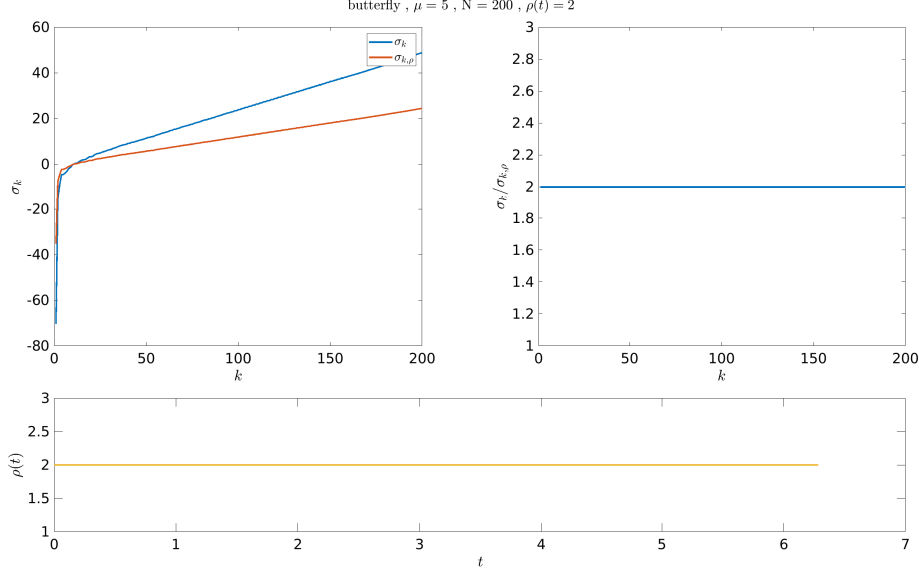
$$\sigma_\rho = \frac{\|\nabla U\|_{L^2(\Omega)}^2 - \mu^2 \|U\|_{L^2(\Omega)}^2}{\|\sqrt{\rho} TU\|_{L^2(M)}^2}. \quad (1.25)$$

and we set $\rho \equiv c \in \mathbb{R}$. This gives $\sigma_{\rho,k} = \frac{\sigma_k}{\rho}$.

In [Figure 3.33](#) we consider a constant weight $\rho \equiv 2$ for the butterfly (see [Appendix A](#)) with $\mu = 5$. In subfigure (a) we show in the first row on the left the eigenvalues σ_k (blue) and $\sigma_{\rho,k}$ (red). In the first row on the right we show the ratio $\sigma_k/\sigma_{\rho,k} = 2$ as expected. In the second row we show the density $\rho(t) = 2$. In subfigures (b) and (c) we compare the 5th eigenfunctions on the boundary and inside Ω . For this constant density, we observe that the eigenfunctions are linearly dependent and we record the subspace angles in the plots.

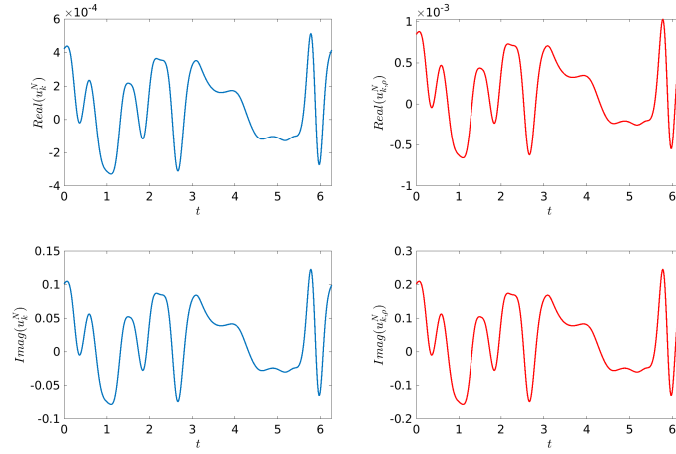
In [Figure 3.34](#) we consider a continuous weight $\rho(t) = 5 \exp(-\sin t) + \cos^3(t)$ for the butterfly with $\mu = 5$. Note that $\rho(0) = \rho(2\pi)$. In subfigure (a) we show in the first row on the left the

eigenvalues σ_k (blue) and $\sigma_{k,\rho}$ (red). In the first row in the middle we show the ratio $\sigma_k/\sigma_{k,\rho}$. In the first row on the right, we show $\sigma_k/\rho(k)$ (green) and $\sigma_{k,\rho}$ (red). Here we observe that the boundary-weighted eigenvalues lie between the ratio $\sigma_k/\rho(k)$. In the second row we show the density $\rho(t)$. In subfigures (b) and (c) we compare the 7th eigenfunctions on the boundary and inside Ω . For this density, we observe that the eigenfunctions are not linearly dependent due to the large subspace angles (70-73 degrees) that we record in the plots.

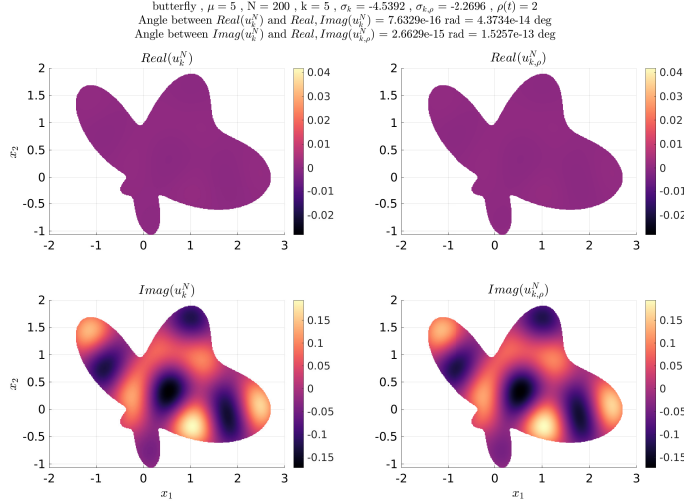


(a) In the top left are the Steklov-Helmholtz eigenvalues σ_k (blue) and $\sigma_{k,\rho}$ (red). In the top right are the ratios $\sigma_k/\sigma_{k,\rho} = 2$. The bottom row shows the density $\rho \equiv 2$.

On the boundary of butterfly, $\mu = 5$, $N = 200$, $k = 5$, $\sigma_k = -4.5392$, $\sigma_{k,\rho} = -2.2696$, $\rho(t) = 2$
Angle between $\text{Real}(u_{k,\rho}^N)$ and $\text{Real}, \text{Imag}(u_k^N) = 4.6323e-12$ rad = $2.6541e-10$ deg
Angle between $\text{Imag}(u_{k,\rho}^N)$ and $\text{Real}, \text{Imag}(u_k^N) = 2.2204e-16$ rad = $1.2722e-14$ deg

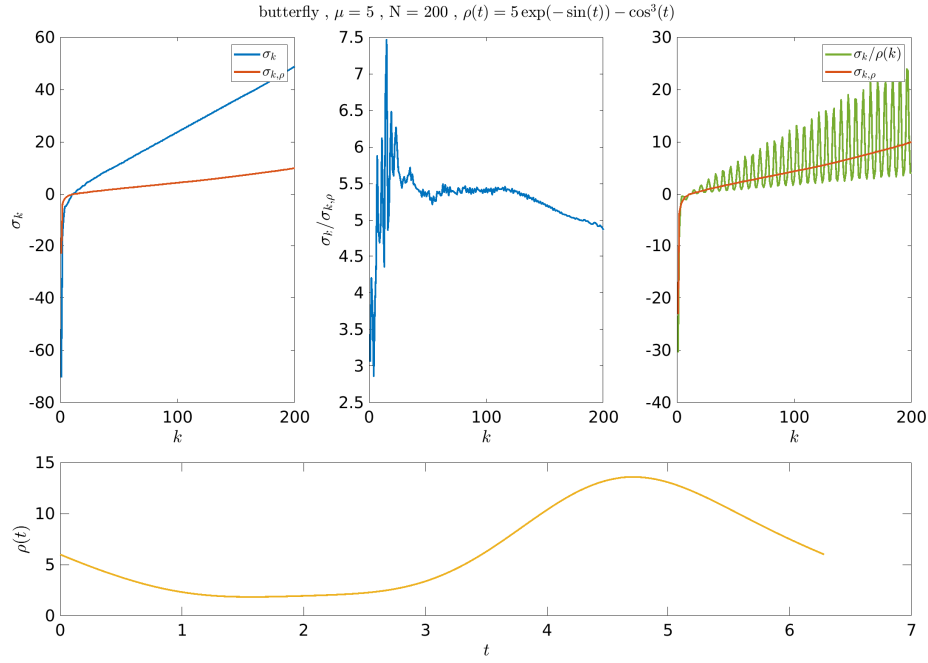


(b) For $k = 5$ the eigenfunctions on the boundary, for the non-weighted (left,blue) weighted (right,red) problems.

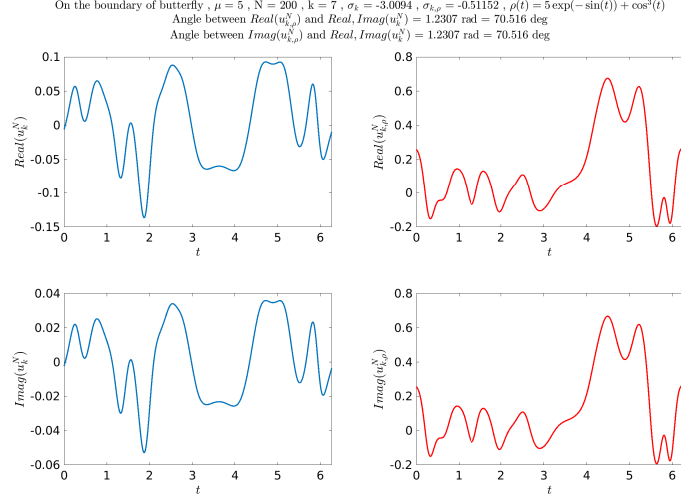


(c) For $k = 5$ the eigenfunctions in Ω , for the non-weighted (left) weighted (right) problems.

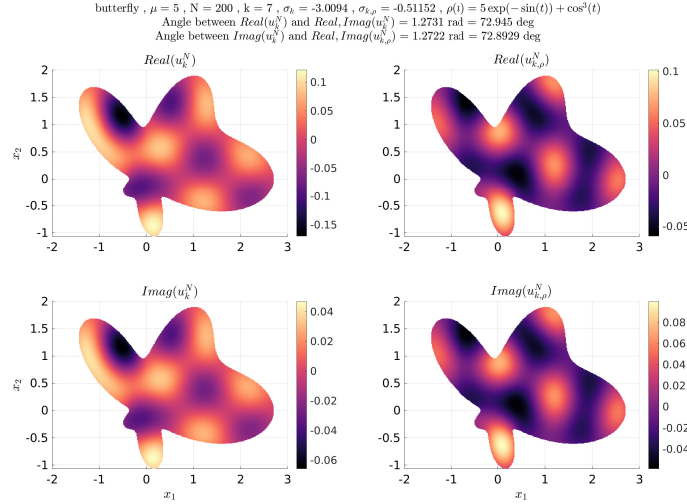
Figure 3.33: Comparison of the Steklov-Helmholtz problem and boundary-weighted Steklov-Helmholtz problem. $\mu = 5$, constant density $\rho \equiv 2$ for butterfly. In subfigure (a) are the spectrum of the 2 problems and the density. The 5th eigenfunctions are compared in subfigures (b), (c). The subspace angles between the eigenfunctions are near 0.



(a) In the top left are the Steklov-Helmholtz eigenvalues σ_k (blue) and $\sigma_{k,\rho}$ (red). In the top middle are the ratios $\sigma_k/\sigma_{k,\rho}$. In the first row on the right, we show $\sigma_k/\rho(k)$ (green) and $\sigma_{k,\rho}$ (red). The bottom row shows the density $\rho(t) = 5 \exp(-\sin t) + \cos^3(t)$.



(b) For $k = 7$ the eigenfunctions on the boundary, for the non-weighted (left,blue) weighted (right,red) problems.



(c) For $k = 7$ the eigenfunctions in Ω , for the non-weighted (left) weighted (right) problems.

Figure 3.34: Comparison of the Steklov-Helmholtz problem and boundary-weighted Steklov-Helmholtz problem. $\mu = 5$, constant density $\rho(t) = 5 \exp(-\sin t) + \cos^3(t)$ for butterfly. In subfigure (a) are the spectrum of the 2 problems and the density. The 7th eigenfunctions are compared in subfigures (b), (c). The subspaces angles between the eigenfunctions are reported in the plots.

3.7 Shape optimization of Steklov-Helmholtz eigenvalues

The goal of this section is to find a curve belonging to a family of curves with the same parameterization and length (or area) which admits maximum (or minimum) k th scaled eigenvalue $f_\Omega \sigma_k$. Here f_Ω is either the perimeter $|M|$ or the square root of the area $\sqrt{|\Omega|}$. Suppose we perturb the domain $\Omega_t = \Psi_t(\Omega)$, $\Psi_t(x) = x + tv(x)$, where v is called the velocity and $t \geq 0$. Informally, the

idea is to use the *rate of change of the eigenvalues with respect to the domain perturbing parameter* t . This rate of change evaluated at $t = 0$ is captured by the *shape derivative* of σ_k . Recalling the variational formulation of the Steklov eigenvalues (see [Equation 1.26](#)),

$$\sigma_k = \frac{\int_{\Omega} |\nabla u|^2 \, dx - \mu^2 \int_{\Omega} |u|^2 \, dx}{\int_M |u|^2 \, ds},$$

where $u \in \mathbb{C}$ is the k th normalized eigenfunction with $\int_M |u|^2 \, ds = 1$. Denoting by $(\cdot)'$ the shape derivative and from equation 4.7 (Chapter 9) in [\[DZ11\]](#) we get,

$$\sigma'_k = \int_{\Omega} (\nabla u \cdot \nabla \bar{u})' - \mu^2 (u \bar{u})' \, dx + \int_M (|\nabla u|^2 - \mu^2 |u|^2) v \cdot \nu \, ds.$$

Since σ'_k is real we get,

$$\sigma'_k = \int_{\Omega} 2\operatorname{Re}(\nabla \bar{u} \cdot \nabla u' - \mu^2 \bar{u} u') \, dx + \int_M (|\nabla u|^2 - \mu^2 |u|^2) v \cdot \nu \, ds.$$

Using Divergence Theorem and the Steklov-Helmholtz problem gives,

$$2\operatorname{Re} \int_{\Omega} \nabla \bar{u} \cdot \nabla u' \, dx = 2\operatorname{Re} \int_{\Omega} \nabla \cdot (u' \nabla \bar{u}) - u' \Delta \bar{u} \, dx = 2\sigma_k \operatorname{Re} \int_M u' \bar{u} \, ds + 2\mu^2 \operatorname{Re} \int_{\Omega} \bar{u} u' \, dx. \quad (3.15)$$

Also, using equation 4.17 (Chapter 9) in [\[DZ11\]](#) on the normalization $\int_M |u|^2 \, ds = 1$ we get,

$$\begin{aligned} 0 &= \int_M (|u|^2)' + (\partial_{\nu} |u|^2 + \kappa |u|^2) v \cdot \nu \, ds = \int_M (u \bar{u})' + (2\bar{u} \partial_{\nu} u + \kappa |u|^2) v \cdot \nu \, ds \\ &= \int_M 2\operatorname{Re}(\bar{u} u') + (2\sigma_k |u|^2 + \kappa |u|^2) v \cdot \nu \, ds, \end{aligned} \quad (3.16)$$

where κ is the mean curvature of Ω . Then using Equations [\(3.15\)](#) and [\(3.16\)](#) in σ'_k give,

$$\sigma'_k = \int_M (|\nabla u|^2 - \mu^2 |u|^2 - 2\sigma_k^2 |u|^2 - \kappa \sigma_k |u|^2) v \cdot \nu \, ds. \quad (3.17)$$

Writing $\nabla u = \nabla_{\Gamma} u + \partial_{\nu} u \, \nu$, the tangential gradient of u is,

$$\nabla_{\Gamma} u = \nabla u - \partial_{\nu} u \, \nu = \nabla u - (\nabla u \cdot \nu) \, \nu. \quad (3.18)$$

On squaring both sides and rearranging, $|\nabla u|^2 = |\nabla_{\Gamma} u|^2 + \sigma_k^2 |u|^2$. Substituting in [\(3.17\)](#) we get an equivalent formulation,

$$\sigma'_k = \int_M (|\nabla_{\Gamma} u|^2 - \mu^2 |u|^2 - \sigma_k^2 |u|^2 - \kappa \sigma_k |u|^2) v \cdot \nu \, ds. \quad (3.19)$$

To compute the integral $\int_M |\nabla_\Gamma u|^2 \, ds$ in (3.19), a couple strategies have been used. The first is to conformally map the boundary M to that of the unit disk [AK19] (there exists a conformal map from any C^2 curve to the unit disk). Then it is possible to directly compute $\nabla_\Gamma u$ where the tangential direction coincides with that of the angular parameter θ . The second strategy is to interpolate the eigenfunction using RBFs. Once we interpolated, we have a closed form of the eigenfunction via the RBF coefficients and so we can compute the gradient. Then we can use the definition of the tangential gradient (3.18) to approximate it. Since the first strategy does not hold when M is not C^2 , we try the second strategy. We find the interpolant for the eigenfunction u using RBFs as described in algorithm 2. We then compute the gradient of the RBF interpolant and finally use (3.18) to compute $\nabla_\Gamma u$. We recall the RBF interpolant form (3.1) for the eigenfunction vector $u = \{u_i\}_{i=1}^{2N}$ evaluated at the boundary points $\{X_i\}_{i=1}^{2N}$. For any $Z = (Z_1, Z_2) \in \mathbb{R}^2$:

$$u_{RBF}(Z) = \sum_{j=1}^{2N} \eta_j \phi(|Z - X_j|),$$

such that $u_i = u_{RBF}(X_i)$. We can compute the gradient of this interpolant as

$$\nabla u_{RBF}(Z) = \left(\sum_{j=1}^{2N} \eta_j \phi_{Z_1}(|Z - X_j|), \sum_{j=1}^{2N} \eta_j \phi_{Z_2}(|Z - X_j|) \right), \quad (3.20)$$

where $\phi_{Z_i}(|Z - X_j|)$ is the partial derivative of the RBF ϕ with respect to Z_i , $i = 1, 2$. We can compute these partial derivatives by hand since the RBFs are infinitely differentiable and have *nice* closed forms. We describe the computation of the tangential gradient via RBF interpolation below in Algorithm 3.

Algorithm 3 Approximating the tangential gradient $\nabla_\Gamma u$ using RBFs, see Appendix B.6

Require: Eigenfunction vector $u = \{u_i\}_{i=1}^{2N}$, evaluation points $\{X_i = (x_i, y_i)\}_{i=1}^{2N}$, curve details

Find the RBF coefficients $\{\eta_i\}_{i=1}^{2N}$ using Algorithm 2 such that $u_{RBF}(Z) = \sum_{j=1}^{2N} \eta_j \phi(|Z - X_j|)$ and $u_{RBF}(X_i) = u_i$, $i = 1, \dots, 2N$.

Compute $\nabla u_{RBF}(Z)$ as per (3.20) for any Z on the boundary M .

Using the boundary parametrization, compute outer unit normal ν to M at Z .

Compute $\nabla_{\Gamma, RBF} u(Z) = \nabla u_{RBF}(Z) - (\nabla u_{RBF}(Z) \cdot \nu) \nu$

We check how well this approximation works on the disk, where we can compute the true tangential gradient. Let the true $\nabla_\Gamma u$ for a circle with radius R , be denoted by $\nabla_\Gamma^{\text{circle}} u = \frac{ik}{R} J_k(\mu R) e^{ik\theta} \tau$, where $\tau = (-\nu_2, \nu_1)$. We report on the subspace angles between $\nabla_\Gamma^{\text{circle}} u$ and $\nabla_\Gamma^{\text{approx}} u := \nabla_{\Gamma, RBF} u$ in Table 3.9. We set $N = 300$, take $\mu = 1, 2, 3, 7, 10, 12, 15$ and $R = 1, 5, 10$. We compare the $k = 1, 10, 20$ eigenfunctions. The subspace angles we see in Table 3.9 are low enough for our

purpose and hence we conclude that this approximation can be used to compute the tangential gradients.

μ	R	k	$\angle(\nabla_{\Gamma}^{\text{circle}} u, \text{real}(\nabla_{\Gamma}^{\text{approx}} u))$	$\angle(\nabla_{\Gamma}^{\text{circle}} u, \text{imag}(\nabla_{\Gamma}^{\text{approx}} u))$	$\angle(\nabla_{\Gamma}^{\text{circle}} u, \text{real}(\nabla_{\Gamma}^{\text{approx}} u))$	$\angle(\nabla_{\Gamma}^{\text{circle}} u, \text{imag}(\nabla_{\Gamma}^{\text{approx}} u))$
1	1	1	0	0	7	1
1	1	10	4.30833733464557e-12	2.31681206057306e-11	7	10
1	1	20	4.85446146011901e-12	4.36751238099931e-12	7	20
1	5	1	2.57781652509372e-11	3.73060269847776e-11	7	1
1	5	10	3.32850366873246e-12	2.7030574676784e-12	7	10
1	5	20	3.63153909933424e-12	6.20231931364174e-12	7	20
1	10	1	4.93602204136272e-11	3.49624571948553e-10	10	1
1	10	10	2.18343757318985e-11	1.55756289371898e-11	10	10
1	10	20	5.44678586912358e-12	5.06573837857797e-12	10	1
2	1	1	0	0	10	5
2	1	10	3.73715067821804e-12	1.30501693010322e-09	10	5
2	1	20	4.43455846544132e-12	4.31539532528977e-11	10	5
2	5	1	1.08992900897167e-10	3.60354482798356e-10	10	10
2	5	10	1.11877779670574e-11	5.78290584104164e-12	10	10
2	5	20	2.61303260649826e-12	3.53541163502748e-12	10	10
2	10	1	3.69922794498284e-11	1.4829526204031e-11	12	1
2	10	10	3.48022075385483e-12	4.9887196572421e-12	12	10
2	10	20	5.22539010472587e-12	3.6034224025578e-12	12	1
3	1	1	2.39760892471087e-11	2.75653102704988e-11	12	5
3	1	10	3.68698820297483e-12	6.92803289114338e-12	12	5
3	1	20	4.12096030425514e-12	6.52527487609322e-11	12	5
3	5	1	3.83594826721404e-12	1.02578315982293e-11	12	10
3	5	10	1.81091612222618e-12	7.00156692159009e-12	12	10
3	5	20	6.6435469227607e-12	2.57527508131184e-12	12	10
3	10	1	1.94062084706083e-11	3.13153010364896e-10	15	1
3	10	10	3.14621866034451e-12	4.65578443793589e-12	15	10
3	10	20	3.30390468026757e-12	7.43883500364739e-12	15	1
					15	5
					15	10
					15	20

Table 3.9: The **subspace** angles between true ($\nabla_{\Gamma}^{\text{circle}} u$) and RBF approximated ($\nabla_{\Gamma}^{\text{approx}} u$) tangential gradients for various circles, $N = 300$. The first column contains the wave number μ , the second column contains the radius R , the third column contains the eigenvalue number k . The fourth column contains the **subspace** angles between $\nabla_{\Gamma}^{\text{circle}} u$ and the real part of $\nabla_{\Gamma}^{\text{approx}} u$. The fifth column contains the **subspace** angles between $\nabla_{\Gamma}^{\text{circle}} u$ and the imaginary part of $\nabla_{\Gamma}^{\text{approx}} u$.

Now that we have an idea on how to compute ∇_{Γ} , we move on to the next steps. From [Lemma 3.5.1](#), the eigenvalues do not scale with the domain and so we cannot fix $|M|$ or the area and we consider, $(f(\Omega)\sigma_k)' = f(\Omega)\sigma_k' + f(\Omega)'\sigma_k$. From equations (4.20) and (4.21) in Chapter 9 of [\[DZ11\]](#),

$$f(\Omega)' = \begin{cases} |M|' = \int_M \kappa v \cdot \nu \, ds & \text{when } f(\Omega) = |M|, \\ \frac{|\Omega|'}{2\sqrt{|\Omega|}} = \frac{\int_M v \cdot \nu \, ds}{2\sqrt{|\Omega|}} & \text{when } f(\Omega) = \sqrt{|\Omega|}. \end{cases}$$

Finally we have the scaled shape derivatives for the scaled eigenvalues,

$$(|M|\sigma_k)' = |M| \int_M (|\nabla_\Gamma u|^2 - \mu^2|u|^2 - \sigma_k^2|u|^2 - \kappa\sigma_k|u|^2)v \cdot \nu \, ds + \sigma_k \int_M \kappa v \cdot \nu \, ds, \quad (3.21)$$

and

$$\left(\sqrt{|\Omega|}\sigma_k\right)' = \sqrt{|\Omega|} \int_M (|\nabla_\Gamma u|^2 - \mu^2|u|^2 - \sigma_k^2|u|^2 - \kappa\sigma_k|u|^2)v \cdot \nu \, ds + \frac{\sigma_k}{2\sqrt{|\Omega|}} \int_M v \cdot \nu \, ds, \quad (3.22)$$

In this type of formulation for the Steklov-Laplace optimization problem, the perimeter length can be fixed. This is because the eigenvalues scale on scaling the domain (see [Equation 3.13](#)). The Steklov-Helmholtz eigenvalues have a different homothetic property (see [Equation 3.11](#)) and as seen in [Section 3.5.2](#) simply scaling the domain, does not scale the eigenvalues. So fixing a value for $|M| = \gamma$ will only provide information on optimum eigenvalues for domains of perimeter γ , and domains related through [Equation 3.11](#).

We numerically evaluate these integrals by the Trapezoidal rule. As usual, we begin our experiments on the disk, where the shape controlling parameter is only the radius R . Hence σ'_k is a scalar with $v = (r \cos t, r \sin t)_{r|R} = (\cos t, \sin t)$. For the disk $|M| = 2\sqrt{\pi|\Omega|}$, and so both the functionals (in exact form)

$$|M|\sigma_k = 2\pi\mu R \frac{J'_k(\mu R)}{J_k(\mu R)} \text{ and } \sqrt{|\Omega|}\sigma_k = \sqrt{\pi}\mu R \frac{J'_k(\mu R)}{J_k(\mu R)}$$

have the same optimizer. Therefore we only consider optimizing $|M|\sigma_k$ for the circle. Even though we must assume for the Steklov-Helmholtz eigenvalue problem that μ^2 is not a Dirichlet-Laplace eigenvalue, as the shape optimization progresses we can not guarantee that μ^2 avoids the Dirichlet spectrum for the updated domain $\tilde{\Omega}$. We plot for reference an example of this, where we know that $\mu = 1$ is not a Dirichlet eigenvalue for the unit disk. However, on moving the radius we eventually hit a Dirichlet-Laplace eigenvalue.

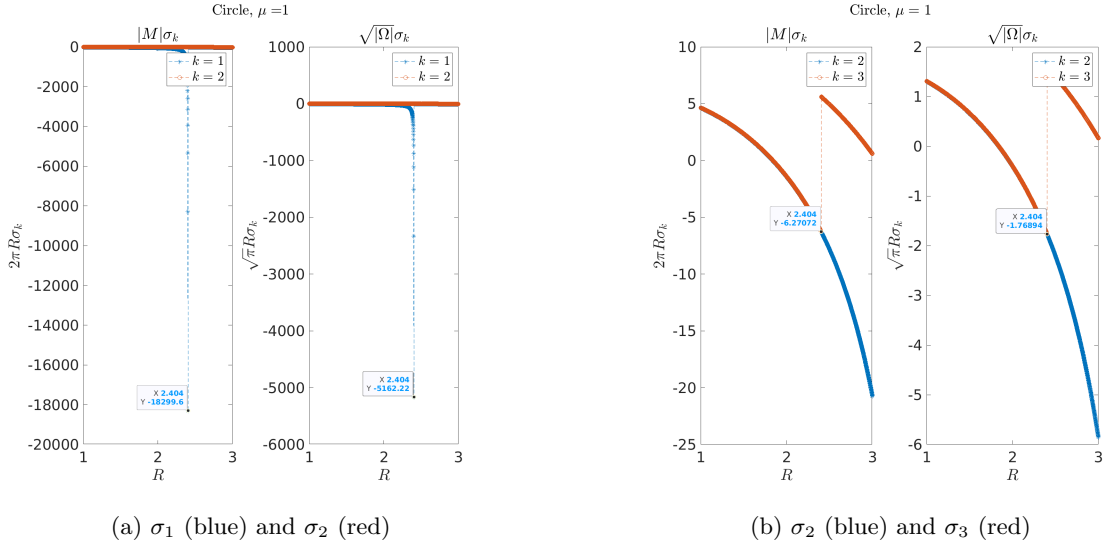
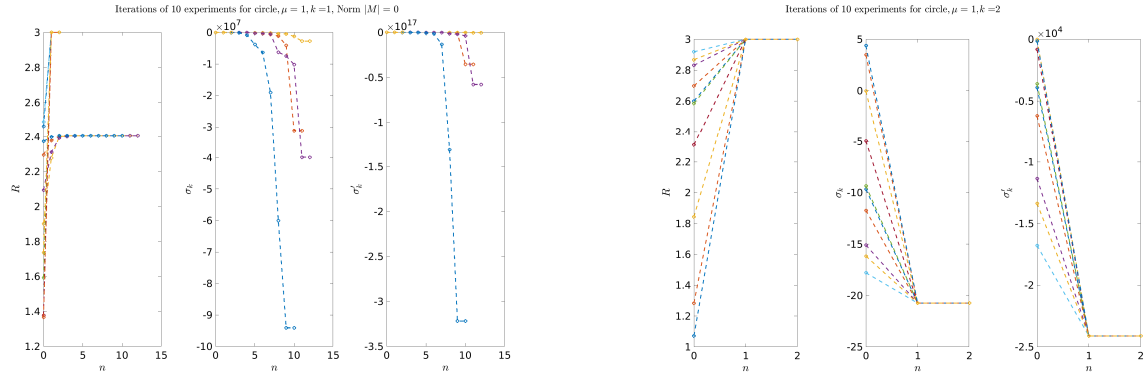
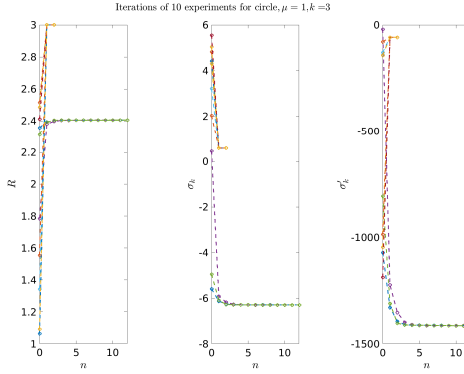


Figure 3.35: Scaled eigenvalues for circles with stepsize for $R = 0.001$ and $R \in [1, 3]$. The first 3 eigenvalues are shown. In subfigure (a) $k = 1, 2$. In subfigure (b) $k = 2, 3$. In each subfigure, on the left is $|M|\sigma_k$ and on the right $\sqrt{|Ω|}\sigma_k$.

In Figure 3.35 we show $|M|\sigma_k$ (left) and $\sqrt{|Ω|}\sigma_k$ (right) for $k = 1$ (blue) and $k = 2$ (red) for $R \in [1, 3]$. We observe for $k = 1$ that as $R \rightarrow 2.404$ that $\sigma_1 \rightarrow -\infty$. Similar behaviour is observed for $k = 3$. On the other other hand, for $R \in [1, 3]$, σ_2 monotonically decreases, with minima at $R = 3$. We consider gradient based approaches as in [AKO17] and [Ant21]. Using the MATLAB function `fmincon` with ten random initial radii R_0 in $[1, 3]$ and $N = 300$, we perform a search for a minima of $\sigma_i, i = 1, 2, 3$ (the function `fmincon` allows input of gradients, and we supply to it the shape derivative (3.19)).



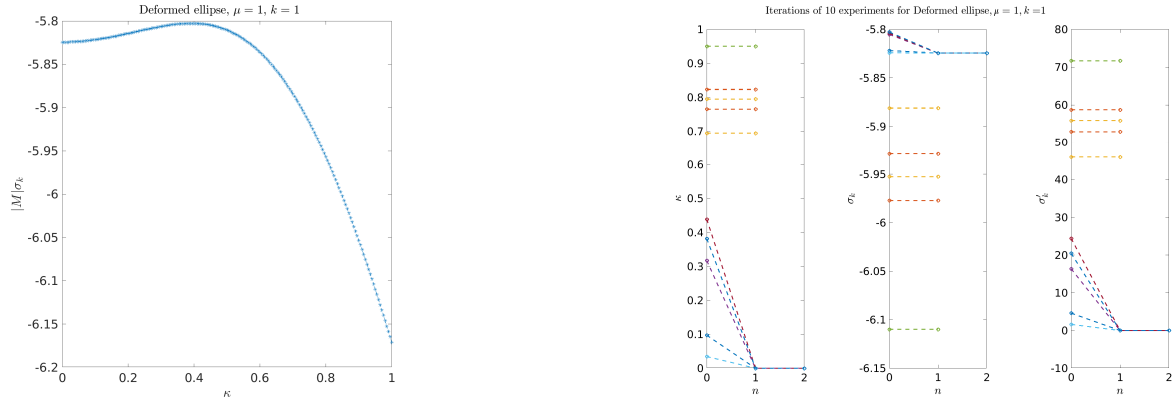
(a) For $k = 1$, note that all experiments converge to $R \approx 2.404$. (b) For $k = 2$, note that all experiments converge to $R = 3$ which is the true minimizer.



(c) For $k = 3$ also, all experiments converge to $R \approx 2.404$.

Figure 3.36: 10 Experiments for the first 3 Steklov-eigenvalues of disks with radii in $[1, 3]$. Subfigure(a) shows experiments for $k = 1$, subfigure(b) shows experiments for $k = 2$ and subfigure(c) shows experiments for $k = 3$. Each subfigure show iterations of the radii R (left), the eigenvalue σ_k (middle) and the shape derivative σ'_k (right) for each of the 10 experiments. For $k = 1, 3$ the optimization converges to a Dirichlet-Laplace eigenvalue.

For $k = 1, 3$ (Figure 3.36 (a,c)) we observe convergence to a local minimum $R \approx 2.40482$ if $R_0 < R$. For $k = 2$, the algorithm takes R_0 to the correct optimizer $R = 3$ (see Figure 3.35(b) and Figure 3.36(b)). Next, we consider the deformed ellipse (see Appendix A) in Figure 3.37 with the only shape controlling parameter κ_p , and velocity $v = (\cos 2t - 1, 0)$ and use `fmincon` with a random initial parameter κ_{p0} in $[0, 1]$ and $N = 300$. Here, even though there seems to be no possibility of Dirichlet eigenvalue, the algorithm barely even moves from the initial point.

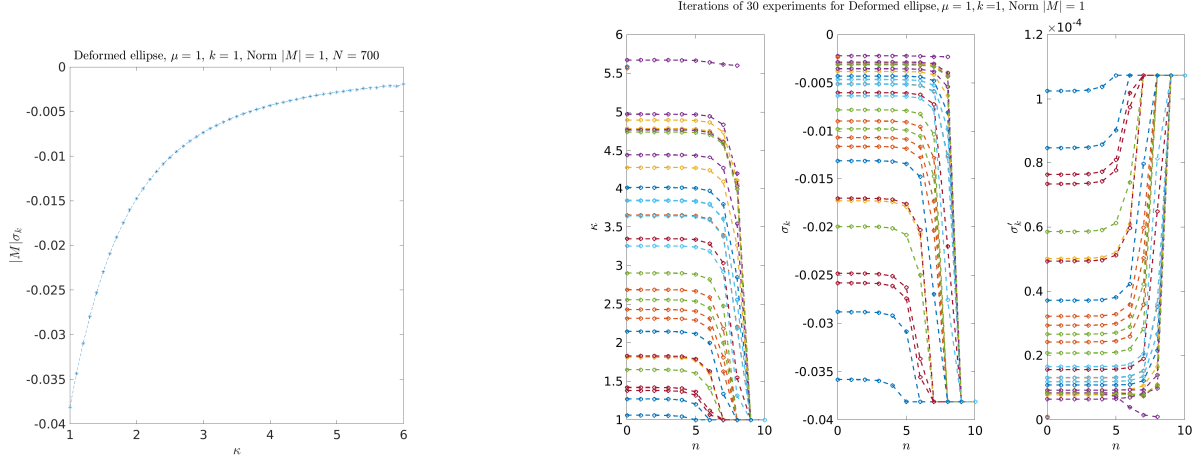


(a) Scaled eigenvalues for deformed ellipses with stepsize for $\kappa = 0.01$

(b) The algorithm either gets stuck or defaults to an end point.

Figure 3.37: 10 Experiments for the first Steklov-eigenvalues of the deformed ellipse for $\kappa \in [0, 1]$. Subfigure(a) shows the actual scaled eigenvalues for $k = 1$, subfigure(b) shows experiments for $k = 1$. Subfigure(b) show iterations of the radii R (left), the eigenvalue σ_k (middle) and the shape derivative σ'_k (right) for each of the 10 experiments.

Here, even though there seems to be no possibility of Dirichlet eigenvalue, the algorithm barely even moves from the initial point. Finally we consider the optimization problem: *find* $\min \sigma_k(\Omega)$ over all Ω of fixed perimeter length $|M| = 1$. In this case we just optimize σ_k since $|M| = 1$. In Figure 3.38 we show experiments for the deformed ellipse. While the optimization seems to work, it is unclear whether we have convergence or defaulting of the algorithm to an endpoint where the minimum coincidentally occurs.



(a) Scaled eigenvalues for deformed ellipses with stepsize for $\kappa = 0.01$

(b) The algorithm either gets stuck or defaults to an end point.

Figure 3.38: 10 Experiments for the first Steklov-eigenvalues of the deformed ellipse for $\kappa \in [1, 6]$. Subfigure(a) shows the actual scaled eigenvalues for $k = 1$, subfigure(b) shows experiments for $k = 1$. Subfigure(b) show iterations of the radii R (left), the eigenvalue σ_k (middle) and the shape derivative σ'_k (right) for each of the 10 experiments. Here $|M| = 1$ is fixed.

We perform similar experiments for an ellipse with parameters a, b varying between 3 and 8 (see Appendix B). Normalized to length one, we note that combinations of (a, b) with the same ratio give the same ellipse. Suppose $(a_0 = 1, b_0 = 2)$, $(a_1 = 2, b_1 = 4)$ and $(a_2 = 4, b_2 = 8)$. Then shrunk to length 1 we get the same ellipse from all three configurations. We set $\mu = 5$ and $k = 7$ and observe the smallest eigenvalue occurs when $a = b$ (which is actually a circle of radius $1/(2\pi)$). Of 30 experiments for this configuration we observe that 26 converge to $a = b = 8$. While this is a correct configuration, it is still an endpoint of the parameter space $[3, 8] \times [3, 8]$ that we search. This time however, there are multiple configurations (a, a) , $a = 3, 4, \dots, 8$ which are correct and the algorithm only goes to $(8, 8)$. So it is possible that the algorithm just defaults to an endpoint.

Chapter 4

Transmission eigenvalue problem

In this short chapter we consider the transmission eigenvalue problem for the Helmholtz equation which we recall as problem (1.3) : *find wave number $\mu \in \mathbb{C}$ such that there exist non trivial solutions $V, W \in L^2(\Omega)$ and $V - W \in H^2(\Omega)$ for*

$$\begin{cases} \Delta V + \mu^2 V = 0 \text{ in } \Omega, \\ \Delta W + n\mu^2 W = 0 \text{ in } \Omega, \\ V = W \text{ on } M, \\ \partial_\nu V = \partial_\nu W \text{ on } M. \end{cases} \quad (4.1)$$

Here $n := n_{RI}$ is the refractive index of an inhomogeneous medium in a bounded domain $\Omega \subset \mathbb{R}^2$ with $M =: \partial\Omega$ smooth enough and ν is the outward unit normal direction. We consider the problem reformulated as a boundary integral equation in terms of the DtN map as described in [Section 1.7.4](#).

Summarizing the details, we have the DtN map given by $\mathcal{D}_{\mu,n} = (I + K'_{\mu,n})S_{\mu,n}^{-1}$. The goal is to search for a wave number μ such that the difference operator of DtN maps ([Equation 1.27](#)),

$$N(\mu) : H^{-1/2}(M) \rightarrow H^{1/2}(M), \quad N(\mu) = \mathcal{D}_{\mu,n} - \mathcal{D}_{\mu,1}, \quad (4.2)$$

has a non-trivial kernel. Reformulated as an integral equation, we need to find μ, ϕ such that

$$N(\mu)\phi = 0, \quad (4.3)$$

has a non-trivial solution. Note now that in terms of the potential layer and the boundary density ϕ we have that $V = S_\mu(\phi)(x)$ and $W = S_{\sqrt{n}\mu}(\phi)(x)$. This will be useful while computing solutions inside Ω .

4.1 Searching for transmission eigenvalues

We use the discretized layer potentials matrices in [Section 2.4](#) to search for possible transmission eigenvalues, similar to the search for Laplace Dirichlet and Neumann eigenvalues in [Section 3.1.2](#). We recall [Remark 2.4.1](#) to denote the discretized operator matrix $N(\mu)$ by

$$C(\mu) = (A_{\mu,1} + Id)B_{\mu,1}^{-1} - (A_{\mu,n_{RI}} + Id)B_{\mu,n_{RI}}^{-1} \quad (4.4)$$

Our search procedure is very similar to [Algorithm 1](#) and we describe it in [Algorithm 4](#) below.

Algorithm 4 Search for transmission eigenvalues μ_T

Require: Curve details, $[\mu_{\min}, \mu_{\max}]$ and number of points N_T to search for within range.

for $\mu_{\min} \leq \mu_j \leq \mu_{\max}$ **do**

 Compute $C(\mu_j) = (A_{\mu_j,1} + Id)B_{\mu_j,1}^{-1} - (A_{\mu_j,n_{RI}} + Id)B_{\mu_j,n_{RI}}^{-1}$

 Find smallest singular value s_{\min_j} of $C(\mu_j)$

end for

Use sign flip and RBF interpolation using [Algorithm 2](#) to find possible zeros (see [Remark 3.1.1](#) and [Remark 3.1.2](#)).

4.2 Tests

In Section 4 of [\[CK17\]](#), the authors list the transmission eigenvalues for some domains. With reference to these reported values, we test whether our search finds the correct transmission eigenvalues. In [Figure 4.1](#) we show the output of [Algorithm 4](#) after RBF interpolation and zero finding. We search for transmission eigenvalues of an egg with curvature 0.2 (see [Appendix A](#)) for $\mu \in [1, 6]$ with a step of $1/60 \approx 0.0167$. We compare with the values in column 5 of table 2 in [\[CK17\]](#). The values are 3.38239, 3.61769, 3.80771, 4.12712, 4.37938, 4.84546, 4.90266, 5.43618, 5.49621, 5.99979. We observe that our approach is able to locate the transmission eigenvalues up to 4 digits of accuracy with a very low computational cost.

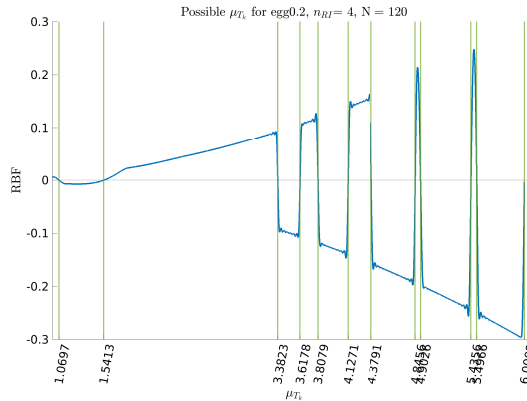
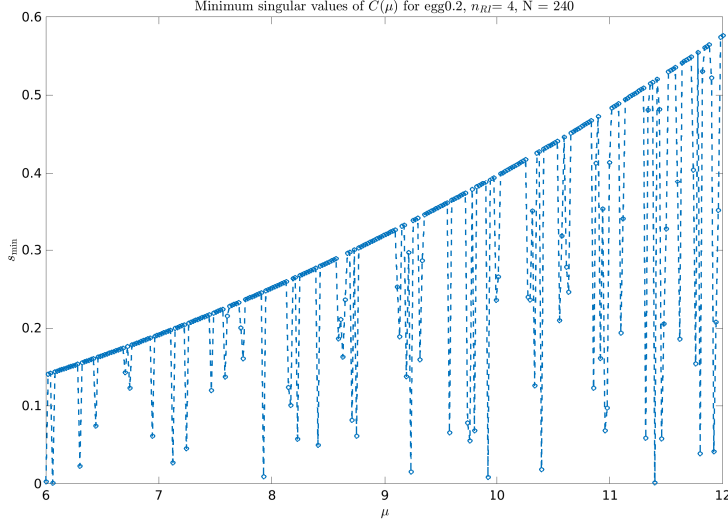
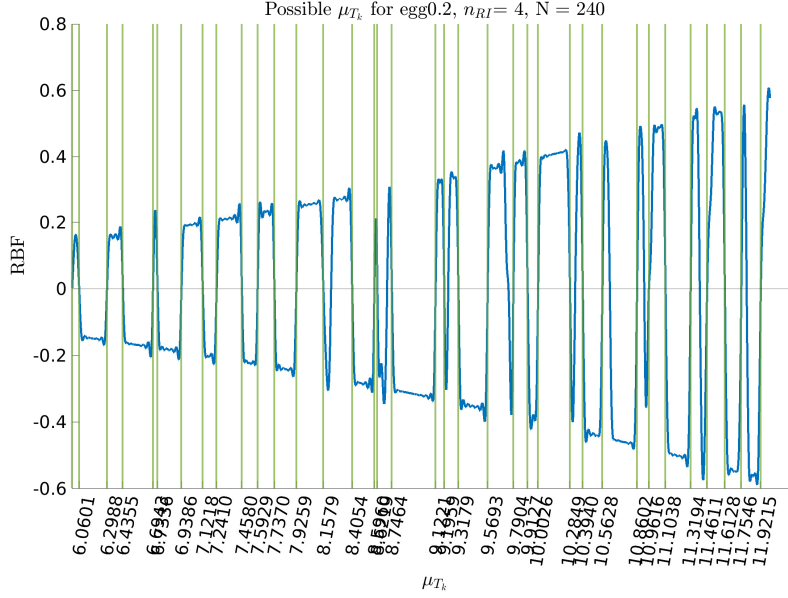


Figure 4.1: Locating zeros using algorithm 4 for egg with curvature 0.2, $n_{RI} = 4$ and $N = 120$.

We experiment for the same curve for $\mu \in [6, 12]$ and in [Figure 4.2](#) we show both phases of [Algorithm 4](#). In subfigure (a) we show the minimum singular values and in subfigure (b) the subsequent RBF interpolation and root finding.



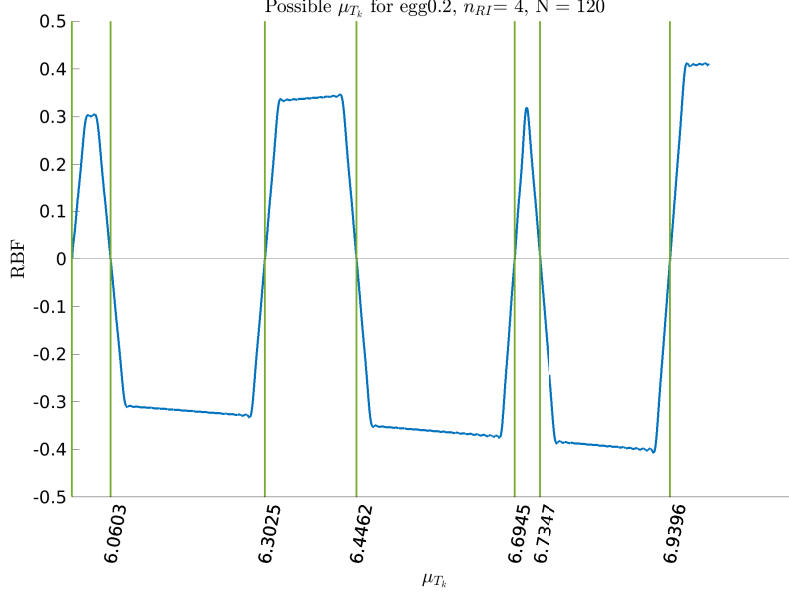
(a) Curve of minimum singular values of the operator $C(\mu)$ for $\mu \in [6, 12]$.



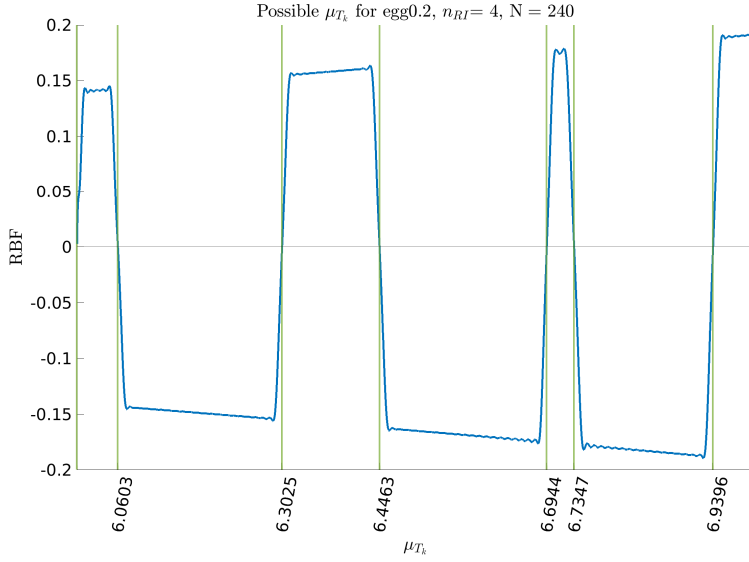
(b) Roots of the RBF interpolant of sign-flipped s_{min} curve of minimum singular values.

[Figure 4.2](#): Possible transmission eigenvalues in $[6, 12]$ of egg with curvature 0.2, $n_{RI} = 4$ using [Algorithm 4](#). Subfigure (a) shows the curve of minimum singular values s_{min} . Subfigure (b) shows the located zeros of RBF after sign flipping s_{min} .

The search for transmission eigenvalues for $\mu \in [6, 12]$ becomes increasingly difficult. We zoom in on the interval to $[6, 7]$ and perform a similar search. We set $N = 120$ and $N = 240$ to check whether there are any drastic differences in the root finding. In [Figure 4.3](#) we see that there are small differences in the 3rd and 4th zeros of the RBFs at the 4 decimal digit.



(a) Root finding step in algorithm 4 for $N = 120$.



(b) Root finding step in algorithm 4 for $N = 240$.

Figure 4.3: Refined search of μ_T in $[6, 7]$ for the egg with curvature 0.2.

We observe many roots in [Figure 4.2](#). So to increase the digits of accuracy, we perform a search only for $\mu \in [10, 11]$ with $N = 240$, which we show in [Figure 4.4](#). Again, on comparing with [Figure 4.2](#)

we see slight differences in digits of roots. So we suggest for better accuracy of the search approach, a combination of refining the search interval followed by RBF interpolation and root finding.

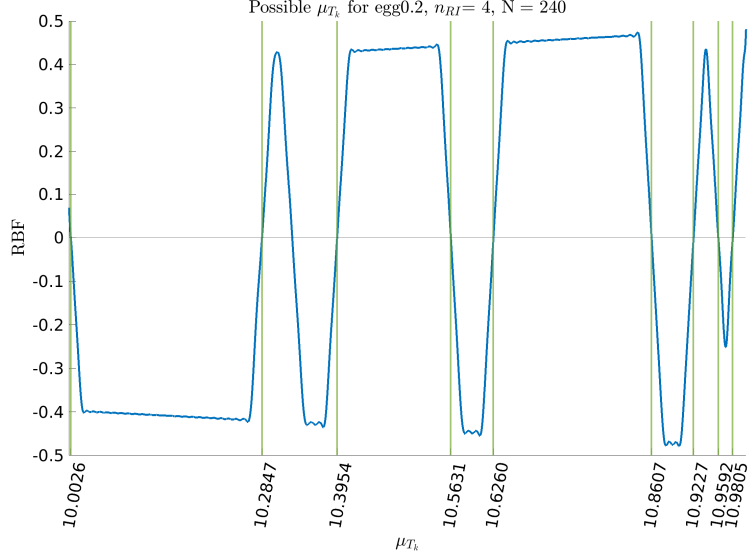


Figure 4.4: Refined search of μ_T in $[10, 11]$ for the egg with curvature 0.2.

We end this chapter by showing two eigenfunctions for the egg with curvature 0.2 with eigenvalues $\mu_T = 4.9026$ and 5.9997 in [Figure 4.5](#). The functions for $n_{RI} = 1$ are in green on the left and for $n_{RI} = 4$ are in red on the right.

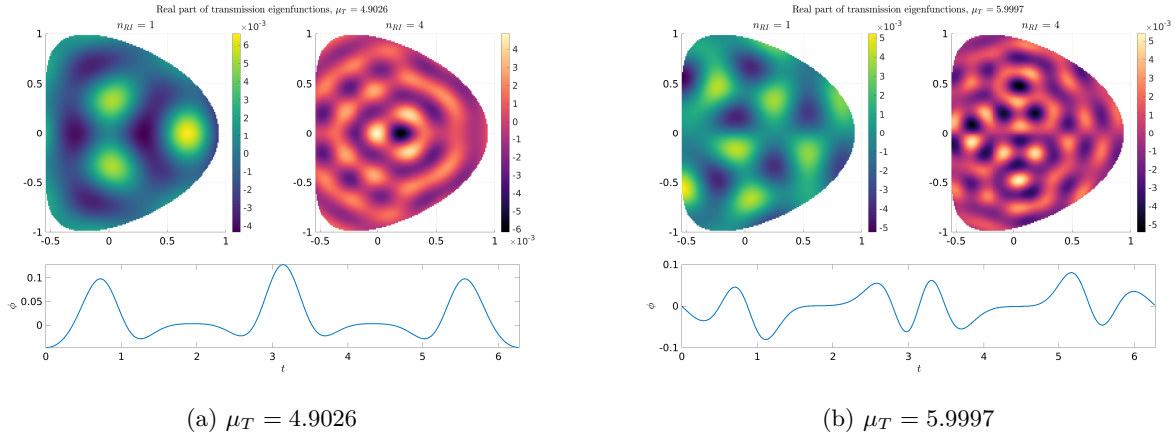


Figure 4.5: A couple of transmission eigenfunctions for the egg with curvature 0.2. Both subfigures show real part of eigenfunctions for $n_{RI} = 1$ (green, left) and $n_{RI} = 4$ (red, right). The bottom row shows the eigendensity ϕ .

Chapter 5

Conclusion and discussion

In this thesis we primarily studied the Steklov-Helmholtz eigenvalue problem on bounded Lipschitz domains. We reformulated the boundary-eigenvalue problem to a boundary integral equation and suggested a strategy for discretizing and numerically approximating the Steklov-Helmholtz eigenpairs. We built matrices corresponding to the discretized single layer potential and the adjoint of the double layer potential with the help of the Trapezoidal rule, and the quadrature and splitting technique given by Kussmaul and Martensen. We used these matrices to solve the Steklov-Helmholtz eigenvalue problem. We also adapted these matrices to locate Dirichlet, Neumann and Robin eigenvalues of the Laplacian. The idea was to search within a range of wave numbers μ for near singular kernels of the matrices (a similar strategy is used for the transmission eigenvalue problem with some caveats).

5.1 Summary

For the Steklov-Helmholtz eigenvalue problem (isospectral with the DtN map \mathcal{D}_μ), we use discretizations of the layer potentials to solve a generalized eigenvalue problem to find the eigenvalues and eigendensities. We observe spectral/exponential convergence with respect to number of points $2N$ that discretize the boundary M . The discretized single layer potential is also used to construct the eigenfunctions both inside the domain and on the boundary. We test the accuracy of the eigenfunctions of disks (concentric annuli) using the true solution on the disk (concentric annuli) with the help of subspace angles and observe convergence to them as well. Once we obtain part of the spectrum, we sort it and study it for the number of negative eigenvalues, homothety and asymptotic behaviour. To obtain the asymptotics of the Steklov-Helmholtz spectrum $\{\sigma_k\}$ as $k \rightarrow \infty$, we attempt to fit the first N eigenvalues with curves of type $Ak + B\sqrt{k} + C/\sqrt{k} + D$. We observe that in the long term, the eigenvalues approximately lie on a line with slope $\pi/|M|$. We speculate that the early part of the spectrum holds information about the shape (possibly through $|\Omega|, |M|$ or/and curvature κ) and wave number μ . We also document experiments with weights $L^\infty(M) \ni \rho > 0$ on M . We compute the ratios of the non-weighted and constant boundary weighted Steklov-Helmholtz

eigenvalues. The ratios are a constant value corresponding to the constant boundary weight. Finally, we try to optimize the k th scaled eigenvalue with the help of shape derivatives within a range of curve parameters. If there are Dirichlet-Laplace eigenvalues in our search region, the optimization gets attracted to them. In some cases, the optimization defaults to an end point in the search region. To avoid this behaviour, we numerically attempt to optimize with a constraint on the boundary by requiring $|M| = 1$.

We perform similar experiments with annular domains and conclude that appropriate modifications to the linear system can accommodate any number of holes in the domain. This comes at the expense of higher computational times, since M will have more components causing the size of the linear system to increase which will eventually lead to poor conditioning issues.

For the transmission eigenvalue problem with refractive index n_{RI} we use the matrices corresponding to the discretized layer potentials to form a difference operator $C(\mu)$ of DtN maps $\mathcal{D}_{\mu,n}$ s for $n = 1$ and $n = n_{RI}$. We propose a search strategy combining search interval refinement followed by sign flipping and RBF interpolation to locate wave numbers μ which could be transmission eigenvalues μ_T . The idea is to search within a range of wave numbers μ for which $C(\mu)$ has a near singular kernel. We test on domains with known transmission eigenvalues which are rather early on in the spectrum. The problem arises later on in the spectrum where it becomes increasingly difficult to tell apart which wave numbers μ are actually transmission eigenvalues. We are confident however that the root finding of the RBF interpolant works well whether or not the located zeros are transmission eigenvalues.

5.2 Future work

While we observe convergence of eigenvalues and eigenfunctions we have a few restrictive assumptions holding us back.

We would like to allow the boundary to be piecewise smooth with corners. This will let us find the Steklov-Helmholtz spectrum of polygons. To tackle the corners, we plan to begin with the use of a graded mesh with more points near the corners, as opposed to the equispaced grid points that we have used for smooth boundaries. This may also help recover more eigenvalues for smooth domains with large curvatures as noted in [Remark 3.4.1](#). Next, we would like to allow the wave number μ to correspond to a Dirichlet eigenvalue of the Laplacian and also be complex (this will make the problem non-self adjoint, see [Equation 1.16](#)). As we have seen while optimizing for the k th Steklov-Helmholtz eigenvalues, the Dirichlet-Laplace eigenvalues are minima which the search algorithm may get stuck in. We seem to have circumvented this issue for the first eigenvalue of the kite by fixing the perimeter, but much work remains to be done. Another inclusion we would like to make is for the sloshing problem (see [Equation 1.8](#)) where a part of the boundary has the homogeneous Dirichlet boundary condition and the rest has the Steklov boundary condition. The goal will be to allow for any type of boundary condition (Dirichlet, Neumann, Steklov) on different

parts of $M = \cup_{i=1}^n M_i$, where M is broken down into n parts. On the analytic side of things, we are working on estimates for errors of the scheme with respect to $N, \mu, |M|$ (see [Figure 3.7](#)) and possibly other domain properties, estimates for the asymptotics of eigenvalues and a Weinstock-type bound for the first eigenvalue. Simultaneously, we want to first extend this method for smooth surfaces in \mathbb{R}^3 .

For the transmission eigenvalue problem, we are working on improving the search algorithm. We are trying to regularize the search by the inclusion of the solution inside the domain as suggested in the modified method of particular solutions [\[BT05\]](#).

Ideally, in the future's future it would be great to extend this method for a class of boundary value problems for the Helmholtz equation, such as the Laplace-Wentzell eigenvalue problem where the boundary-eigenvalue condition is for given $\beta \in \mathbb{R}$: $-\beta\Delta u + \partial_\nu u = \sigma u$ (see equation 1.1 in [\[DWX18\]](#)). Such an extension would entail the construction of higher order potentials and appropriate choice of quadratures. It would be great to develop a class of methods for strongly elliptic eigenvalue problems up to second order which would first require the construction of an appropriate Green's function for the solutions. Perhaps we could begin with an inhomogeneous Helmholtz equation and the Poisson equation.

Clearly, there is so much more to do and we are cautiously optimistic as this thesis provides a good starting point with respect to the numerical schemes and highlights pitfalls of the methods used and assumptions made.

References

- [ABN14] Eldar Akhmetgaliyev, Oscar Bruno, and Nilima Nigam. “A boundary integral algorithm for the Laplace Dirichlet-Neumann mixed eigenvalue problem”. *Journal of Computational Physics* 298 (Nov. 2014). DOI: [10.1016/j.jcp.2015.05.016](https://doi.org/10.1016/j.jcp.2015.05.016).
- [AK19] Weaam Alhejaili and Chiu-Yen Kao. “Numerical studies of the Steklov eigenvalue problem via conformal mappings”. *Applied Mathematics and Computation* 347 (2019), pp. 785–802.
- [AKO17] Eldar Akhmetgaliyev, Chiu-Yen Kao, and Braxton Osting. “Computational methods for extremal Steklov problems”. *SIAM Journal on Control and Optimization* 55.2 (2017), pp. 1226–1240.
- [AM12] Wolfgang Arendt and Rafe Mazzeo. “Friedlander’s eigenvalue inequalities and the Dirichlet-to-Neumann semigroup”. *Communications on Pure and Applied Analysis* 11 (Nov. 2012). DOI: [10.3934/cpaa.2012.11.2201](https://doi.org/10.3934/cpaa.2012.11.2201).
- [Ant21] Pedro R.S. Antunes. “Numerical calculation of extremal Steklov eigenvalues in 3D and 4D”. *Computers and Mathematics with Applications* 104 (2021), pp. 50–58. ISSN: 0898-1221. DOI: <https://doi.org/10.1016/j.camwa.2021.11.008>. URL: <https://www.sciencedirect.com/science/article/pii/S0898122121004053>.
- [Auc05] Giles Auchmuty. “Steklov Eigenproblems and the Representation of Solutions of Elliptic Boundary Value Problems”. *Numerical Functional Analysis and Optimization* (2005). DOI: <https://doi.org/10.1081/NFA-120039655>.
- [BFK17] Dorin Bucur, Pedro Freitas, and James Kennedy. *4 The Robin problem*. Jan. 2017. ISBN: 9783110550887. DOI: [10.1515/9783110550887-004](https://doi.org/10.1515/9783110550887-004).
- [BG73] Ake Bjorck and Gene Golub. “Numerical Methods for Computing Angles Between Linear Subspaces”. *Mathematics of Computation* 27 (July 1973), p. 123. DOI: [10.2307/2005662](https://doi.org/10.2307/2005662).
- [BR00] K. Balakrishnan and P.A. Ramachandran. “The method of fundamental solutions for linear diffusion-reaction equations”. *Mathematical and Computer Modelling* 31.2 (2000), pp. 221–237. ISSN: 0895-7177. DOI: [https://doi.org/10.1016/S0895-7177\(99\)00233-2](https://doi.org/10.1016/S0895-7177(99)00233-2). URL: <https://www.sciencedirect.com/science/article/pii/S0895717799002332>.
- [BT05] Timo Betcke and Lloyd N. Trefethen. “Reviving the Method of Particular Solutions”. *SIAM Rev.* 47 (2005), pp. 469–491.
- [Cak+16] Fioralba Cakoni et al. “Stekloff Eigenvalues in Inverse Scattering”. *SIAM Journal on Applied Mathematics* 76 (Jan. 2016), pp. 1737–1763. DOI: [10.1137/16M1058704](https://doi.org/10.1137/16M1058704).

- [Car+01] J. Carr et al. “Reconstruction and Representation of 3D Objects With Radial Basis Functions”. *ACM SIGGRAPH* (Sept. 2001). DOI: [10.1145/383259.383266](https://doi.org/10.1145/383259.383266).
- [CDM22] Fabien Caubet, Marc Dambrine, and Rajesh Mahadevan. “Shape Sensitivity of Eigenvalue Functionals for Scalar Problems: Computing the Semi-derivative of a Minimum”. *Applied Mathematics & Optimization* 86 (Aug. 2022). DOI: [10.1007/s00245-022-09827-6](https://doi.org/10.1007/s00245-022-09827-6).
- [CG23] Adrien Chaigneau and Denis S. Grebenkov. “A numerical study of the Dirichlet-to-Neumann operator in planar domains” (Sept. 2023). arXiv: [2310.19571 \[cs.NA\]](https://arxiv.org/abs/2310.19571).
- [CH13] Anne Cossonnière and Houssem Haddar. “Surface integral formulation of the interior transmission problem”. *Journal of Integral Equations and Applications* 25.3 (2013), pp. 341–376. DOI: [10.1216/JIE-2013-25-3-341](https://doi.org/10.1216/JIE-2013-25-3-341). URL: <https://doi.org/10.1216/JIE-2013-25-3-341>.
- [Cha+12] Simon N. Chandler-Wilde et al. “Numerical-asymptotic boundary integral methods in high-frequency acoustic scattering”. *Acta Numerica* 21 (2012), pp. 89–305. DOI: [10.1017/S0962492912000037](https://doi.org/10.1017/S0962492912000037).
- [CK13] David Colton and Rainer Kress. *Inverse acoustic and electromagnetic scattering theory, third edition*. 2013. ISBN: 9781461449423 1461449421. URL: <http://link.springer.com/book/10.1007%2F978-1-4614-4942-3>.
- [CK17] Fioralba Cakoni and Rainer Kress. “A boundary integral equation method for the transmission eigenvalue problem”. *Applicable Analysis* 31.2 (2017), pp. 23–38. DOI: [10.1080/00036811.2016.1189537](https://doi.org/10.1080/00036811.2016.1189537).
- [CK83] David Colton and Rainer Kress. *Integral Equation Methods in Scattering Theory*. Society for Industrial and Applied Mathematics, 1983. URL: <https://epubs.siam.org/doi/abs/10.1137/1.9781611973167>.
- [DT23] Victor Dominguez and Catalin Turc. “Stability estimates of Nyström discretizations of Helmholtz decomposition boundary integral equation formulations for the solution of Navier scattering problems in two dimensions with Dirichlet boundary conditions” (Oct. 2023). arXiv: [2311.17032 \[cs.NA\]](https://arxiv.org/abs/2311.17032).
- [DWX18] Feng Du, Qiaoling Wang, and Changyu Xia. “Estimates for eigenvalues of the Wentzell-Laplace operator”. *Journal of Geometry and Physics* 129 (Mar. 2018). DOI: [10.1016/j.geomphys.2018.02.020](https://doi.org/10.1016/j.geomphys.2018.02.020).
- [DZ11] M. C. Delfour and J.-P. Zolésio. *Shapes and Geometries*. Second. Society for Industrial and Applied Mathematics, 2011. DOI: [10.1137/1.9780898719826](https://doi.org/10.1137/1.9780898719826). eprint: <https://epubs.siam.org/doi/pdf/10.1137/1.9780898719826>. URL: <https://epubs.siam.org/doi/abs/10.1137/1.9780898719826>.
- [Eva10] Lawrence C. Evans. *Partial differential equations*. American Mathematical Society, 2010. ISBN: 9780821849743 0821849743.
- [FS09] Ailana Fraser and Richard Schoen. “The first Steklov eigenvalue, conformal geometry, and minimal surfaces” (Dec. 2009).
- [FS12] Ailana Fraser and Richard Schoen. “Eigenvalue bounds and minimal surfaces in the ball”. *Inventiones mathematicae* 203 (Sept. 2012).

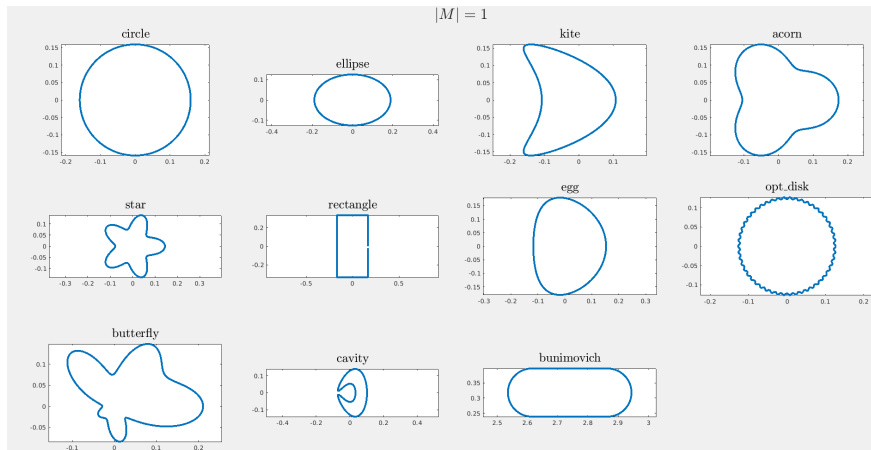
- [Gir+21] Alexandre Girouard et al. “The Dirichlet-to-Neumann map, the boundary Laplacian, and Hörmander’s rediscovered manuscript” (Feb. 2021).
- [GP10] Alexandre Girouard and Iosif Polterovich. “On the Hersch-Payne-Schiffer inequalities for Steklov eigenvalues”. *Functional Analysis and Its Applications* 44 (June 2010), pp. 106–117. DOI: [10.1007/s10688-010-0014-1](https://doi.org/10.1007/s10688-010-0014-1).
- [GP17] Alexandre Girouard and Iosif Polterovich. “Spectral geometry of the Steklov problem (survey article)”. *Journal of Spectral Theory* 7.2 (2017), pp. 321–359.
- [HL04] Jin Huang and Tao Lü. “The mechanical quadrature methods and the their extrapolation for solving BIE of Steklov eigenvalue problems”. *Journal of Computational Mathematics* 22.5 (2004), pp. 719–726. ISSN: 02549409, 19917139. URL: <http://www.jstor.org/stable/43693198> (visited on 09/09/2023).
- [HPS74] Joseph E. Hersch, Lawrence Edward Payne, and Menahem M. Schiffer. “Some inequalities for Stekloff eigenvalues”. *Archive for Rational Mechanics and Analysis* 57 (1974), pp. 99–114.
- [IN22] Kthim Imeri and Nilima Nigam. *A Steklov-spectral approach for solutions of Dirichlet and Robin boundary value problems*. 2022. arXiv: [2209.08405 \[math.NA\]](https://arxiv.org/abs/2209.08405).
- [Kre78] E. Kreyszig. *Introductory functional analysis with applications*. Wiley, 1978. ISBN: 9780471504597.
- [Kre99] Rainer Kress. *Linear integral equations*. Springer New York, NY, 1999. DOI: <https://doi.org/10.1007/978-1-4612-0559-3>.
- [Kus69] R. Kussmaul. “Ein numerisches Verfahren zur Lösung des Neumannschen Außenraumproblems für die Helmholtzsche Schwingungsgleichung”. *Computing* 4 (1969). URL: <https://doi.org/10.1007/BF02234773>.
- [Kuz+14] Nikolay G. Kuznetsov et al. “The legacy of Vladimir Andreevich Steklov”. *Notices of the American Mathematical Society* 61 (2014), pp. 9–23.
- [LMP22] Michael Levitin, Dan Mangoubi, and Iosif Polterovich. *Topics in spectral geometry*. Cambridge University Press, 2022.
- [Mar63] Erich Martensen. “Über eine Methode zum räumlichen Neumannschen Problem mit einer Anwendung für torusartige Berandungen”. *Acta Mathematica* 109.none (1963), pp. 75–135. DOI: [10.1007/BF02391810](https://doi.org/10.1007/BF02391810). URL: <https://doi.org/10.1007/BF02391810>.
- [McL00] William C. McLean. *Strongly Elliptic Systems and Boundary Integral Equations*. Cambridge University Press, 2000. ISBN: 9780521663755.
- [MK12] H. C. Mayer and R. Krechetnikov. “Walking with coffee: Why does it spill?” *Phys. Rev. E* 85 (4 Apr. 2012), p. 046117. DOI: [10.1103/PhysRevE.85.046117](https://doi.org/10.1103/PhysRevE.85.046117). URL: <https://link.aps.org/doi/10.1103/PhysRevE.85.046117>.
- [MM20] Jian Meng and Liquan Mei. “Discontinuous Galerkin methods of the non-selfadjoint Steklov eigenvalue problem in inverse scattering”. *Applied Mathematics and Computation* 381 (2020), p. 125307.
- [MS22] Y. Ma and J. Sun. “Integral Equation Method for a Non-Selfadjoint Steklov Eigenvalue Problem.” *Communications in Computational Physics* (2022). DOI: [10.4208/cicp.OA-2022-0016](https://doi.org/10.4208/cicp.OA-2022-0016).

- [Neč11] Jindřich Nečas. *Direct Methods in the Theory of Elliptic Equations*. Springer Berlin, Heidelberg, 2011. ISBN: 9783642104558.
- [OKO21] Edouard Oudet, C.-Y Kao, and Braxton Osting. “Computation of free boundary minimal surfaces via extremal Steklov eigenvalue problems”. *ESAIM: Control, Optimisation and Calculus of Variations* 27 (Mar. 2021). DOI: [10.1051/cocv/2021033](https://doi.org/10.1051/cocv/2021033).
- [SEVP] SEVP. *AimPL: Steklov eigenproblems*. American institute of Mathematics. URL: <http://aimpl.org/stekloveigen>.
- [SXY23] Qi Sun, Xuejun Xu, and Haotian Yi. “Dirichlet-Neumann learning algorithm for solving elliptic interface problems” (Jan. 2023). DOI: [10.48550/arXiv.2301.07361](https://doi.org/10.48550/arXiv.2301.07361).
- [TGH98] Wei-jun Tang, Zhi Guan, and Hou-de Han. “Boundary element approximation of Steklov eigenvalue problem for Helmholtz equation”. *Journal of Computational Mathematics* (1998), pp. 165–178.
- [Tur21] Onder Turk. “A DRBEM approximation of the Steklov eigenvalue problem”. *Engineering Analysis with Boundary Elements* 122 (Jan. 2021), pp. 232–241. DOI: [10.1016/j.enganabound.2020.11.003](https://doi.org/10.1016/j.enganabound.2020.11.003).
- [Wan+18] Yu Wang et al. “Steklov Spectral Geometry for Extrinsic Shape Analysis”. *ACM Transactions on Graphics* 38 (2018). DOI: <https://doi.org/10.1145/3152156>.
- [Wei54] Robert Weinstock. “Inequalities for a Classical Eigenvalue Problem”. *Journal of Rational Mechanics and Analysis* 3 (1954), pp. 745–753. ISSN: 19435282, 19435290. URL: <http://www.jstor.org/stable/24900312> (visited on 08/16/2023).

Appendix A

Curve library

- Circle: $(x_1, x_2) = (R \cos t, R \sin t)$, where R is the radius.
- Ellipse: $(x_1, x_2) = (a \cos t, b \sin t)$. a, b are the semi major/minor axes lengths. We set $a = 3$, $b = 2$.
- Deformed ellipse: $(x_1, x_2) = (\cos t + \kappa_p \cos 2t - \kappa_p, 1.5 \sin t)$, where κ_p is the curvature. We refer to this curve as a Kite for $\kappa_p = 0.65$.
- Acorn: $(x_1, x_2) = \sqrt{4.25 + 2 \cos 3t} (\cos t, \sin t)$
- Star: $(x_1, x_2) = (1 + 0.3 \cos 5t) (\cos t, \sin t)$
- Butterfly: $(\exp(\cos t)(\cos 2t)^2 + \exp(\sin t)(\sin 2t)^2) (\cos t, \sin t)$
- Egg: $(x_1, x_2) = (0.75 \cos t + \epsilon \cos 2t, \sin t)$, where ϵ is the curvature.
- Cavity: $(x_1, x_2) = \left(\frac{1}{4}(\cos t + 2 \cos 2t), \frac{1}{2}(\sin t + \sin 2t + 0.5 \sin 3t) + \frac{1}{48}(4 \sin t - 7 \sin 2t + 6 \sin 3t - 2 \sin 4t) \right)$



The domains worked with (except rectangle).

Appendix B

README for the code

In this section, we describe in detail the usage of the codes that we wrote in MATLAB. The codes in their most recent version are at [my GitHub](#).

B.1 Curves

This function creates curve points and their derivatives given the parametrization, $z(t) = (z_1(t), z_2(t))$. In the code we denote by \mathbf{x} the set of points $\{(z_1(t_j), z_2(t_j))\}_{j=1}^{2N+1}$, where \mathbf{t} is a partition of $[0, 2\pi]$ of $2N + 1$ points generated as $t = 0 : \frac{2\pi}{2N} : 2\pi$.

Inputs

- `name` is a string of the curve name matching with the name as in the code, case insensitive.
- `t` is the set of $2N + 1$ partition points.
- `len1` is either 1 or 0, indicating whether to normalize the perimeter or not.
- `varargin` is for extra variable the curve parametrization may require, for example the radius in case of a circle.

Outputs

- `x, dx` and `d2x` are the points on the curve and the first 2 derivatives of the parametrization at those points respectively.
- `nx` is the outward unit normal at the points.
- `len` is the perimeter $|M|$ of the curve.

```

1 function [x,dx,d2x,nx,len] = curve(name,t,len1,varargin)
2 switch lower(name)
3 case 'circle'
4     r = varargin{1};
5     x = r*[cos(t);sin(t)];
6     dx = r*[-sin(t);cos(t)];
7     d2x = -x;
8     len = 2*pi*r;
9 case 'ellipse'
10    a = varargin{1}; b = varargin{2};
11    x = [a*cos(t);b*sin(t)];
12    dx = [-a*sin(t);b*cos(t)];
13    d2x = -x;
14    len = integral(@(t)sqrt(a^2*sin(t).^2+b^2*cos(t).^2),0,2*pi);
15 case 'kite'
16    x = [cos(t)+0.65*cos(2*t)-0.65;1.5*sin(t)];
17    dx = [-sin(t)-1.3*sin(2*t);1.5*cos(t)];
18    d2x = [-cos(t)-2.6*cos(2*t);-1.5*sin(t)];
19    len = integral(@(t) sqrt((sin(t)+1.3*sin(2*t)).^2+(1.5*cos(t)).^2)
20                  ,0,2*pi);
21 end
22 if len1 ~=0
23     x = x/len; dx = dx/len; d2x = d2x/len; len = 1;
24 end
25 nx = [dx(2,:);-dx(1,:)];
26 nx = nx./sqrt(dx(1,:).^2+dx(2,:).^2);
27 end

```

To add a curve, we add an extra `case` with the curve name and the details. The outputs of the function can be used for various things. Below we show the computation of the domain area and mean curvature κ of the curve.

```

1 dom_area = polyarea(x(1,:)',x(2,:)'); % polyarea is an inbuilt function in
                                             MATLAB
2 kappa = (dx(1,1:end-1).*d2x(2,1:end-1)-d2x(1,1:end-1).*dx(2,1:end-1))./(dx
    (1,1:end-1).^2+dx(2,1:end-1).^2).^1.5;
3 kappa = sum(kappa)*pi/N; kappa = kappa/(2*pi);

```

We make the following `meshgrids` from the data and create sin and cos vectors used for the creation of trigonometric polynomials.

```

1 [Tau,T] = meshgrid(t);
2 [Xtau,Xt] = meshgrid(x(1,:));
3 [Ytau,Yt] = meshgrid(x(2,:));
4 [dXtau,dXt] = meshgrid(dx(1,:));
5 [dYtau,dYt] = meshgrid(dx(2,:));

```

```

6 [d2Xtau,d2Xt] = meshgrid(d2x(1,:));
7 [d2Ytau,d2Yt] = meshgrid(d2x(2,:));
8 t_scaled = (0:2*N).*T; % the first column is 0*t, second is 1*t, ..., l*t is
    the lth column and so on.
9 cos_vecs = cos(t_scaled); % l is fixed in columns, t_j is fixed in rows.
10 sin_vecs = sin(t_scaled);

```

B.2 Trigonometric polynomials

When numerically integrating using the quadratures, we first find the trigonometric polynomials of the integrands.

Inputs

- f is a meshgrid of the function evaluations
- N is half the number of distinct partition points of $[0, 2\pi]$ where by periodicity 0 and 2π are the same.
- `cos_vecs`, `sin_vecs` are as described above.

Outputs

- tp is the meshgrid of the trigonometric polynomial of f .

```

1 function tp = ftp(f,N,cos_vecs,sin_vecs)
2     al = f(:,1:(end-1))*cos_vecs(1:end-1,1:N+1)/N;
3     al(:,[1,end]) = al(:,[1,end])/2;
4     bl = f(:,1:(end-1))*sin_vecs(1:end-1,2:N)/N;
5     tp = al*cos_vecs(:,1:N+1)' + bl*sin_vecs(:,2:N)';
6 end

```

B.3 Layer potentials

Next, we create the layer potential matrices.

`inputs:` μ is the wavenumber and the rest are the meshgrids as defined above.

`outputs:` A is the matrix for K' (adjoint of the double layer) and B is the matrix for S (single layer).

```

1 function [A,B] = layer_pots(mu,Tau,T,Xtau,Xt,Ytau,Yt,dXtau,dXt,dYtau,dYt,d2Xt
    ,d2Yt)
2

```

```

3 N = (size(Tau,1)-1)/2;
4
5 %% R, X for all pairs t, tau
6 X = dYt.* (Xtau-Xt)-dXt.* (Ytau-Yt);
7 R = sqrt((Xt-Xtau).^2+(Yt-Ytau).^2);
8 XR_ratio = X./R;
9 % -----
10
11 %% L, M -----
12 tic
13 dp1norm = sqrt(dXt.^2+dYt.^2);
14 dp2norm = sqrt(dXtau.^2+dYtau.^2);
15 dpnorm_ratio = dp2norm./dp1norm;
16 logsin_term = log(4*sin((T-Tau)/2).^2);
17 cL = (1i*mu/2)*dpnorm_ratio;
18 cL1 = -mu/(2*pi)*dpnorm_ratio;
19 L = cL.*XR_ratio.*besselh(1,mu*R); % note that besselh(1,0) blows up so when
   R = 0 it's useless.
20
21 L1 = cL1.*XR_ratio.*besselj(1,mu*R);
22 L2 = L-L1.*logsin_term;
23 L(isnan(L)) = diag((dYt.*d2Xt-dXt.*d2Yt)./(2*pi*dp1norm.^2));
24 L2(isnan(L2)) = diag(L);
25 L1(isnan(L1)) = 0;
26
27 M = (1i/2)*dp2norm.*besselh(0,mu*R);
28 M1 = -1/(2*pi)*dp2norm.*besselj(0,mu*R);
29 M2 = M-M1.*logsin_term;
30 mc = 1i/2-double(eulergamma)/pi;
31
32 M2(isnan(M2)) = diag(dp1norm.* (mc-log(mu/2*dp1norm)/pi));
33
34 %-----
35
36 %% Trig. poly. -----
37 % f^tp(t,tau) =
38 % (a_0/2,a_1,...,a_{N-1},a_N/2).(1,cos(tau),...,cos([N-1]tau),cos([N]tau))+
39 % (b_1,...,b_{N-1}).(sin(tau),...,sin([N-1]tau)) =
40 % a_vec.cos_ON_vec + b_vec.sin_ON_vec
41 t_scaled = (0:2*N).*T; % the first column is 0*t, second is 1*t, so on.
42 cos_vecs = cos(t_scaled); % l is fixed in columns, t_j is fixed in rows.
43 sin_vecs = sin(t_scaled);
44
45 %L1 tp
46 L1_tp = ftp(L1,N,cos_vecs,sin_vecs);

```

```

47
48 % L2_tp
49 L2_tp = ftp(L2,N,cos_vecs,sin_vecs);
50
51 %M1_tp
52 M1_tp = ftp(M1,N,cos_vecs,sin_vecs);
53
54 % M2_tp
55 M2_tp = ftp(M2,N,cos_vecs,sin_vecs);
56 toc
57 % -----
58
59 %% RN weights (quadrature from ColtonKress), same for any integrand (L1,M1
   for us) -----
60 tic
61 diff_t_tau = T-Tau;
62
63 RN_mat = cos(diff_t_tau);
64 for k1 = 2:(N-1)
65     RN_mat = RN_mat+cos(k1*diff_t_tau)/k1;
66 end
67 RN_mat = -2*pi*RN_mat/N - pi*cos(N*(diff_t_tau))/N^2;
68 % end
69 toc
70
71 %-----
72
73 %% Matrices -----
74 A = RN_mat.*L1_tp+pi/N*L2_tp; % The second term is trapezoidal rule
75 % (A + I) is the effect of K'
76 A(:,end) = []; A(end,:) = [];
77
78 B = RN_mat.*M1_tp+pi/N*M2_tp; % B is the effect of the S
79 B(:,end) = []; B(end,:) = [];
80
81 end

```

B.4 Steklov eigenvalues

Now we use the matrices to solve a generalized eigenvalue problem using `eig` in MATLAB.

```

1 I = eye(2*N);
2 [eden1,evs1] = eig(I+A,B);
3 evs1 = diag(evs1);

```

```

4
5 if sum(imag(evs1)) < 1e-9
6   evs = real(evs1);
7   [evs, ind] = sort(evs);
8   eden = eden1(:,ind); % eigen densities
9   [~,blah,ev_reps] = uniquetol(real(evs));
10  ev_reps = blah(accumarray(ev_reps,1).'==1);% indices of non repeated evals
11 else
12 disp("Imaginary part of eigenvalues too high. Either mu is very close to a
      Dirichlet eigenvalue or N is too small.")
13 end
14 evecs = B*eden/2;
15 normder_evecs = (A+I)*eden/2;

```

We now discuss the use of the eigen density ψ (eden) to compute the solution inside the domain and begin by creating a grid of points inside the curve.

```

1 m = 150; % choose according to N and increase if needed.
2 xi = linspace(min(x(1,:)),max(x(1,:)),m);
3 yi = linspace(min(x(2,:)),max(x(2,:)),m);
4 [X,Y] = meshgrid(xi,yi) ;
5 idx = inpolygon(X(:,Y(:,x(1,:),x(2,:)) ;
6 points_inside = transpose([X(idx),Y(idx)]);
7 [Xtauin,Xin] = meshgrid(x(1,1:end-1),points_inside(1,:)); % mesh x coord of
      in points and bdry points
8 [Ytauin,Yin] = meshgrid(x(2,1:end-1),points_inside(2,:)); % mesh y coord of
      in points and bdry points

```

B.5 Construction of solutions inside Ω

Next we fix an eigenvalue number and compute the solution inside using the trapezoidal rule.

```

1 fix = 2;
2 bessord = evsac_mat(evs_ac(fix)==evsac_mat(:,1),2); % for circle
3 eden_fix = eden(:,fix);
4
5 Xindiff = Xtauin-Xin; Yindiff = Ytauin-Yin;
6 Rin = sqrt(Xindiff.^2+Yindiff.^2);
7 HankRin = besselh(0,mu*Rin); % rows correspond to fixed point inside
8 Recon_integrand = HankRin.*transpose(eden_fix).*dp2norm(fix,(1:end-1)); %
      make this a tp and then sum and scale
9 recint_cos1 = Recon_integrand*cos_vecs(1:end-1,1:N+1)/N;
10 recint_cos1(:,[1,end]) = recint_cos1(:,[1,end])/2;
11 recint_sin1 = Recon_integrand*sin_vecs(1:end-1,2:N)/N;

```

```

12 recint_cos = recint_cos1*cos_vecs(:,1:N+1)';
13 recint_sin = recint_sin1*sin_vecs(:,2:N)';
14 recint = recint_cos+ recint_sin; recint = recint(:,1:end-1);
15
16 % solution at points inside
17 solution_fixed_point = 1i*pi/(4*N)*sum(recint,2);
18
19 % interpolate solution
20 xlin = linspace(min(points_inside(1,:)),max(points_inside(1,:)),round(1*m));
21 ylin = linspace(min(points_inside(2,:)),max(points_inside(2,:)),round(1*m));
22
23 [Xin2,Yin2] = meshgrid(xlin,ylin);
24
25 Uin = griddata(points_inside(1,:),points_inside(2,:),solution_fixed_point,
      Xin2,Yin2,'cubic');
26 RealUin = real(Uin); ImagUin = imag(Uin);
27
28 % remove solution computed outside domain
29 bdrypts =
30 inpolygon(Xin2,Yin2,x(1,:),x(2,:));
31 Xin2(~bdrypts) = NaN; Yin2(~bdrypts) = NaN;
32
33 % sample plot
34 surf(Xin2,Yin2,RealUin);
35 shading interp; view(0,90); colormap(magma); colorbar
36 title('$\text{Real}(u^N_n)$', 'Interpreter', 'latex')
37 xlabel('$x_1$', 'Interpreter', 'latex'); ylabel('$x_2$', 'Interpreter', 'latex');
      zlabel('Real$(u)$', 'Interpreter', 'latex');

```

B.6 RBFs

We use RBFs to find the tangential gradient and to interpolate the sign-flipped minimum singular values for the Dirichlet/Neumann/Robin Laplace and Transmission eigenvalue problems.

```

1 fix = 1; % eigenvalue number
2 norm_M = sum(abs(evecs(:,fix)).^2)*pi/N; % normalization for eigenfunction
3 norm_evec = evecs(:,fix)/sqrt(abs(norm_M));
4 eden_fix = eden(:,fix)/sqrt(abs(norm_M));
5
6 % RBF setup
7 rbf_points = x(:,1:end-1);
8 rbf_f = norm_evec;
9 [Xtau_rbf,Xt_rbf] = meshgrid(rbf_points(1,:));
10 [Ytau_rbf,Yt_rbf] = meshgrid(rbf_points(2,:));

```

```

11 R_rbf = sqrt((Xt_rbf-Xtau_rbf).^2+(Yt_rbf-Ytau_rbf).^2);
12
13 % RBF list and parameters
14 rbf_c = 0.05;
15 %rbf = @(t) t; drbf = @(t) 1;
16 %rbf = @(t) t.^3; drbf = @(t) 3*t; % dividing with t for the x/r(t) part.
17 %rbf = @(t) t.^2.*log(t+rbf_c); drbf = @(t) 2*log(t+rbf_c)+t./t+rbf_c;
18 rbf = @(t) 1./sqrt(t.^2+rbf_c.^2); drbf = @(t) -1./t.^2+rbf_c.^2).^1.5;
19 %rbf = @(t) 1./t.^2+rbf_c.^2; drbf = @(t) -1./t.^2+rbf_c.^2).^2;
20
21 % rbf = @(x,y) 1./(x.^2+rbf_c.^2).*(1./(y.^2+rbf_c.^2));
22 % drbfx = @(x,y) (-2*x)./(x.^2+rbf_c.^2).^2*1./(y.^2+rbf_c.^2);
23 % drbfy = @(x,y) (-2*y)./(y.^2+rbf_c.^2).^2*1./(x.^2+rbf_c.^2);
24
25 %rbf = @(t) exp(-rbf_c*t.^2); drbf = @(t) -2*rbf_c*exp(-rbf_c*t.^2);
26
27 % Setup linear system
28 bf = 0;
29 if bf == 1
30     A_rbf = rbf((Xt_rbf-Xtau_rbf),(Yt_rbf-Ytau_rbf));
31 else
32     A_rbf = rbf(R_rbf);
33 end
34 A_rbf = (A_rbf+A_rbf')/2;
35
36 rbf_mat = A_rbf;
37 rbf_rhs = rbf_f;
38
39 % solve linear system for coefficients
40 rbf_coeffs = rbf_mat\rbf_rhs;
41
42 % compute function, gradient an tangential gradient in terms of RBF
43 rbf_grad = zeros(size(x,2)-1,2);
44 rbf_fun = zeros(size(x,2)-1,1);
45 rbf_tgrad = zeros(size(x,2)-1,2);
46 for i = 1:(size(x,2)-1)
47     for j = 1:size(rbf_points,2)
48         if bf == 1
49             rbf_fun(i) = rbf_fun(i)+rbf_coeffs(j)*rbf(x(1,i)-rbf_points(1,j),x
50                 (2,i)-rbf_points(2,j));
51             rbf_grad(i,:) = rbf_grad(i,:) + rbf_coeffs(j)*[drbfx(x(1,i)-
52                 rbf_points(1,j),x(2,i)-rbf_points(2,j)),drbfy(x(1,i)-rbf_points
53                 (1,j),x(2,i)-rbf_points(2,j))];
54         else
55             distr = norm(x(:,i)-rbf_points(:,j));

```

```
53     rbf_fun(i) = rbf_fun(i)+rbf_coeffs(j)*rbf(distr);
54     rbf_grad(i,:) = rbf_grad(i,:) + rbf_coeffs(j)*drbf(distr)*(x(:,i)
55                           '-rbf_points(:,j)');
56 end
56 end
57 rbf_tgrad(i,:) = rbf_grad(i,:)-sum(rbf_grad(i,:).*nx(:,i)')*nx(:,i)';
58 end
```